Elsevier Editorial System(tm) for Tectonophysics

Manuscript Draft

Manuscript Number: TECTO13230R1

Title: Crust-mantle coupling during continental convergence and break-up: Constraints from peridotite xenoliths from the Borborema Province, northeast Brazil

Article Type: Research Paper

Keywords: Subcontinental mantle lithosphere
Crust-mantle coupling
Melt-rock interaction
Annealing
Olivine crystal preferred orientation
Seismic anisotropy

Corresponding Author: Dr. Andrea Tommasi, Dr

Corresponding Author's Institution: CNRS & Univ Montpellier

First Author: Shiran Liu

Order of Authors: Shiran Liu; Andrea Tommasi, Dr; Alain Vauchez; Maurizio Mazzucchelli

Abstract: We studied a suite of mantle xenoliths carried by Cenozoic volcanism in the Borborema Province, NE Brazil. These xenoliths sample a subcontinental lithospheric mantle affected by multiple continental convergence and rifting events since the Archean. Equilibrium temperatures indicate a rather hot geotherm, implying a ca. 80 km thick lithosphere. Most xenoliths have coarse-granular and coarse-porphyroclastic microstructures, recording variable degrees of annealing following deformation. The high annealing degree and equilibrated pyroxene shapes in coarse-granular peridotites equilibrated at ~900°C indicate that the last deformation event that affected these peridotites is several hundreds of Ma old. Coarse-porphyroclastic peridotites equilibrated at 950-1100°C probably record younger (Cretaceous?) deformation in the deep lithospheric mantle. In addition, a few xenoliths show fine-porphyroclastic microstructures and equilibrium temperatures ≥1200°C, which imply a recent deformation, probably related to the dykes that fed the Cenozoic volcanism. Chemical and microstructural evidence for reactive percolation of melts is widespread. Variation in textural and chemical equilibrium among samples implies multiple melt percolation events well spaced in time (from Neoproterozoic or older to Cenozoic). Crystal preferred orientations of olivine and pyroxenes point to deformation controlled by dislocation creep with dominant activation of the [100](010) and [001]{0kl} slip systems in olivine and pyroxenes for all microstructures. Comparison of xenoliths' seismic properties to SKS splitting data in the nearby RCBR station together with the equilibrated microstructures in the low-temperature xenoliths point to coupled crust-mantle deformation in the Neoproterozoic (Brasiliano) continental-scale shear zones, which is still preserved in the shallow lithospheric mantle. This implies limited reworking of the lithospheric mantle in response to

extension during the opening of the Equatorial Atlantic in the Cretaceous, which in the present sampling is restricted to the base of the lithosphere.

Research Data Related to this Submission

There are no linked research data sets for this submission. The following reason is given:
Data will be made available on request

*Cover Letter

Géosciences Montpellier
UMR 5243 CNRS/UM/UA

Dear Editor,

Pleased find enclosed the revised version of the ms. "Crust-mantle coupling during continental convergence and break-up: Constraints from peridotite xenoliths from the Borborema Province, northeast Brazil" (previous title "The lithospheric mantle in a continental domain submitted to multiple tectonic events: Peridotite xenoliths from the Borborema Province, northeast Brazil").

We have carefully revised the ms. implementing all suggestions from the two reviewers. In short, we fully reorganized the data presentation and the discussion as suggested by reviewer 1 and revised all figures to enhance their readability. We also reduced the number of figures and transferred the table with the chemical analyses data to the Supplementary on line material.

The result is a slightly shorter article (by 1 page and 1 figure), which we hope is easier to read and better presents the data and conveys our conclusions.

Sincerely yours,

Shiran Liu and Andréa Tommasi on the behalf of all co-authors

Géosciences Montpellier
CC60 - Université de Montpellier, Place E. Bataillon, 34095 Montpellier cedex 05, France
Tél. +33 (0)4 67 14 37 28 - dirgm@gm.univ-montp2.fr - http://www.gm.univ-montp2.fr

Crust-mantle coupling during continental convergence and break-up: Constraints from peridotite xenoliths from the Borborema Province, northeast Brazil

Shiran Liu[1,2], Andréa Tommasi[1], Alain Vauchez[1], Maurizio Mazzucchelli[3]

[1]*Géosciences Montpellier, CNRS & Université de Montpellier, Montpellier, France.*
[2]*Key Laboratory of Orogenic Belts and Crustal Evolution, School of Earth and Space Sciences, Peking University, Beijing, China.*
[3]*Dipartimento di Scienze Chimiche e Geologiche, Università di Modena e Reggio Emilia, Modena, Italy.*

Abstract

We studied a suite of mantle xenoliths carried by Cenozoic volcanism in the Borborema Province, NE Brazil. These xenoliths sample a subcontinental lithospheric mantle affected by multiple continental convergence and rifting events since the Archean. Equilibrium temperatures indicate a rather hot geotherm, implying a ca. 80 km thick lithosphere. Most xenoliths have coarse-granular and coarse-porphyroclastic microstructures, recording variable degrees of annealing following deformation. The high annealing degree and equilibrated pyroxene shapes in coarse-granular peridotites equilibrated at ~900°C indicate that the last deformation event that affected these peridotites is several hundreds of Ma old. Coarse-porphyroclastic peridotites equilibrated at 950-1100°C probably record younger (Cretaceous?) deformation in the deep lithospheric mantle. In addition, a few xenoliths show fine-porphyroclastic microstructures and equilibrium temperatures ≥1200°C, which imply a recent deformation, probably related to the dykes that fed the Cenozoic volcanism. Chemical and microstructural evidence for reactive percolation of melts is widespread. Variation in textural and chemical equilibrium among samples implies multiple melt percolation events well spaced in time (from Neoproterozoic or older to Cenozoic). Crystal preferred orientations of olivine and pyroxenes point to deformation controlled by dislocation creep with dominant activation of the [100](010) and [001]{0kl} slip systems in olivine and pyroxenes for all microstructures. Comparison of xenoliths' seismic properties to SKS splitting data in the nearby RCBR station together with the equilibrated microstructures in the low-temperature xenoliths point to coupled crust-mantle deformation in the Neoproterozoic (Brasiliano) continental-scale shear zones, which is still preserved in the shallow lithospheric mantle. This implies limited reworking of the lithospheric mantle in response to extension during the opening of the Equatorial Atlantic in the Cretaceous, which in the present sampling is restricted to the base of the lithosphere.

***Revision Notes**
Click here to download Revision Notes: Revision_Notes.docx

Dear editor,

Please find enclosed a point-by-point answers (in black) to the reviewers comments (in blue).

We have implemented all requested changes, with the exception of your suggestion of production of "a nice take-home message figure summarizing the results and allowing at once to capture the history (eg inflitrations, melting or deformation events), relative chronology and possible past location of the samples with respect to depth and major tectonic events (with of course appropriate question marks where needed)". We tried, but there is too much uncertainty in the timing of the different tectono-magmatic events in the mantle and in their correlation with the dated crustal record. We can clearly convey this uncertainty in the text. However, we feel that we cannot do it in a figure even if question marks were added (we would need to add question marks to all parts of the figure). It would also be difficult to indicate the variation in "robustness" of the various interpretations. A last problem in preparing such a figure is that, although we may infer the kinematics of the deformation frozen in the shallow lithospheric mantle based on the consistency between crustal deformation and SKS splitting data, we have no constraints on the kinematics of the possible Cretaceous deformation in the deep lithospheric mantle. The SKS splitting data is better explained if flow directions in the mantle are parallel to NNE over the entire lithospheric mantle and the asthenosphere. Yet such a direction is at high angle to all Cretaceous extensional structures… Therefore, we reworked the text in order to clarify our conclusions on the relative timing of the tectono-magmatic events in the mantle lithosphere and on the crust-mantle coupling during these events, but prefer not to produce a summary interpretative figure, which may lead the readers to imagine that these conclusions are more robust than they are really.

We fully reorganized the data presentation and the discussion as suggested by reviewer 1 and revised all figures to enhance their readability. The revision resulted in a slightly shorter article (by 1 page and 1 figure), which we hope is easier to read and better conveys our conclusions. All major changes are highlighted in the annotated version of the ms.

Comments by Sandra Piazolo.

The manuscript "The lithospheric mantle in a continental domain submitted to multiple tectonic events: Peridotite xenoliths from the Borborema Province, northeast Brazil" by Liu et al. represents an extensive dataset on a suite of xenoliths from the subcontinental lithosphere of NE Brazil. It is without doubt a lovely dataset well worth publishing, the authors collected both orientation and chemical data and relate the data to existing geophysical datasets. The data is in general very nicely presented and thoroughly interrogated (mostly in form of bulk data), however at present the manuscript feels a bit like an amalgamation of data with not a clear hypothesis or research question to test in mind. This also means that there are lots of different strands of information followed in the manuscript and it leaves the reader a bit lost. So currently - after a fast read (what most reader do) currently the reader learns that xenoliths are varied and the lithospheric mantle is heterogeneous with different annealing and metasomatic modifications. But I think there is more you can get out of the data set. I believe that this manuscript could highly benefit from streamlining towards a bigger question: The authors provide the question in the first paragraph of their introduction (as well as the last part of their discussion) - is the deformation of crust and mantle coupled or not? Are there times when there is decoupling prevalent and other times were there is coupling seen. This is then a

large-scale big picture question of interest to the general geological community. And very few datasets allow such an evaluation.

This would mean that the authors would need to link more explicitly some of the microstructures to the geotectonic setting known from the crustal parts of the lithosphere. Maybe in some xenoliths you have different domains so you can develop a time sequence - it looks to me that you could do that? At present the authors do it for the last event - linking the high stress recrystallization to melt intrusion (nice), however can one make some links for the other 900 C and >1000 C structures?
Overall the paper will benefit from streamlining with the big paper in mind, please have a think if you need all figures. Maybe you can put some in supplementary (see suggestions). After the revisions the paper will be ideally reduced by 10-15%. Here some shuffling of section will help.
We sincerely thank S. Piazolo for her throughout and very constructive review. We extensively reworked the presentation of the data and the discussion as suggested, so that we better streamline the presentation of the evidence and the discussion of the relative timing of the various tectono-magmatic events and their relation to the dated crustal structures. This allows to discuss the question of crust-mantle coupling during major tectonic events. In the present case, we propose that there is strong evidence for pervasive deformation of the entire lithosphere, with strong crust-mantle coupling, during the formation of the Borborema shear zone system in an intraplate setting during the late stages of the continental convergence that lead to the formation of the Gondwana supercontinent. In contrast, extension leading to continental break-up and formation of the Equatorial Atlantic Ocean in the Cretaceous seems to have resulted limited reworking of the lithospheric mantle, which in the present xenolith sampling is only recorded in a few xenoliths with equilibration temperatures >1000°C. Moreover, SKS splitting data does not support flow directions in the lithospheric mantle consistent with the extensional structures. Altogether, these observations point to decoupling between crustal and mantle deformation or to very localized deformation in response to extension in the lithospheric mantle.

Comments and suggestions:

1) Title: Have another look at it, can you provide a statement regarding coupling? Or deformation / metasomatism sequences you identify?
We revised the title as suggested. However, if the reviewers consider the new title too appealing, we are happy with the original one (The lithospheric mantle in a continental domain affected by multiple tectonic events: Peridotite xenoliths from the Borborema Province, northeast Brazil), which described precisely the observations presented in the article.

2) Abstract: needs some rephrasing to put up the question to be answered more clearly. Rework after defining more precisely which structures are probably related to which tectonic event. The current last two sentences are interesting but please add what that means - i.e. fabrics can be frozen in in the mantle part of the lithosphere over billions of years (if you argue for frozen in strike slip fabrics (actually not much about this in the current main body of text) - this is interesting because that would mean that such features would probably influence future tectonic events in orientation and deformation rate. In addition if that is true then there would be a clear direct coupling from continental crust to the continental lithosphere during strike slip - an important feature to know if one wants to understand large scale tectonics. Also what does it mean that there is a significant mismatch of calculated and measured seismic delay times? Does that mean that the xenolith only sample an old component and not

current deformation state? (again not really discussed in the main text - please rectify) (Please note, these questions need to be addressed in the discussion and depending on outcome the abstract needs to be modified).
We have reworked the abstract to better convey the conclusions of the article concerning the relative timing of the deformation and metasomatism in the mantle and crust-mantle coupling. We also rephrased the part presenting the comparison with seismic anisotropy data leaving to the discussion and conclusion of the article the discussion of the fact that the xenoliths only sample the lithospheric anisotropy, which cannot account alone for the very high delay times measured in station RCBR, and the implications of this to the present-day asthenospheric deformation.

2) Introduction: If you want to link crustal and lithospheric deformation, then it becomes important to make sure that the reader knows about the main events as known from the crust. Therefore I suggest to keep the regional part of the introduction shorter in the introduction- you only need to argue that the province you chose is a nice testing ground for the question asked. (Hence move some of the regional information into the Geological background - this then needs to be more explicit)
We added a phrase explaining why direct observations on the mantle structures and compositions are needed in addition to seismic anisotropy to discuss crust-mantle coupling during major tectonic episodes and shortened the regional part.

3) Chapter 2.1. To help the reader, I strongly recommend to provide a summary table of tectonic events with little comics of structural movement at different times and intrusion - like a table that has the columns time, major tectonic event (name and character (extensional, compression), scale of deformation (10s km, 100 km etc.), igneous activity (yes/no/ what type) - then you can easily refer to different events later - and even a reader not familiar with the area (most readers) will be able to follow your links. Hopefully it will also help to streamline this section. Concentrate on the main events. (modify figure accordingly - see also below).
We added to Figure 1 a time line of the major tectono-magmatic episodes recorded in the crust. We also revised the map and its legend to better convey the temporal evolution.

4) Chapter 2.2.: Is there a possibility to have a summary geophysical diagram that shows the essentials of what we know right now? Alternatively make the geophysical signal clearer in the map please.
We added to Figure 1 magnetic anomaly and seismic tomography maps, which image the structures in the middle crust and the seismic velocity anomalies in the shallow sublithospheric mantle, respectively. We also made the SKS splitting data clearer by enhancing the size of the symbols and presenting it onto both the geological map and on the magnetic anomaly map. This should allow the reader to visualize the relation between crustal structures and seismic anisotropy in the upper mantle.

4) Sampling: In Figure 1, can you make the sampling sites more easy to see - using the abbreviations. Then you can shorten the text and refer the reader to the figure and the table.
5) Chapter 3.1. should then be only half of what it is now, can be easily streamlined by putting GPS data into the table etc.
We enhanced the size of the symbols presenting the sampling locations in Figure 1 and revised and shortened the text of section 3.1 (lines 316-331).

6) Sections 3.1/3.2/3.3. are nicely written and all necessary data needed is there.
7) Why don't you first have the modal percentages and the mineral compositions combined - they belong together. This should also help to streamline the two sections as well.
9) 4.2. - Why not start with the section (current line 479 and following) with the definition of the microstructural types and then provide what makes them typical, again this will help streamline the text and make it easier for the reader. It is easy to get confused. In the whole results section it will be useful to use the microstructure types as anchor points - then the structure is similar in each results section, making it easier for the reader.
We reorganized the data presentation as suggested. It now starts with the presentation of the microstructures (section 4.1), which allow to define the microstructural groups from the start, and use this classification to present the CPO (section 4.2) and composition data (sections 4.3 and 4.4). As suggested by the reviewer, modal compositions are now presented just before the mineral composition data.

For the statistics - for a porphyroclastic microstructure you need to divide the structure and the bulk statistics into two parts the porphyroclasts/blasts and the matrix. This is not done and therefore the statistical values that are provided and plotted in figures are misleading - hence produce two datasets for these microstructure type please. And then replot, it should become much clearer what is going on.
For the fine-porphyroclastic peridotites, we now present the CPO data separately for porphyroclasts and neoblasts (new Figs. 5 and 6). The coarse-porphyroclastic peridotites present a continuous variation in grain sizes and some annealing, which render the distinction of porphyroclasts and neoblasts very difficult. This is now clearly stated in the text (lines 500-501).

Since you have already presented the modal percentages and chemical data, can you please when you describe the microstructures of each microstructural type, also link in the modal percentages and chemistry. This is done in some case, please put it in systematically (just needs a half sentence here and there) - please make sure you refer to the relevant figures
By reorganizing the text, we can now clearly describe the relation or not between microstructures and modal compositions or mineral chemistry. This is done in lines 615-620 and 655-656.
We also now clearly state that there are no relations between sampling site and microstructures, modal compositions, or mineral chemistry. All types are sampled in the Pico do Cabugi and also in the other sampled Macau volcanics (lines 461-467, 612-613, 657-658).

I would make the maps in Figure 2 larger and use some arrows you can then backrefer to in the text).
Figures were re-organized in consequence of the changes in the text and EBSD maps are now presented together with the microstructures in new Fig. 3. This allows to better refer to these maps, which clearly illustrate the olivine and pyroxene grain shapes, in the microstructures description section.

10) Section 4.3. CPOs (see comments on figure 7) nicely done, I notice that in figure 8 you have "recrystallized areas" - is that for the fine porphyclastic ones? Please be explicit - they show a nice trend - so you have the data, show also in Fig. 7 please (did I miss it?) (Just a comment: I wonder how much of the CPO is inherited by metasomatic reactions? This might be its own contribution though - but would be good to know …)
The CPO presentation figures (new Figs. 5 and 6) have been re-designed to clearly present olivine porphyroclasts and neoblasts data for the fine-porphyroclastic peridotites. The

neoblasts orientations are clearly inherited from the neoblasts ones (cf. pole figures in Fig. 6), but there is a strong dispersion, probably due to dynamic recrystallization. One cannot discard the influence of fluids or melts in this recrystallization, but there is no positive evidence for it, such crystallization of other mineral phases in the recrystallized domains (cf. Fig. 3g).

11) Discussion: 5.1. What would trigger the Cenozoic melt percolation? What is the geotectonic setting for that? I am a bit confused, on the one hand you say that the geotherm must be high (based on Figure 11, but then you say that the early equilibrium textures have survived and therefore high geotherms were prevalent in the Mesozoic ? So do the shallower sample - represent relatively recent high geotherm and the deep samples represent an earlier fabric, and an early high T geotherm? Please clarify. It would be good to streamline. Important for seismic interpretation as well …
I think it would be better to have discussion point 5.2 first - as you can use the microstructures to argue for annealing/ long time at high T etc. - please switch around - hopefully it helps to streamline.
We completely reorganized the discussion following the reviewer suggestion. Now it starts by the discussion of the microstructures, then we discuss the thermal constraints and compare them to geophysical data and calculated melting conditions for the last two magmatic episodes, compare the seismic properties of the samples to seismic anisotropy data, and, at last try to use all this information to relate the mantle and crustal evolutions.
Concerning the questions above: the equilibrium temperatures and absence of garnet despite fertile compositions imply a rather hot geotherm in the Cenozoic, which is consistent with the calculated melting conditions for the most primitive Macau volcanics. Both datasets imply a hotter than normal sublithospheric mantle. Geophysical data points to a hotter than normal sublithospheric mantle nowadays. One may infer therefore that the present-day conditions persist since the Cenozoic. For the pre-Cenozoic thermal state, the only constraints we have are the calculated melting conditions for the most primitive Cretaceous basalts of the Ceara-Mirim dykes indicate still shallower partial melting. Based on these data, we suggest that the lithosphere-asthenosphere boundary might have been shallower in the Cretaceous. In conclusion, the shallower samples represent old lithospheric mantle, but the deeper ones might represent material accreted to the lithosphere by cooling since the Cretaceous. We have re-written this section of the discussion (lines 1073-1088) to clarify this point.

12) 5.2. I think it would be best to go through the three microstructural types and discuss their general features, with a bit of "outliers" - but really you want to emphasis the general trends. Many of the arguments you bring up in the microstructures part you can directly link to the geotherm - so switch 5.1. and 5.2. around. If you show the matrix versus porphyroclast data - then you can discuss here in more detail, it will help in setting up the evolution of these samples better.
Done, see answer to previous point

13) 5.3. I think you should take this part out, not needed - alternatively, shorten considerably - just point out the main difference relatively uniform versus high variations in your studied samples.
We have eliminated this section as suggested. However, we kept the oceanic samples in Fig. 2, since we use the comparison in the annealing degree between the FN samples, for which we can infer a maximum age for their accretion to the lithosphere and hence for the freezing of the microstructures, with the one measured in the Borborema peridotites to try to constrain the age of the deformation frozen in the coarse-granular and coarse-porphyroclastic peridotites from the continental domain (lines 1194-1199 & 1242-1257).

14) 5.4. Nice section - just rewrite a little bit keeping the big question in mind.
15) 5.5. this is the BIG story discussion, all other discussion sections (5.1.-5.4) should be written to feed into this one. Currently you do not "feed" off a) the metasomatic story, b) the geotherm story - If the geotherm seen is Mesozoic and cenozoic - then how is the Neoproterozoic structure preserved - are the hT only static with very little deformation? Maybe the only deformation signature is actually the melt percolation and annealing, but no CPO development? This section needs a major rehaul, there is a lot more in there, thinking about what can trigger mantle metasomatism - and when in the annealing and deformation history of the xenoliths that metasomatism is inflicted should provide some pinpoints for a relative time - melt percolation - deformation - annealing path. If you can construct these for the three main microstructure types then I think you have a nice story, you have done that half or 2/3rd of the way, but it needs to be clear and explicit. This discussion part will feed directly in rephrasing and restructuring the other discussion parts.

Neoproterozoic structures are preserved in the shallow part of the lithospheric mantle, which after the Neoproterozoic deformation have only been affected by annealing and minor (localized) reactive melt percolation leading to refertilisation - the coarse-granular peridotites. Neither of these processes produces major changes in the olivine CPO.

The few low-temperature coarse-porphyroclastic samples might record more recent deformation, but strains are probably small and have not significantly modified the CPO. This last interpretation is based on two observations: (1) the lack of evidence for any high-stress, low-temperature (<1000°C), high-strain deformation in the studied sampling (considering that the geotherm in the Mesozoic was only slightly hotter than the Cenozoic one, temperatures in the shallow section of the lithospheric mantle would not have been very different) and (2) the seismic anisotropy data derived from both SKS splitting and anisotropic receiver functions, which point to a fabric subparallel to the Neoproterozoic crustal structures in the lithospheric mantle.

This section of the discussion has been reorganized and extensively re-written. The points above are presented in the discussion lines 1223-1265.

16) Conclusions - largely fine, but needs some reworking after 5.5. is redone.

Done.

Figures:

Figure 1: Nice figure, but you need to add the tectonostratigraphic event table - Ideally you can link the two through numbers or colours (I think it will be worth the effort)

We added to Figure 1 a time line of the major tectono-magmatic episodes recorded in the crust. We also revised the map and its legend to better convey the temporal evolution. We also added maps of the geophysical data illustrating the continuation of the Neoproterozoic structures in the middle crust and seismic velocity anomalies which point to higher than normal temperatures in the sublithospheric mantle temperature beneath the study area.

Figure 2. I am not sure that you need both figure 2a and b, they show the same data twice, I would opt for 2b. Then you can have the legend bigger so that it is legible. The white writing on the maps is intelligible, please make maybe black writing with a white background

We have completely reorganized the order of figures to follow the new order of presentation of the data. The old Fig. 2, which is now Fig. 7 has been strongly simplified, since now the EBSD phase maps are presented together with the microstructures. We kept nevertheless the ternary diagram as an insert, since it is the most traditional way to present peridotites modes and as it is now, it does not use supplementary space.

Figure 3. No need in the manuscript (can be supplementary)
Deleted. Grain sizes are presented in Table 2.

Figure 4-5. Please use some extra arrows to point out specific features, e.g. irregular boundaries between different phases (CPX-Ol) if there are subgrains (I assume you have the EBSD data for each of these datasets - then point out these out - why not make for each one a little inset showing an EBSD map with typical GOS and subgrain boundaries marked. This would help a lot in the discussion and the understanding of the reader what you are focussing on. Will also help to streamline the text.
These figures, which are now Fig. 3 and 4 have been extensively revised. For lack of space, we do not show intragranular misorientation maps for all microstructures. However, we do it in Fig. 3 for the fine-porphyroclastic microstructures, where the contrast in intragranular misorientations between porphyroclasts and neoblasts is well marked.
We also added arrows to mark the most important features, such as 120° triple junctions, subgrains, and pyroxene shapes, in the detail microphotographs in Fig. 4.

Fig. 7 Can you add to each sample the modal percentages of each phase (could be put for example below sample no. Note: If you divide up the porphyroclstic ones into two data sets each, you will have to plot them separately, I think this will be very informative and maybe a good way to look through the last deformation - so you would get a CPO history?! Would be worth checking out?!
We did not add the modal percentages to this figure (now Fig. 6) because it is already crowded. The modal percentages for all samples are presented in Table 1.
As required, we now present separately the olivine CPO for porphyroclasts (points) on top of the neoblasts CPO (contours) for the fine-porphyroclastic peridotites. This allows to clearly observe the orientation inheritance relations, but higher spread of the neoblasts orientations.

Figure 9. They are very small, I think you could put the spinel related figures into supplementary and make the other larger, then it is easier for the reader to see and relate to text.
Done. This is now Fig. 8 and spinel graphs are now Supplementary Material Fig. S1.

Figure 10. There is too much data on it - trends (or lack of) are hard to see. I suggest that you take our the literature as point data, but show them as fields that underlie your data. What are the open circles and squares? It becomes then much clearer that the fine porphyrclastic ones are distinct, while the other ones show a large range.
We now only present Macau peridotites data in this figure (now Fig. 9). Moreover, the use of colors, instead of gray level, allows as in the other figures, to better distinguish the present study data from the literature. In choosing the colors we paid attention that when printed in gray levels the symbols for the different microstructures could still be distinguished.

Hope this helps to make this manuscript even better,
Best wishes,
Sandra Piazolo

28 Feb, 2019

Manuscript Number: TECTO13230
Title: The lithospheric mantle in a continental domain submitted tomultiple tectonic events: Peridotite xenoliths from the BorboremaProvince, northeast Brazil
Authors: Liu et al.

This manuscript reported microtextures, CPO and major element compositions of mantle xenoliths from the Northern Borborema Province. The authors discussed P-T conditions and deformation-metasomatic history of the xenoliths, and finally discussed tectonic evolution of the studied mantle. The data quality is high, and interpretations and discussions are reasonably supported by their data coupled with previous data sets. The contents of the manuscript contain significant contributions to a link between petrological observations and geophysical interpretations. My decision for the present manuscript is, therefore, acceptable with minor revisions. To strengthen the manuscript, it might be better to discuss/describe two points before the authors go to discussions: (1) effects of infiltration of the host melt and (2) effects of heterogeneity of modal abundances for modal estimation.

1) Effects of infiltration of the host melt

Although the authors mentioned "Most xenoliths are small (on average 3 cm of diameter), but they are very fresh and display no macroscopic evidence for major interaction with the host lava. However, interstitial veins of altered glass, up to a few microns wide and often visible only by SEM, which could be sometimes followed to the contact with the basalt, were described in some xenoliths, such as AG6, AG7,"(307-311 lines), it is better to describe a bit more carefully what are fine-grained parts in deformed samples. According to Fig. 5., effects of infiltration of the host basalt are likely commonly observed (red arrows below).

The reviewer is 100% correct. The xenoliths are small and the effects of infiltration of the basalt, in particular close to the borders of the xenoliths, were understated in the submitted version of the ms. We have re-written this paragraph (lines 331-338) to clearly describe them and to state that the zones that displayed, under the microscope, any evidence for such reactions were carefully avoided in the chemical analyses and that this melt infiltration does not affect the microstructural data, because it concerns very small areas.

Especially, AG6, a deformed one, would be highly affected by infiltration of the host basalt. Please describe mineral assemblages in fine-grained part in deformed sample (AG6 for example), whether or not glass presents. Any hydrous minerals? If hydrous minerals are in the fine-grained parts, the discussions might be changed. I just want to make sure that the fine-grained parts were formed by deformation rather than melt-rock interactions. I almost believe that the former (deformation) would be a case for the studied samples.

The recrystallized domains in the fine-porphyroclastic peridotites are clearly distinct from the basalt infiltration ones. To better show this we added in the new Fig. 3 a detail EBSD phase map of such a domain in AG6, which clearly shows that the domain is composed solely by recrystallized olivine, with neither interstitial pyroxenes nor amphiboles that would have crystallized in response to melt rock interactions. Moreover, comparison of the olivine CPO of porphyroclasts and neoblasts, which are now plotted separately in the new Fig. 6 show that the two CPO are related, pointing to orientation inheritance, which is expected for recrystallization, but not for crystallization from a melt under static conditions.

2) Mineral mode estimation

Mineral mode is a key to estimate physical properties of the samples. However, because of large grain size and macroscopic heterogeneity in thin section scale, mineral modes in the manuscript is OK for the thin sections, but might need care to estimate representative mineral

mode for the mantle in the studied area. For instance, samples of CA14 and CA11 in Fig. 2 are very heterogeneous in mineral distributions. If we measure modal abundances of left half of the samples, mineral mode would be significantly different from the right half.
I would like to ask the authors to describe/discuss the effects of uncertainly in mineral mode for further discussions.
We agree that determination of mineral modes in such small samples is problematic, since mantle rocks are often compositionally heterogeneous. However, this is the best we can do given the size of xenoliths carried by these basalts. The only solution is to multiply the number of samples. Comparison with the present dataset with previous ones (which suffered from the same shortcomings) suggests, nevertheless, that the present sampling may be representative of the modal composition range in the lithospheric mantle in the region.
Yet, because of the uncertainty in the determination of the modal composition of the individual samples, we only discuss the trends and use average samples for the calculation of seismic properties and comparison with the seismological data.

Minors:
266 lines typo
Significant digits for numbers in tables
Please consider significant digits for numbers in all tables. For instance, is it necessary to display the second decimal place for modal volume of minerals in Table 1?
Thanks for the remark. This was clearly our mistake. We have revised all tables to only show significant digits.

I hope these comments would improve the revised version of the manuscript.
Best regards, Tomo MORISHITA, Kanazawa University

Highlights:

- Mainly coarse-granular and porphyroclastic peridotites with [100](010) olivine textures
- Equilibrium temperatures consistent with a 80 km thick lithosphere in the Cenozoic
- Extensive annealing implies that deformation frozen in the shallow mantle is 100s Ma old
- Mantle fabric related to Neoproterozoic shear zones may partially explain SKS splitting
- Limited reworking of the lithospheric mantle during Cretaceous rifting

Crust-mantle coupling during continental convergence and break-up: Constraints from peridotite xenoliths from the Borborema Province, northeast Brazil

Shiran Liu[1,2], Andréa Tommasi[1], Alain Vauchez[1], Maurizio Mazzucchelli[3]

[1]Géosciences Montpellier, CNRS & Université de Montpellier, Montpellier, France.
[2]Key Laboratory of Orogenic Belts and Crustal Evolution, School of Earth and Space Sciences, Peking University, Beijing, China.
[3]Dipartimento di Scienze Chimiche e Geologiche, Università di Modena e Reggio Emilia, Modena, Italy.

Corresponding author: Shiran Liu (hbhslsr@gmail.com), Andréa Tommasi (andrea.tommasi@umontpellier.fr)

Keywords:
Subcontinental mantle lithosphere
Crust-mantle coupling
Melt-rock interaction
Olivine crystal preferred orientation
Seismic anisotropy

Highlights:

- Mainly coarse-granular and porphyroclastic peridotites with [100](010) olivine textures
- Equilibrium temperatures consistent with a 80 km thick lithosphere in the Cenozoic
- Extensive annealing implies that deformation frozen in the shallow mantle is 100s Ma old
- Mantle fabric related to Neoproterozoic shear zones may partially explain SKS splitting
- Limited reworking of the lithospheric mantle during Cretaceous rifting

Abstract

We studied a suite of mantle xenoliths carried by Cenozoic volcanism in the Borborema Province, NE Brazil. These xenoliths sample a subcontinental lithospheric mantle affected by multiple continental convergence and rifting events since the Archean. Equilibrium temperatures indicate a rather hot geotherm, implying a ca. 80 km thick lithosphere. Most xenoliths have coarse-granular and coarse-porphyroclastic microstructures, recording variable degrees of annealing following deformation. The high annealing degree and equilibrated pyroxene shapes in coarse-granular peridotites equilibrated at ~900°C indicate that the last deformation event that affected these peridotites is several hundreds of Ma old. Coarse-porphyroclastic peridotites equilibrated at 950-1100°C probably record younger (Cretaceous?) deformation in the deep lithospheric mantle. In addition, a few xenoliths show fine-porphyroclastic microstructures and equilibrium temperatures ≥1200°C, which imply a recent deformation, probably related to the dykes that fed the Cenozoic volcanism. Chemical and microstructural evidence for reactive percolation of melts is widespread. Variation in textural and chemical equilibrium among samples implies multiple melt percolation events well spaced in time (from Neoproterozoic or older to Cenozoic). Crystal preferred orientations of olivine and pyroxenes point to deformation controlled by dislocation creep with dominant activation of the [100](010) and [001]{0kl} slip systems in olivine and pyroxenes for all microstructures. Comparison of xenoliths' seismic properties to SKS splitting data in the nearby RCBR station together with the equilibrated microstructures in the low-temperature xenoliths

point to coupled crust-mantle deformation in the Neoproterozoic (Brasiliano) continental-scale shear zones, which is still preserved in the shallow lithospheric mantle. This implies limited reworking of the lithospheric mantle in response to extension during the opening of the Equatorial Atlantic in the Cretaceous, which in the present sampling is restricted to the base of the lithosphere.

1. Introduction

Continental plates have long-lived histories. They are usually composed by crustal domains with varied tectonic ages. Tectonic reworking is a common feature in crustal exposures. Yet, major tectonic events such as convergence, collision, and rifting involve the entire plate, not only the crust. By consequence, large volumes of the subcontinental lithospheric mantle must have been affected by a succession of tectono-thermal events (cf. reviews in Tommasi and Vauchez, 2015; Vauchez et al., 2012). In addition, during orogenic events, the strain regime frequently changes across the belt, with contiguous domains accommodating transcurrent motions and others accommodating thrusting for instance. However, how the deformation is accommodated in the lithospheric mantle and the level of coupling between crust and mantle deformation during these major tectonic episodes are still matter of debate.

Comparison between SKS splitting data and crustal structures points to coherent kinematics, implying at least partial coupling between the crust and the mantle in many orogenic belts (Tikoff et al., 2004). As recognized since the early times of seismic anisotropy measurements (e.g., Vauchez et al., 1991), crust-mantle coupling is well documented beneath large-scale strike slip faults and transpressional belts, such as the San Andreas fault (Bonnin et al. 2012) or the Pyrenees, the Appalachians, and the neoproterozoic Ribeira-Aracuai belt of SE Brazil (cf. review in Vauchez et al., 2012). In contrast, in collisional domains submitted to large amounts of thickening, like the Alps and the Southern Tibet, or in active continental rifts, such as the East African rift system, polarization directions of fast split SKS or SKKS waves are usually parallel to the trend of the belts or rifts, but at high angle to the lineations marking flow directions in the ductile crust and to the slip directions in active faults (e.g., Barruol et al., 2011; Wu et al., 2015; Hammond et al., 2014). This suggests at least partial decoupling between the crust and lithospheric mantle (Tommasi et al., 1999).

However, seismic anisotropy data only offer indirect information on the present-day structure of the upper mantle. Moreover, unless a variety of methods based on waves with different incidence angles and propagation directions are employed, localizing vertically the source of the anisotropy remains difficult. Analysis of mantle xenoliths, which are mantle fragments (peridotite xenoliths) carried to the surface by volcanic episodes, allows for direct sampling of the lithospheric mantle. This sampling is imperfect: it is discontinuous, non-oriented, and focused along the magmatic conduits.

Nevertheless, the characterization of the microstructures and associated crystal preferred orientations, as well as of the chemical compositions and mineralogy of the mantle xenoliths, allows determining the relative deformation, annealing, and petrological (partial melting, reactive melt transport, solid-state reequilibration) history, even if no dating is possible. Coupling petrophysical analyses on mantle xenoliths to seismological data may allow better constraining the deformation history of the lithospheric mantle and hence discussing crust-mantle coupling during major tectonic events.

In this article, we present a petrostructural study of peridotite xenoliths entrained by Cenozoic volcanism in NE Brazil. Based on these data and on published SKS splitting measurements (Assumpção et al., 2011; Bastow et al., 2015), we try to unravel the tectono-thermal evolution of the continental lithospheric mantle in this region, which has been affected by multiple collisional and extensional episodes since the Archean. Analysis of the presently outcropping crustal structures highlights a series of tectono-magmatic episodes, among which the most important and recent ones are: (i) extensive intraplate deformation in a convergent setting, which produced a continental-scale system of strike-slip shear zones and transpressional belts accommodating lateral escape of this domain during the formation of the Gondwana and (ii) extension, localized in a series of intracontinental basins, during the early stages of the opening of the Equatorial Atlantic.

2. Geological and geophysical background

2.1 Evolution of the Northern Borborema Province (NBP)

The analysis of the crustal rocks outcropping in the Northern Borborema Province (NBP) points to a complex tectonic evolution, which probably started in the Archean, as indicated by U-Pb ages ranging from 3.4 to 2.7 Ga recorded in the São José Massif (Souza et al., 2016), ca. 100 km to the east of the study area and in smaller nuclei elsewhere in the province. Between 2.1-2.4 Ga, a major crust formation event produced ca. of the 50% of the present-day outcropping rocks (Hollanda et al., 2011; Souza et al., 2016). The tectonic setting for this extensive magmatic activity is discussed, but isotopic data indicates significant recycling of pre-existing crustal material (Hollanda et al., 2011).

The Meso- to Neoproterozoic evolution of the Borborema Province is characterized by a series of failed intracontinental rifting episodes. At 1.8-1.9 Ga, the Orós and Jaguaribe volcano-sedimentary basins formed to the west of the study area (Fig. 1). Localized extension was accompanied by intrusion of small volumes of alkaline granites and anorthosites elsewhere in the province, which extended until 1.75 Ga (Sa et al., 1995; Hollanda et al., 2011). At 1-0.9 Ga, extension affected the central Borborema Province (Santos et al., 2010; Van Schmus et al., 2008). The last Proterozoic extensional episode affected most of the province and formed the Seridó basin within the study area (Fig. 1).

The youngest sedimentation in this basin occurred at ~630-615 Ma, but early sedimentation may be as old as 1.8 Ga (Hollanda et al., 2015), suggesting an early rifting episode simultaneous with the formation of the Orós and Jaguaribe basins.

The major tectono-magmatic episode that affected the Borborema Province, shaping its present-day geology, is, however, the compressional Brasiliano event between 595-540 Ma (Neves, 2003; Archanjo et al. 2008; Viegas et al., 2014). This event resulted in extensive tectono-thermal reworking of the province through the formation of a continental-scale transcurrent shear zone system – the Borborema shear zone system, transpressional inversion of the Proterozoic metasedimentary basins, and widespread emplacement of granitoids (Fig. 1). The granitoids geochemistry indicates a dominant component of crustal reworking (Neves, 2003; Souza et al., 2016), implying an intraplate setting for the Brasiliano deformation, with a possible convergent plate boundary > 500 km to the NW from the study area (e.g., Caby et al., 1991; Ancelmi et al., 2015). The complex network of anastomosing E-W and NE-SW trending ductile dextral strike-slip shear zones, some up to ~25 km wide, and transpressional belts deformed under high temperature, low pressure conditions that compose the Borborema shear zone system (Vauchez et al., 1995) is therefore the expression of strain localization in an intraplate setting controlled by large-scale intraplate rheological heterogeneities (the basins) in response to the convergence between São Francisco, Amazonian, and West African cratons during the construction of the Gondwana (Tommasi et al., 1995). This shear zone system allowed for tectonic extrusion of the Borborema Province towards the NE (Ganade de Araújo et al., 2014, 2016), that is, towards the Saharan province, which, like Borborema, had been weakened by tectono-magmatic activity during the Meso- and Neoproterozoic.

In the early Cretaceous, the Borborema province experienced regional extension before rifting localized at the present location of the equatorial Atlantic Ocean (Darros de Matos, 1999). Structures associated with these early stages of rifting in the northern Borborema Province include several intracontinental basins or aborted rifts and a large tholeiitic dyke swarm. The basins formed as NW-SE trending asymmetric grabens (e.g., Potiguar, Rio do Peixe, Araripe in Fig. 1) controlled by reactivation of the Brasiliano shear zones (Darros de Matos, 1999; Castro et al., 2007, 2012; Marques et al., 2014). They contain dominantly continental sediments of fluviatile and lacustrine origin, which attain thicknesses of 2000 m, deposited between 145-125 Ma. The Potiguar basin is the best developed among these basins; its offshore domain is the only one involved in the final opening of the Atlantic. The Ceará-Mirim dyke swarm is a >350-km-long tholeiitic dyke swarm with a dominantly E-W trend that rotates to NE-SW at the southern termination of the Potiguar basin (Fig. 1). The dykes have ages between 135 Ma and 120 Ma (Hollanda et al, 2018 and references therein). Their emplacement is therefore synchronous to

the formation of the intracontinental basins. Geochemical data points to primary magmas formed by melting of an enriched mantle (EMI ± FOZO isotopic signatures) at shallow depths (<90 km; Ngonge et al., 2016).

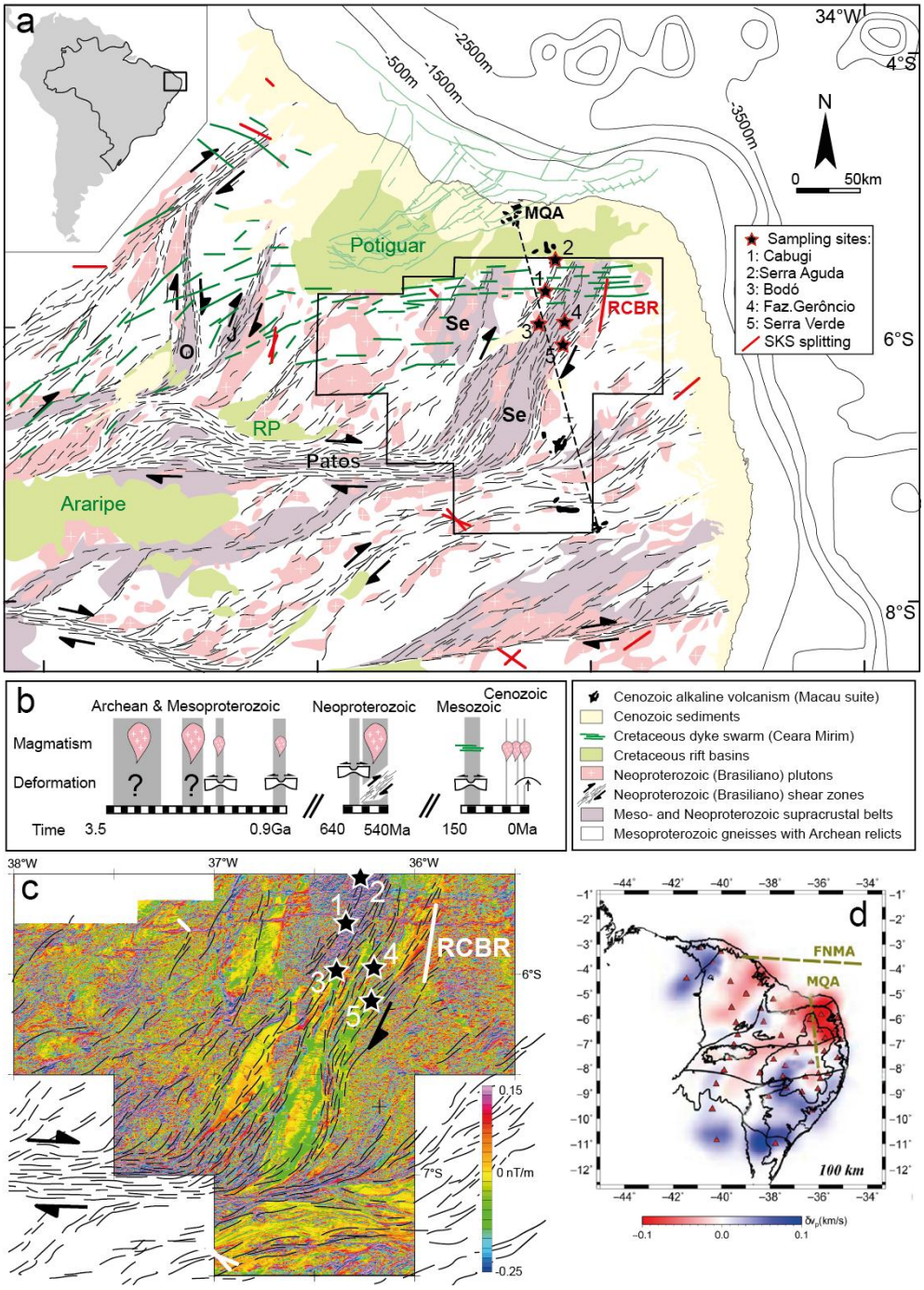

Fig. 1. (a) Simplified geological map (after Vauchez et al., 1995 and Oliveira and Medeiros, 2018) displaying xenolith sampling locations. (b) Time line of the major tectono-magmatic events in the Borborema Province. (c) Aeromagnetic anomalies map (1st vertical derivative; Costa et al., 2016) imaging middle crust structures in and around the Seridó belt. (d) P-wave tomography model for the Borborema Province at 100 km depth (Simões Neto et al., 2018) characterized by a marked low velocity anomaly east of the Macau-Queimadas volcanic alignment (MQA) and north of the Patos shear zone. SKS splitting data in (a) and (c) from Assumpção et al. (2011) and Bastow et al. (2015). RP: Rio do Peixe

Cretaceous basin. Se: Seridó, O:Orós, and J: Jaguaribe supracrustal belts.

The Cenozoic is characterized by a long-lived, but small-volume alkaline volcanism (both onshore and offshore), tectonic inversion of the Mesozoic intracontinental basins, and uplift of the Borborema Plateau. The entire Borborema Province sits nowadays on average at ~800m above the sea level and the Araripe basin is topographically more than 500 m above the Precambrian basement. Analysis of river profiles implies that most uplift occurred within the last 30 Ma (Tribaldos et al., 2017), but earlier events may have occurred (Marques et al., 2014; Nogueira et al., 2015). The present day crustal thickness of 30-35 km implies some degree of sub-lithospheric support for the uplift. The offshore Cenozoic volcanism forms an E-W volcanic alignment that extends from the Ceará coast in northeast Brazil (the Mecejana volcanic field) to the Fernando de Noronha archipelago. The Mecejana volcanics yield K-Ar ages between 26 and 44 Ma (Mizusaki et al., 2002), whereas volcanism in Fernando de Noronha has Ar-Ar ages between 12.5 and 6 Ma (Perlingeiro et al., 2013). The onshore Cenozoic volcanism is distributed along a N-S trend, forming the Macau–Queimadas Alignment (MQA, Fig. 1). Emplacement ages range between 52 Ma and 7 Ma, with two peaks around 26-29 Ma and 7-9 Ma and no clear age progression along the MQA (Souza et al., 2003; Silveira 2006; Knesel et al., 2011).

The Macau volcanics that entrained the studied mantle xenoliths (Fig. 1) erupted onto metasediments from the Neoproterozoic Seridó belt or Mesoproterozoic gneisses that form their basement. In the study area, the Brasiliano event is recorded by multiple NE-SW shear zones, which branch off from the E-W Patos shear zone in the south, by transpressional structures in the Seridó belt, and by intrusion of granitoids. The Cretaceous Ceará-Mirim dyke swarm crosscuts the study area with an E-W trend and the Potiguar basin outcrops to the north and west of it (Fig. 1).

2.2 Geophysical data

P-wave receiver functions, deep seismic refraction experiments, and surface-wave dispersion data indicate that the crust is 30 ~ 32km thick in the northern Borborema Province, but 36 ~ 38 km thick in the southern part of the province (Oliveira and Medeiros, 2012; Almeida et al., 2015; Lima et al., 2015; Luz et al., 2015). This variation in crustal thickness is consistent with gravity data (Oliveira and Medeiros, 2018) and correlated with topography: elevated regions show thicker crust. Receiver function data also imply an intra-crustal discontinuity at 9-18 depth, most often observed in domains with thinner crust, such as the area sampled by the studied xenoliths (Almeida et al., 2015).

Gravity and magnetic data illuminate the structuration of the deep crust in the Borborema province (Oliveira and Medeiros, 2018). These data establish the Patos, Pernambuco, and Jaguaribe shear zones as major structures, which splay of from the Transbrasiliano Lineament, separating four crustal blocks with different geophysical characteristics: the Southern, the Transversal,

the Ceará, and the Rio Grande do Norte domains. The studied xenoliths sample the mantle beneath the Rio Grande do Norte domain, which is delimited by the Jaguaribe and Patos shear zones to the west and south, and by the Atlantic Ocean to the north and east. This domain is characterized by strong magnetic contrasts with E-W or NNE trends, correlated with the outcropping Brasiliano structures (Fig. 1c). Magnetic anomalies also clearly define the Ceará-Mirim dykes (Fig. 1c). In addition, analysis of the Bouguer gravity anomaly shows that most of the Rio Grande do Norte domain is characterized by weak long wavelength positive anomalies, which follow the trend of the coastline (cf. Fig. 7 of Oliveira and Medeiros, 2018), suggesting that crustal thinning related to the Atlantic opening affected most of the domain.

The first kilometers of the lithospheric mantle structure may be probed by the analysis of Pn velocities, which decrease from 8.1 km/s to 7.9 km/s in a NW-SE refraction profile across the Borborema Province to the south of the study area (Lima et al., 2015). In the vicinity of the study area, Pn velocities are ~8.0 km/s, which for an isotropic mantle with a spinel-lherzolite composition would correspond to sub-Moho temperatures of 700-750°C (Schutt et al., 2018).

No seismic velocity data is available for the deeper sections of the lithospheric mantle, but a recent P-wave regional travel-time tomography model (Simões Neto et al., 2019) imaged slower than average velocities at depths <150 km in the northeastern Borborema province, just east of the study area (Fig. 1d). This low velocity anomaly coincides with a local geoid anomaly of +10 m (Ussami et al. 1999). Slower than average P-wave velocities in the shallow mantle beneath the study area are coherent with a rather shallow Lithosphere Asthenosphere boundary (LAB), estimated at 80 km depth based on S receiver function data from the station RCBR (Heit et al., 2007). The results of the regional P-wave tomography for the northeastern Borborema Province are also consistent with global finite-frequency tomography models, which image lower than average S-wave velocities in the mantle at 250-km depth in this region (French et al. 2013).

SKS splitting data in the Borborema Province (Bastow et al., 2015) show a complex pattern, with highly variable delay times and fast polarization directions, which in some places closely follow the Neoproterozoic crustal fabric, but are oblique to it in others (Fig. 1a,c). The station closest to the xenolith sampling sites, RCBR (Fig. 1a,c), shows a NNE-oriented fast S-wave polarization subparallel to the Brasiliano transpressive structures, which structure the northern Seridó belt and its gneissic basement, and a high delay time (1.9±0.2 s) based on 9 individual measurements (Assumpção et al., 2011).

2.3 Previous studies of Macau peridotite xenoliths

The petrology and the geochemistry of Macau mantle xenoliths were

studied by Comin-Chiaramonti et al. (1986), Princivalle et al. (1994), Fodor et al. (2002), Rivalenti et al. (2000; 2007). These studies identified two microstructural groups: protogranular (the dominant type) and (rare) porphyroclastic (partially recrystallized) peridotites. Protogranular microstructures are mainly observed in lherzolites, whereas porphyroclastic microstructures are usually observed in harzburgites. Protogranular peridotites also yield lower two-pyroxene equilibrium temperatures (825±116°C) than porphyroclastic ones (>1150°C). Trace-element patterns and isotopic compositions of the peridotites indicate variable degrees of metasomatism by alkali-basaltic melts with EMI and minor EMII isotopic signatures, probably during multiple metasomatic events (Rivalenti et al., 2000, 2007).

3. Methods

3.1. Sampling

We have studied 22 xenoliths from 5 different Macau volcanic sites, which extend in a rough N-S trend, from the limit of the Potiguar basin to ~70 km south of it (Fig. 1). Most xenoliths analyzed in the present study come from the Pico do Cabugi basaltic neck (5°42.3'S, 36°19.4'W). The Pico do Cabugi basalts yield Ar-Ar ages 24.6 ± 0.8 Ma (Souza et al., 2003 and references therein). Among the 16 xenoliths of the Pico do Cabugi in this study, 14 (marked as CA) have been collected by the authors in a field campaign in 2016 and two (marked as PC) were previously studied by Rivalenti et al. (2000).

We also analyzed 6 xenoliths previously studied by Rivalenti et al. (2007): two from the Serra Aguda neck (AG, 5°31'S, 36°17'W), ~30 km north of the Pico do Cabugi, at the border of the Potiguar basin (Fig. 1), one from the Serra Preta do Bodó dykes (BO, 5°58'S, 36°22'W), ~20 km south of Pico do Cabugi, and four from Fazenda Geroncio (GR, 5°58'S, 36°14'W) and Serra Verde localities (SV, 6°06'S, 36°12'W), located ~30 and ~50 km south of Pico do Cabugi (Fig. 1). There are no ages for the Fazenda Geroncio and Serra Verde volcanics, but the Serra Aguda basalts were dated at 26 Ma (Silveira, 2006) and those at Serra Preta do Bodó, at 7.1 Ma (Knesel et al, 2010).

Most xenoliths are small (on average 3 cm of diameter), but they are very fresh. The samples display no macroscopic evidence for major interaction with the host lava. However, small pockets of fine-grained clinopyroxene, spinel, and olivine, as well as melt films along grain boundaries were observed under the microscope, in particular close to the borders of many xenoliths. In addition, some xenoliths have pyroxenes with spongy borders, indicative of limited partial melting during extraction. These domains were carefully avoided during microprobe analyses. They were sometimes included in the EBSD analyses, but affect weakly the results because of their small area.

3.1 Electron-backscattered diffraction (EBSD) data acquisition and treatment

Petrostructural analyses were performed on all samples. Crystallographic preferred orientations (CPOs) of olivine, pyroxenes, and spinel were measured

by indexing of electron-backscattered diffraction patterns in the SEM-EBSD facility at Geosciences Montpellier, France. Data acquisition was performed using a JEOL JSM 5600 scanning electron microscope with 17kV acceleration voltage and 24mm working distance. We performed EBSD mapping over the entire thin section (areas ≥ 2x3 cm^2) with step sizes between 14µm and 35 µm, depending on grain size. Indexation rates varied between 84% and 97%. Non-indexed points correspond mainly to fractures. During post-acquisition data treatment, we eliminated inaccurate indexing points (MAD > 1.3° and wild spikes), corrected for rare olivine pseudo-symmetry misindexing, and filled up non-indexed pixels with at least 6 coherent neighboring measurements with the average of the neighbors' orientations.

The CPO data analysis, that is, the calculation of the orientation distribution functions (ODF) and of the misorientations, the computation of the strength and symmetry of the olivine CPO, the plotting of pole figures, and the quantification of the microstructure (grains' size, shape, and orientation) was performed using the MTEX toolbox in Matlab (http://mtex-toolbox.github.io/; Hielscher and Schaeben, 2008; Bachmann et al., 2010; Bachmann et al., 2011). The ODFs were calculated using a "de la Vallée Poussin" kernel function with a half-width of 10°. The CPO is presented as one crystallographic orientation per pixel in pole figures (lower hemispheric stereographic projections). Thin sections were cut in random orientations, because of the small size of the xenoliths. To facilitate comparison between samples, we rotated the CPO of all samples into a common reference frame, in which the maximum concentration of [100] of olivine is parallel to the E-W direction and the maximum concentration of [010] axis of olivine is parallel to the N-S direction of the pole figure. The choice of this reference frame can be justified a-posteriori by the analysis of the CPO, which indicates that this reference frame probably corresponds to the lineation and normal to the foliation directions (cf. discussion).

The strength of the CPO was quantified using the dimensionless J-index (Bunge, 1982). The J-index for a random CPO is 1; it can reach up to 20 in natural peridotites, with a peak at 3-5 (Tommasi and Vauchez, 2015). We use the dimensionless BA-index, based on the eigenvalues of the [100] and [010] axes orientation distributions (Mainprice et al., 2014), to characterize the olivine CPO symmetry. This index allows classifying the olivine CPO into three types: (i) fiber-[010], characterized by a [010] point maxima and girdle distributions of [100] and [001] (BA-index < 0.35), (ii) orthorhombic, characterized by point maxima of [100], [010], and [001] (0.35 < BA-index < 0.65) and (iii) fiber-[100], characterized by a point maxima of [010] and girdle distributions of [010] and [001] (BA-index > 0.65). J- and BA-indexes do not depend on the reference frame.

To analyze quantitatively the microstructure, we used the grain detection method in MTEX (Bachmann et al., 2011) defining grains boundaries by misorientation angles between adjacent pixels higher than 15°. Grains

composed by less than 10 pixels were not considered in the microstructural analysis. The misorientation of each pixel relative to the mean orientation of the grain (M2M) and the grain orientation spread (GOS) were calculated to quantify the intracrystalline orientation gradients, which are a proxy of the dislocation density. In addition, we characterized the sinuosity of the grain boundaries by the shape factor, which is the ratio of the perimeter of the grain over the perimeter of a circle with the same area. Both the intra-granular misorientation (M2M and GOS) and the sinuosity of grain boundaries (shape factor) should decrease in response to recrystallization.

3.2 Mineral compositions and equilibrium temperatures

Mineral compositions of olivine, orthopyroxene, clinopyroxene, and spinel were analyzed in ten samples, selected based on their microstructure, so that all microstructural types were represented. Measurements were performed in a Cameca SX100 electron microprobe at the Microsonde Sud facility at the University of Montpellier, France at a 20kV accelerating voltage and a 10nA current. For each sample, we analyzed both rim and core composition in 3 to 4 grains for olivine, orthopyroxene, clinopyroxene, and spinel.

We calculated equilibrium temperatures based on the clinopyroxene-orthopyroxene geothermometer (Taylor, 1998) and on the Ca-in-opx geothermometer (Brey and Kohler, 1990; revised by Nimis and Grutter, 2010). Average rim and core equilibrium temperatures were calculated by averaging the temperatures calculated using 3-4 rim or core compositions of individual opx grains or opx-cpx pairs for each sample. Since no reliable barometers are available for spinel-facies peridotites, we chose arbitrarily 1.5 GPa (~46 km depth) as the pressure to calculate the two thermometers. Changes in the assumed pressure produce a variation of ~10 °C per 0.5 GPa (~11 km).

3.3 Seismic properties

Seismic properties of each sample were computed using the MTEX toolbox (Mainprice et al., 2011), using Voigt-Reuss-Hill averaging based on the CPOs and modal content of olivine, orthopyroxene, and clinopyroxene derived from the EBSD maps and on the single crystal elastic constant tensors of the three minerals and their temperature and pressure derivatives (Abramson et al., 1997; Anderson et al., 1992; Chai et al., 1997; Isaak et al., 2006; Jackson et al., 2007; Sang and Bass, 2014). Average seismic properties for the lithospheric mantle beneath the study area were estimated by averaging the elastic constant tensors of all samples with all CPO data rotated into a common reference frame. The assumption is that the orientation of the lineation and foliation is constant both laterally and vertically. The average seismic properties provide therefore an estimate of the maximum seismic anisotropy that could be produced, if the xenolith sampling is representative of the variability of compositions and CPO in the lithospheric mantle beneath the

studied area.

4. Data

4.1 Microstructures

Previous studies (Fodor et al., 2002; Rivalenti et al., 2000; Rivalenti et al., 2007) have correlated optical observations of the microstructures with chemical compositions and equilibrium temperatures to divide the Macau peridotite xenoliths into two groups: protogranular and porphyroclastic. In the present study, we associated to the optical observations quantitative analysis of the microstructural data derived from EBSD mapping. Based on these data, in particular the intragranular misorientation of olivine and the olivine and orthopyroxene grain shapes (Fig. 2), we classify the Macau peridotites into three microstructural groups (Table 1): coarse-granular (6), coarse-porphyroclastic (12), and fine-porphyroclastic (4). The coarse-granular and coarse-porphyroclastic groups correspond to a continuous variation in microstructure (Figs. 2 and 3). They were described as protogranular in the previous studies. The fine-porphyroclastic group is clearly different from the other two groups (Figs. 2 and 3); it was described as porphyroclastic in the previous studies.

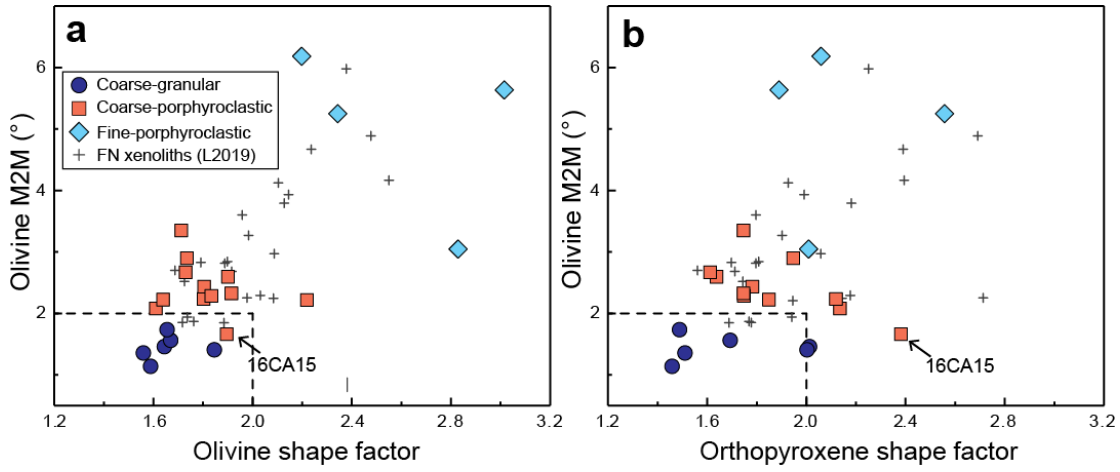

Fig. 2. Microstructural parameters calculated from EBSD data: (a) Olivine shape factor vs. intragranular misorientation relative to the mean orientation of the grain (M2M); (b) Orthopyroxene shape factor vs. olivine M2M. All quantities are average values at the sample scale weighted by the grains' area (cf. Table 2). Similar data for Fernando de Noronha (FN) xenoliths, which sample an old domain of the equatorial Atlantic (Liu et al., 2019), are presented for comparison.

There is no relation between microstructure and sampling site. All three microstructures are represented among the Pico do Cabugi peridotites, which is the best-sampled site in the present study, and in at least one of the other sampling localities (Table 1). This observation is corroborated by the previous studies, which analyzed a larger number of peridotite xenoliths from other Macau volcanic centers (Fodor et al. 2002; Rivalenti et al. 2007). Coarse

granular and coarse porphyroclastic microstructures predominate in all sites. Fine-porphyroclastic peridotites are always minor. They were only recovered in three sites, which are nevertheless >60 km apart (Fig. 1): Serra Aguda, Cabugi, and Serrote Preto (a small plug ca. 30 km to the SSE of Pico do Cabugi, Fodor et al. 2002).

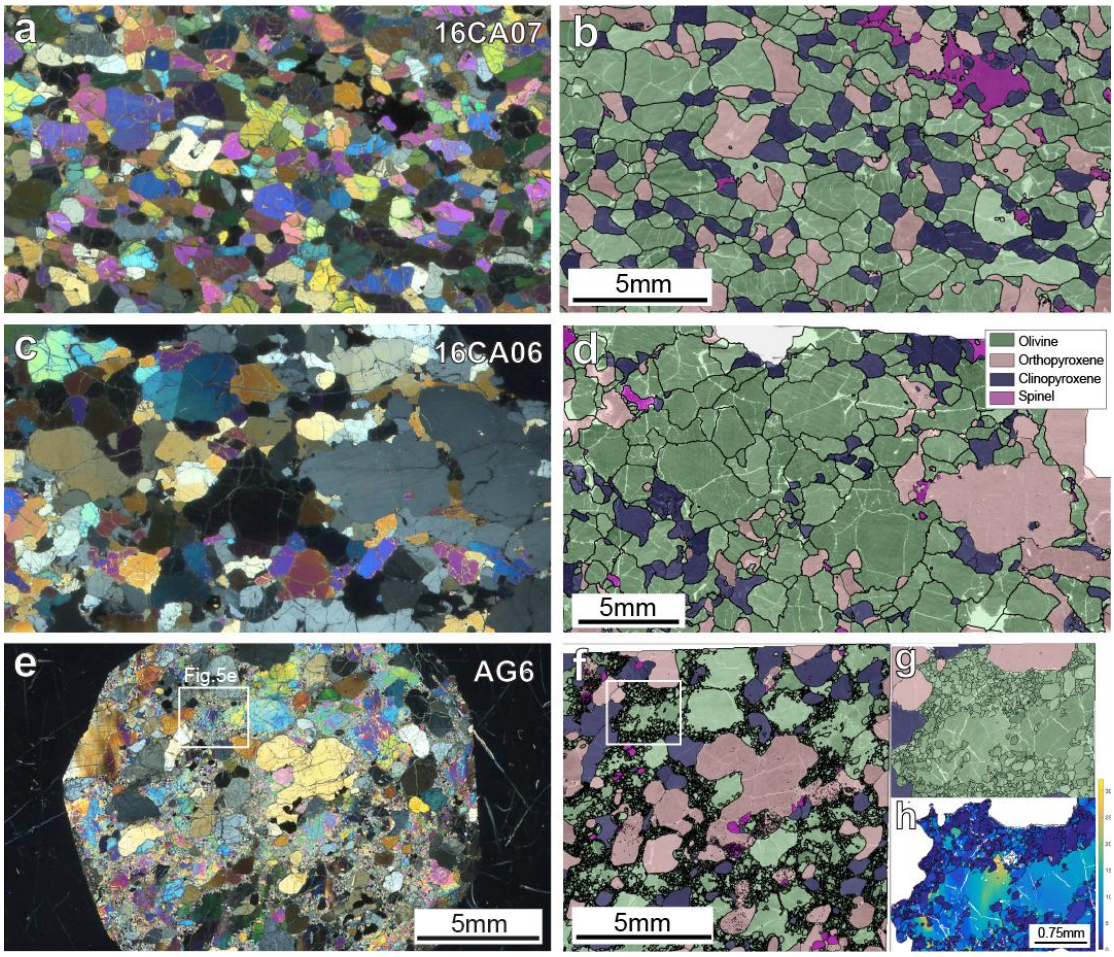

Fig. 3. Typical microstructures of Macau peridotite xenoliths: (a-b) coarse-granular, (c-d) coarse-porphyroclastic, and (e-f) fine-porphyroclastic. (a,c,e) Photomicrographs in cross-polarized light; scale bar is the same in all photomicrographs. (b,d,f,g) EBSD phase maps, which better illustrate the variation in shape of olivine and pyroxenes between the three microstructures. (g) Detail of a partially recrystallized domain in fine-porphyroclastic lherzolite AG6. (h) Misorientation relative to the mean orientation of the grain (M2M) map illustrating the difference in intragranular misorientation in olivine between porphyroclasts (high M2M) and neoblasts (low M2M) in the same domain.

Coarse-granular peridotites are characterized by roughly equigranular microstructures (Fig. 3a-b). Olivine and orthopyroxene pyroxene grains are on average 1-3 mm, clinopyroxene slightly smaller: 0.8-1 mm (Table 2). Both olivine and pyroxenes have curvilinear to straight grain boundaries, evolving locally into polygonal shapes with 120° triple junctions (Fig. 4a), and very low densities of intracrystalline deformation features, such as undulose extinction, subgrains, or kinks (Fig. 3a and 4a). Quantitatively, these observations

translate into low shape factors ≤ 1.85 for olivine and ≤ 2 for orthopyroxene and into low M2M values ≤ 2° for olivine (Fig. 2). Lherzolite 16CA14 has an intermediate microstructure characterized by polygonal olivine grains, but pyroxenes with irregular shapes (Figs. 2 and 4b). Most coarse-granular peridotites display a weak olivine shape-preferred orientation (SPO) (Fig. 3a), but BO09 has higher olivine aspect ratios (Table 2) and a clear olivine SPO, which results in a tabular microstructure. Pyroxene grains usually show no exsolutions (Fig. 3a and 4a-b). Spinel grains have holy-leaf or interstitial shapes. Coarse holy-leaf spinels may contain rounded inclusions of olivine or pyroxenes (Fig. 3b).

Coarse-porphyroclastic microstructures are characterized by variable grain sizes. In most cases, the grain size variation is continuous and it is difficult to discriminate between porphyroclasts and neoblasts (Fig. 3c-d). Olivine has more irregular grain shapes and clear evidence for intracrystalline plastic deformation (Fig. 3c-d and 4c). Olivine grains have shape factors between 1.6 and 2.2, consistently with the more sinuous grain boundaries, and higher M2M values ranging from 2° to 3.4° (except 16CA15), consistent with the higher frequency of undulose extinction and subgrain boundaries (Fig. 2). Orthopyroxene grains also have irregular shapes (Fig. 3c-d and 4c-d), which are associated with shape factors from 1.6 to 2.4 (Fig. 2b). Orthopyroxene grain boundaries often show embayments or cuspate shapes at the contact with olivine grains (Fig. 4c-d). Clinopyroxene grains also show irregular or interstitial shapes (Fig. 3c-d). In some samples, orthopyroxene grains display exsolutions (Fig. 3c). Undulose extinction and kinks are observed locally. Spinel usually has irregular shapes and occurs in association with ortho- or clinopyroxene (Fig. 3d).

Fine-porphyroclastic peridotites show a well-developed bimodal olivine grain size distribution, characterized by coexistence of coarse porphyroclasts with serrated grain boundaries, undulose extinction, and closely-spaced subgrain boundaries with a recrystallized matrix composed by polygonal olivine neoblasts free of intracrystalline deformation (Figs. 3e-h and 4e-f). The average size of the recrystallized grains varies between samples (Table 2): it is ~100 µm in AG6 (Fig. 4e), but >300 µm in the other fine-porphyroclastic peridotites (Fig. 4f, Table 2). It is noteworthy that the recrystallized olivine grains are not organized in a planar mode, marking a foliation, but either form irregular pockets or vein-like structures (Fig. 3e-f). Orthopyroxene is usually coarser than clinopyroxene (Fig. 3f). Exsolutions were not observed in this group. Shape factors of orthopyroxene vary between 1.89 and 2.56 (Fig. 2). In AG6 and AG7, pyroxenes have rounded shapes (Fig. 3f), whereas in PC105 and PC109 fine-porphyroclastic samples, pyroxenes have irregular shapes, with cusp-like terminations when in contact with olivine, similarly to pyroxenes in coarse-porphyroclastic peridotites. Spinel occurs as fine rounded grains (Fig. 3f).

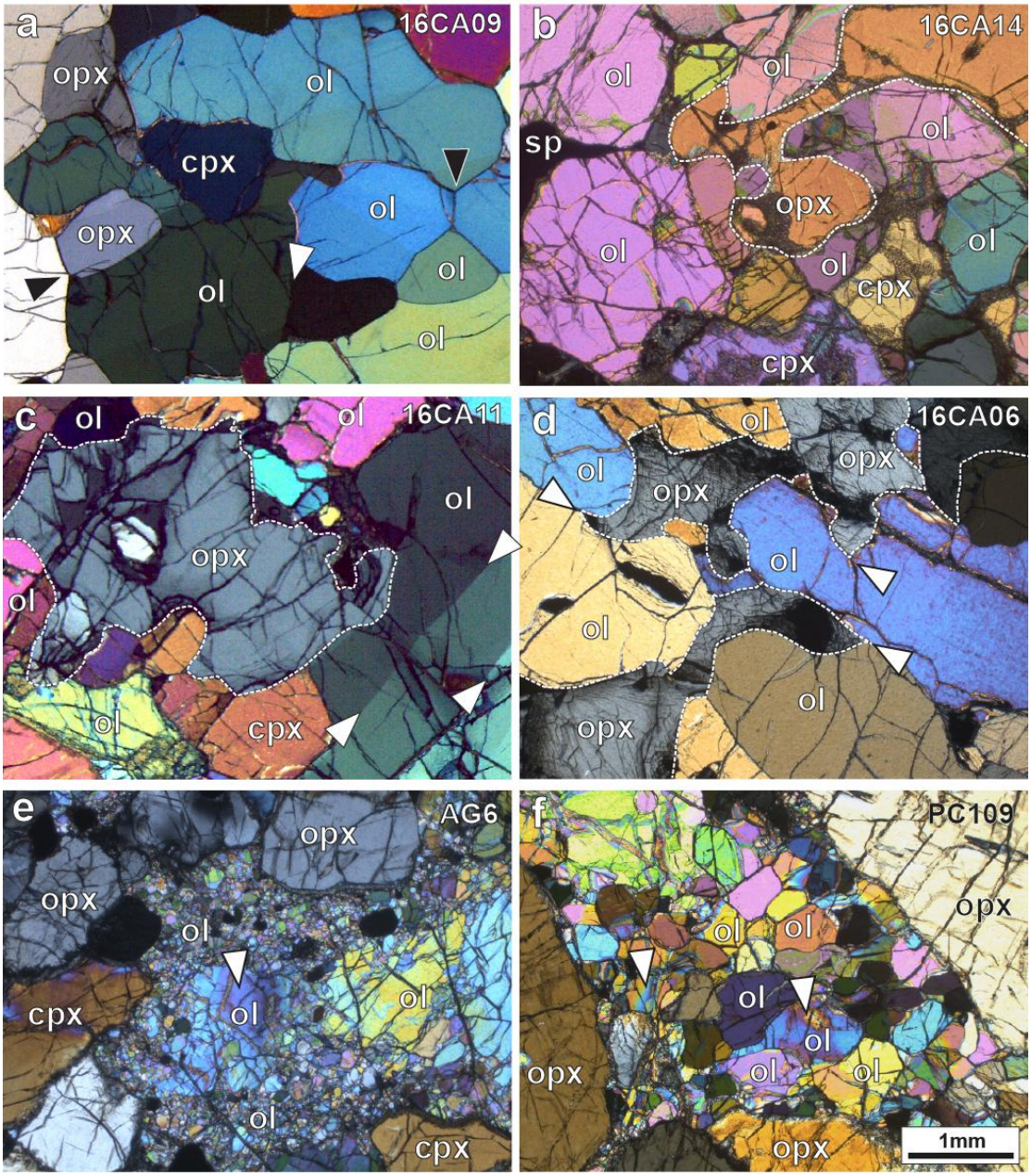

Fig. 4. Photomicrographs in cross-polarized light displaying typical features for the three microstructural groups. (a) Coarse granular lherzolite displaying polygonal grains (black arrow marks a 120° triple junction) almost free of intracrystalline deformation features, white arrow indicates a relict subgrain boundary in olivine (ol); (b) Coarse granular lherzolite 16CA14 displaying polygonal strain-free olivine grains, but irregularly-shaped orthopyroxene (opx) grains (highlighted by dashed line). (c-d) Coarse porphyroclastic lherzolites 16CA11 and 16CA06 showing irregularly shaped olivine, orthopyroxene (highlighted by dashed line), and clinopyroxene (cpx) grains with interpenetrating interphase boundaries, white arrows indicate subgrain boundaries in ol in (c) and mark cusp shaped opx in contact with ol in (d); (e) Fine-porphyroclastic lherzolite AG6 showing a matrix of very fine recrystallized olivine neoblasts surrounding a coarse olivine porphyroclast with ondulose extinction and subgrains (white arrow); (f) Fine-porphyroclastic harzburgite PC109 showing tabular, strain-free olivine neoblasts as well as relicts of olivine porphyroclasts with undulose extinction (white arrow) within a strongly recrystallized domain between opx porphyroclasts. Scale bar is the same in all photomicrographs.

4.2 Crystallographic preferred orientations (CPO)

Quantitative data on the intensity and symmetry of the olivine CPO (J- and BA-indexes) as well as pole figures of the olivine, orthopyroxene, and clinopyroxene CPOs for all studied samples are presented in Figs. 5 and 6 and Table 2. For the samples in which a foliation was observed, the latter is displayed on the pole figures (Fig. 6). In these samples, the olivine [010] maximum is normal to the foliation.

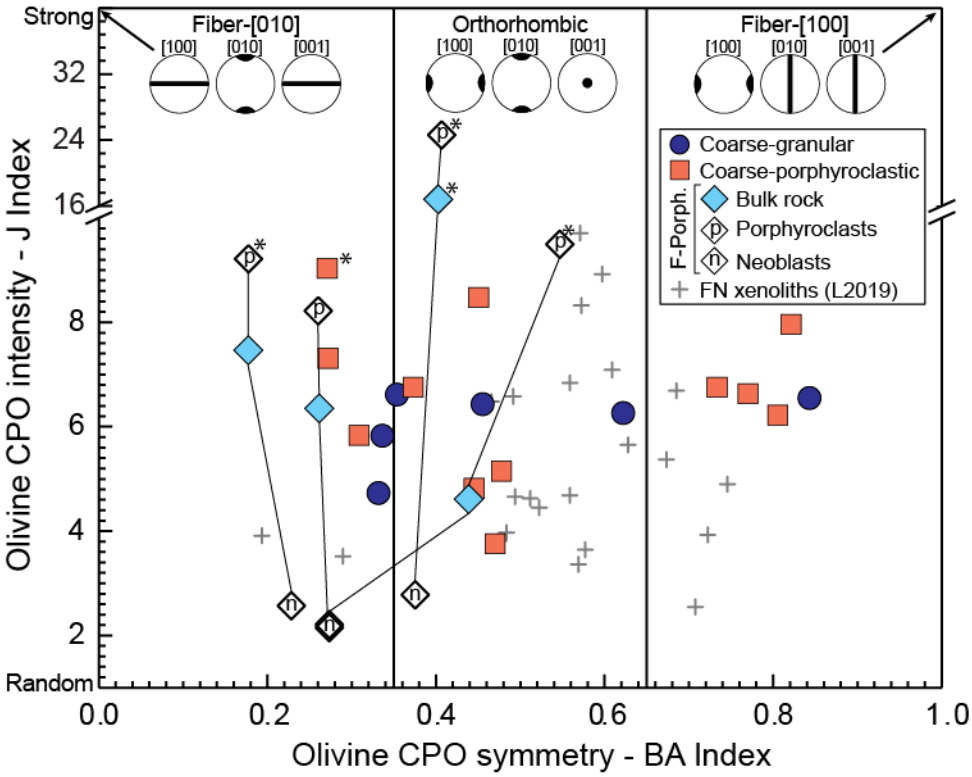

Fig. 5. Olivine CPO symmetry (BA-index) vs. CPO strength (J-index). The variation in olivine CPO pattern as a function of BA-index is illustrated at the top of the diagram. For fine-porphyroclastic peridotites, we present data for the bulk rock and for porphyroclasts and neoblasts separately. Values are presented in Table 2. * indicates J-indexes that are probably overestimated, because <100 grains could be analyzed in the thin section. CPO data for Fernando de Noronha (FN) xenoliths (Liu et al., 2019) are displayed for comparison.

Olivine has moderate to strong CPO (Figs. 5 and 6). With exception of harzburgite AG7, which has a very high J-index of 16.6 due to a few coarse olivine porphyroclasts that occupy most of the thin section, the J-index varies between 3.8 and 8.5, with a mean of 6.4. The CPO symmetry varies between fiber-[010], orthorhombic, and fiber-[100] patterns. Fine-porphyroclastic peridotites display olivine CPO patterns intermediate between fiber-[010] and orthorhombic and the neoblasts have systematically weaker olivine CPO (Figs. 5 and 6a). There is no systematic variation of J-index or BA-index within the two other microstructural groups. Coarse-granular samples display dominantly orthorhombic olivine CPO patterns with J-indexes around 6 (Figs. 5 and 6a). Coarse-porphyroclastic samples have more variable CPO patterns and

intensities (Fig. 5). Four coarse-porphyroclastic harzburgites (16CA01, 16CA02, 16CA03, and 16CA18) have strong CPO with fiber-[100] patterns (Fig. 6b). The remainder coarse-porphyroclastic peridotites display variable CPO intensity orthorhombic patterns with a tendency towards fiber-[010], expressed as girdle of [100] with a maximum within it and a point maximum of [010] (Fig. 6b).

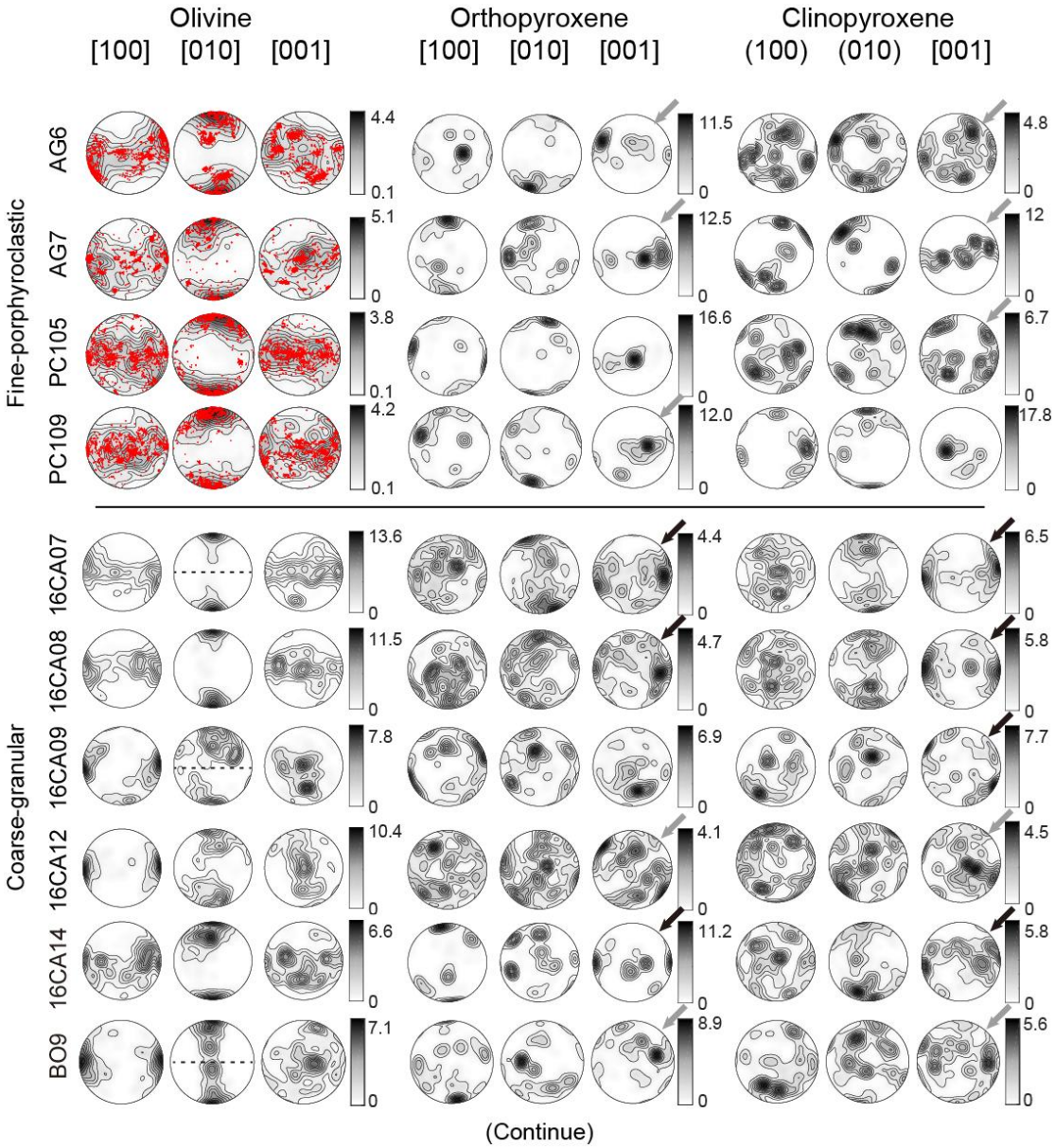

Fig. 6. Crystal preferred orientations (CPO) of olivine, orthopyroxene, and clinopyroxene for all studied fine-porphyroclastic and coarse-granular peridotites and coarse-porphyroclastic peridotites. Lower hemisphere stereographic projections with contours at 1 multiple of a uniform distribution intervals. The three pole figures for each mineral are plotted using the same gray scale. For the fine-porphyroclastic peridotites, the CPO of olivine porphyroclasts is presented as points and the CPO of olivine neoblasts is presented as contours. Black arrows indicate pyroxene CPO that are well correlated with the olivine CPO and gray arrows indicate those partially correlated. When the sample shows a olivine shape preferred orientation marking a foliation, the latter is displayed as a dashed

line in the olivine [010] pole figure.

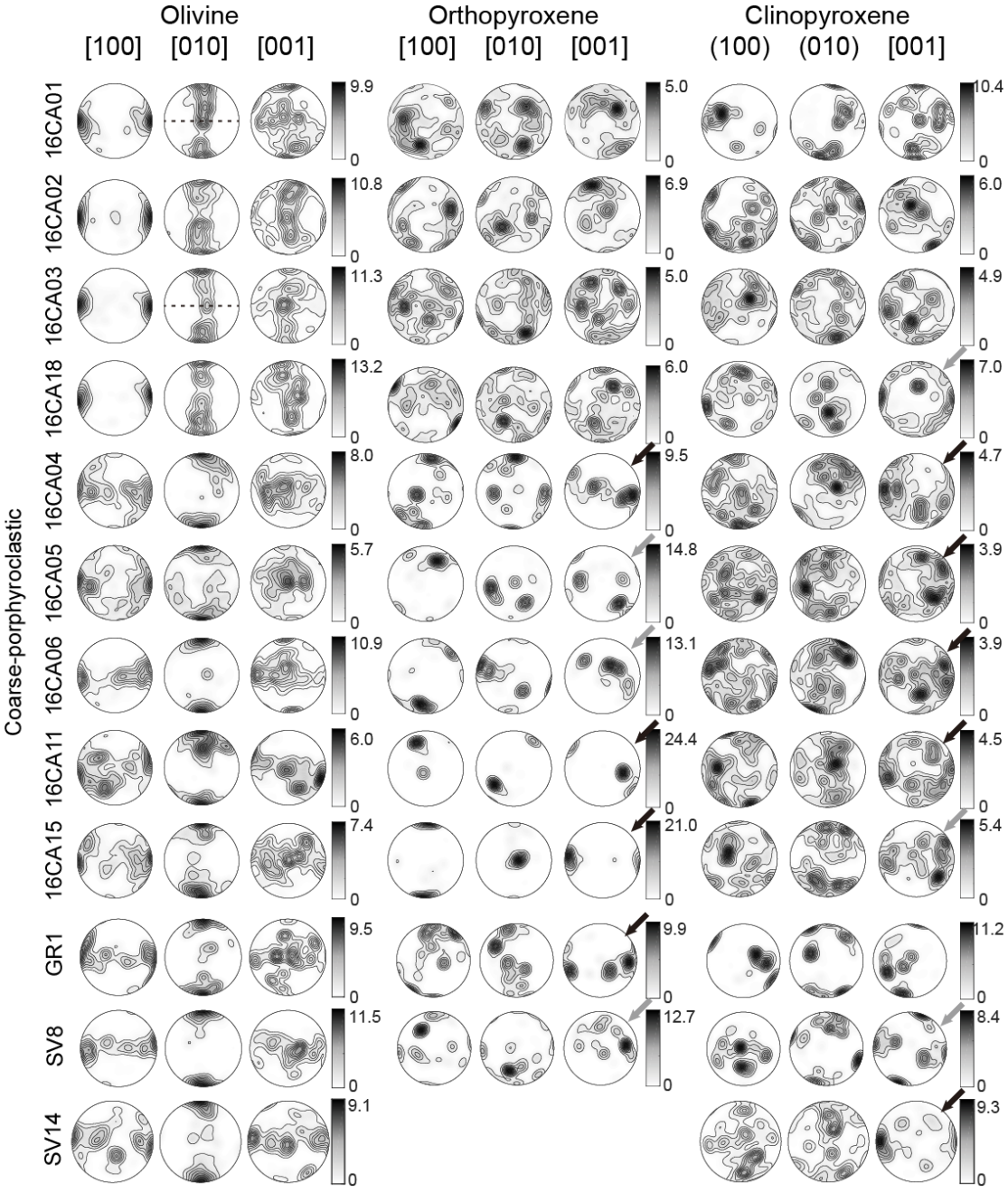

Orthopyroxene CPO is consistent with the olivine CPO in the majority of the studied peridotites. It is characterized by $[001]_{opx}$ and $[100]_{opx}$ (or $[010]_{opx}$) maxima parallel to the $[100]_{ol}$ and $[010]_{ol}$ maxima, respectively, suggesting a common deformation history (arrows in Fig. 6). However, coarse-porphyroclastic harzburgites 16CA01, 16CA02, 16CA03, 16CA18 and coarse-granular lherzolite 16CA09 show weak orthopyroxene CPO that are not consistent with the olivine CPO, characterized by a weak $[001]_{opx}$ maximum at high angle to a well-developed $[100]_{ol}$ maximum.

Clinopyroxene shows more dispersed CPO, but which are, in many samples, consistent with both olivine and orthopyroxene CPO patterns,

characterized by $[001]_{cpx}$ and $[010]_{cpx}$ maxima subparallel to $[100]_{ol}$ and $[010]_{ol}$ maxima (arrows in Fig. 6). However, in most fine-porphyroclastic peridotites and in coarse-granular lherzolite 16CA12, although the orthopyroxene CPO is consistent with the olivine CPO, the clinopyroxene CPO is not. In coarse-porphyroclastic harzburgites (16CA01, 16CA02, 16CA03, 16CA18) neither the orthopyroxene nor the clinopyroxene CPO are correlated with the olivine CPO.

4.3 Modal compositions

Modal compositions were determined based on the area fraction of each mineral in the EBSD maps (Fig. 7 and Table 1). All samples are spinel-facies peridotites. Lherzolites predominate (14/22), but the sampling also includes 7 harzburgites and 1 wehrlite. Predominance of fertile peridotites with no dependence on sampling site was also observed in previous sampling of Macau xenoliths by Rivalenti et al. (2000, 2007; Fig. 7).

The compositions of the two microstructural groups overlap, but coarse-granular peridotites are on average more fertile (ol contents of 57-70%) than coarse-porphyroclastic peridotites (ol contents between 67-87%, with one outlier – 16CA04, which has 59% of olivine and an intermediate microstructure). Fine-porphyroclastic peridotites display variable olivine contents overlapping with the two other groups.

Comparison of the modal compositions to those predicted by various partial melting models highlights that roughly half of the studied Macau xenoliths are enriched in clinopyroxene or olivine relatively to the models' predictions (Fig. 7). Even for those samples plotting along the partial melting trends, a large variability in partial melting degrees, from 1-20% melting, has to be invoked to explain the full range of observed modal compositions. Such a variation in partial melting is difficult to reconcile within the limited volume of the mantle sampled by these volcanic eruptions. This suggests reactive melt percolation leading to either crystallization of clinopyroxene and/or orthopyroxene at the expenses of olivine (refertilization processes, e.g. Le Roux et al., 2007; represented by gray arrows in Fig. 7) or crystallization of olivine at the expense of pyroxenes (dunitization processes, e.g., Berger and Vannier, 1984; Kelemen, 1990; black arrows in Fig. 7). The observed deviations in modal compositions relatively to partial melting trends are consistent with microstructural evidence for reactive melt percolation, such as the sinuous olivine-pyroxene boundaries and the cusp-like shapes of pyroxenes when in contact with two olivine grains (cf. Figs. 3 and 4).

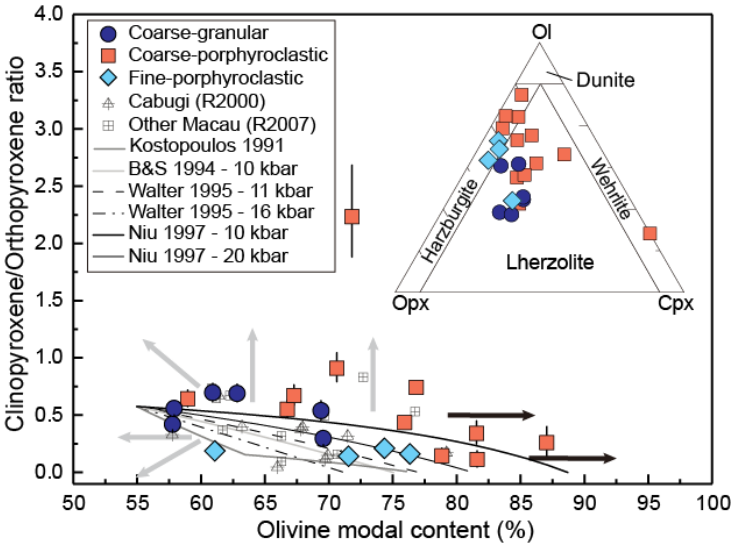

Fig. 7. Modal compositions of the studied peridotites presented as clinopyroxene/orthopyroxene ratio vs. olivine modal content and as the traditional ol-opx-cpx ternary diagram (insert). Modal compositions of Cabugi and other Macau volcanics peridotite xenoliths studied by Rivalenti et al. (2000) and (2007) are plotted for comparison. Black and gray curves represent the evolution of the modal composition predicted by different partial melting models for an initial fertile modal composition of 55% ol, 28.5% opx, and 16.5% cpx (Baker and Stolper, 1994; Kostopoulos, 1991; Niu, 1997; Walter et al., 1995). Gray arrows indicate evolution trends associated with cpx and/or opx crystallization at the expense of ol (refertilization reactions). Black arrow indicates evolution trends associated with ol crystallization at the expense of pyroxenes (dunitization reactions).

4.4. Mineral compositions

The chemical compositions of main mineral phases in the studied Macau peridotite xenoliths are listed in Supplementary Material Table S1. Representative results are displayed in Fig. 8 together with previous data for Macau peridotite xenoliths (Supplementary Material Table S2). Comparison between the present and previous datasets indicates that our sampling is representative of the variability in composition for these localities. Analysis of the present dataset indicates that there is no simple correlation between microstructural types and chemical compositions (Fig. 8). There is also no relation between mineral chemistry and sampling locality.

The Mg# number [Mg# = 100×Mg/(Fe + Mg), atomic ratio] of olivine, orthopyroxene, and clinopyroxene ranges between 89.1 – 91.6 (average 90.0), 89.1 - 91.7 (average 90.4), and 87.9 – 92 (average 90.9), respectively (Figs. 8a,b). Core-rim variations in Mg# are weak for all three minerals in most samples. Olivine and orthopyroxene Mg# within each sample show low dispersion and are positively correlated, with the orthopyroxene being slightly enriched in Mg relatively to olivine (all data points, except fine-porphyroclastic peridotites AG6 and AG7, plot slightly above the 1:1 line in Fig. 8b). Clinopyroxene Mg# shows much higher variability at the sample scale, in particular within coarse-porphyroclastic harzburgites, indicating chemical disequilibrium at the mm-scale. Moreover, average clinopyroxene Mg# in

neither cores nor rims does not display a simple correlation with the olivine Mg# (Fig. 8a). Most measured Mg# spread between the 1:1 and the Fe-Mg partition trend between olivine, clinopyroxene, and melt in oceanic troctolites (Lissenberg and Dick 2008), but fine-porphyroclastic peridotites AG6 and AG7 have clinopyroxenes enriched in Fe relatively to olivine.

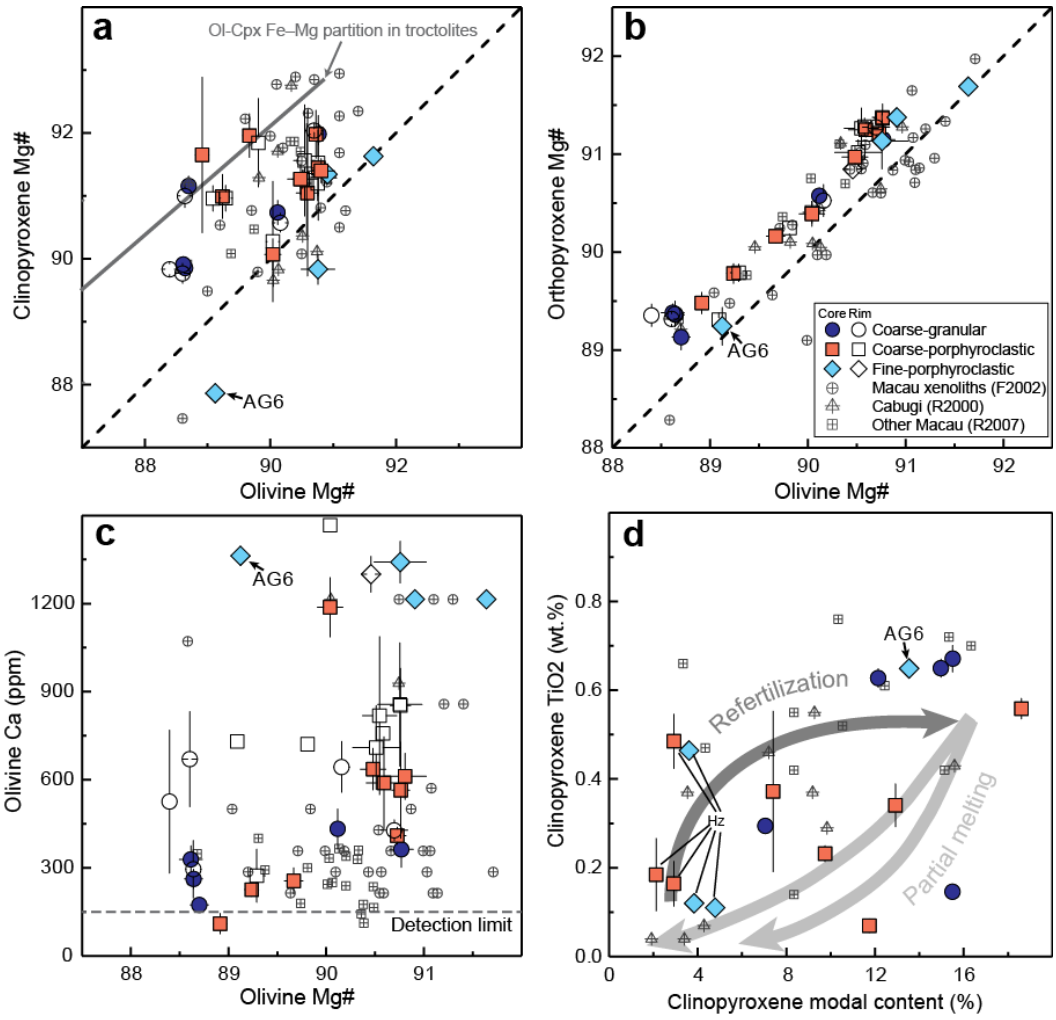

Fig. 8. Chemical compositions for major rock-forming minerals: (a-c) Clinopyroxene Mg#, orthopyroxene Mg#, and olivine Ca content (ppm) vs. olivine Mg#, (d) Clinopyroxene TiO2 content (wt.%) vs. modal content (%). Minerals chemical compositions for Macau peridotite xenoliths previously studied by Rivalenti et al. (2000), (2007), and Fodor et al. (2002) are plotted for comparison. The value of the depleted mantle (DM) from Workman and Hart (2005) is displayed in (a) and (b). Fe-Mg partition between olivine and clinopyroxenes in troctolites (Lissenberg and Dick, 2008) is plotted in (a). Partial melting and refertilization trends proposed by Le Roux et al. (2007) are plotted in (d). Hollow symbols represent rim compositions and solid symbols represent core ones. Error bars represent the chemical variation at the sample scale. Data is presented in Supplementary Material Table S1.

Olivine cores show low Ca contents with a weak positive correlation with Mg#, (Fig. 8c), except for the fine-porphyroclastic peridotites and the coarse-porphyroclastic lherzolite GR1, which have high Ca contents. Olivine rims in all studied peridotites are enriched in Ca and show a high variability at

687 the thin section (mm-cm) scale.
688 Clinopyroxene TiO_2 contents (wt.%) do not show the simple positive
689 correlation with cpx modal content (%) expected if partial melting controlled the
690 chemistry of the peridotites (Fig. 8d). Among the harzburgites, four have
691 Ti-poor clinopyroxene grains (TiO_2 contents < 0.2%), while the other two have
692 clinopyroxene grains with TiO_2 contents of 0.55%. All harzburgites show
693 marked variability in the Ti-content of clinopyroxene at the sample scale,
694 indicating disequilibrium. Half of the lherzolites have clinopyroxenes with
695 almost constant TiO_2 contents between 0.55-0.65%, independently of the
696 clinopyroxene modal content. The remaining lherzolites have rather Ti-poor
697 clinopyroxene grains.
698 Spinel Cr# [Cr# = 100×Cr/(Cr+Al) and Mg# contents correlate with the
699 modal composition. Harzburgites have spinel with Cr# ranging between
700 40-57.5 and Mg# ranging between 61-72, whereas lherzolites have spinel with
701 Cr# between 8-20 and Mg# between 73-84 (Supplementary Material Fig. S1a).
702 Yet, the lherzolites show a clear enrichment in Mg in spinel relatively to a
703 typical depleted mantle composition. Fine-porphyroclastic lherzolite AG6 has
704 the highest spinel Mg# (83) and lowest Cr# (11). TiO_2 contents (wt. %) in spinel
705 are low (≤0.18%) in most lherzolites (Supplementary Material Fig. S1b). In
706 contrast, spinel in coarse-porphyroclastic harzburgites and lherzolite GR1 has
707 a wide range of average TiO_2 contents, which may reach 1.03%, with strong
708 variations within each sample, indicating disequilibrium. Spinel in
709 fine-porphyroclastic lherzolite AG6 also has a fairly high TiO_2 content of 0.45%.
710
711 *4.5. Equilibrium temperatures and geotherm estimation*
712 Most equilibrium temperatures determined using two-pyroxenes
713 geothermometer of Taylor (1998; TTA98) and the Ca in orthopyroxene
714 (Ca-in-opx) of Brey and Kohler (1990) revised by Nimis and Grutter (2010)
715 agree within ±70 °C (gray dashed lines in Fig. 9). This suggests that they are
716 reliable. However, peridotites with cpx-opx temperatures < 800 °C show larger
717 discrepancies (>90 °C), with systematically higher Ca-in-opx equilibrium
718 temperatures. This inconsistency between the predictions of the two
719 thermometers is observed for both core and rim temperatures and is not
720 correlated with the microstructure. It affects two coarse-porphyroclastic
721 peridotites (16CA06, 16CA11) and one coarse-granular lherzolite (16CA14).
722 The latter has the lowest temperature among all samples with strong
723 inconsistency between the predictions of the two thermometers (592°C and
724 790°C, Table 1).
725 Following Nimis and Grutter (2010), we use the temperature predictions
726 of TTA98 thermometer as the equilibrium temperatures. All
727 fine-porphyroclastic peridotites and the coarse-porphyroclastic peridotite GR1
728 have high equilibrium temperatures over 1200 °C. Coarse-porphyroclastic
729 peridotites have two ranges of equilibrium temperatures: harzburgites
730 (16CA01, 16CA03, 16CA18) as well as clinopyroxene-poor lherzolite SV8

have equilibrium temperatures between 900 and 1100 °C, whereas the clinopyroxene-rich coarse-porphyroclastic lherzolites (16CA06, 16CA11, 16CA15) have lower equilibrium temperatures between 600 and 700 °C. Coarse-porphyroclastic peridotites 16CA03, 16CA15, and 16CA18 display core-rim variations in equilibrium temperature. In most cases, rim Ca-in-opx temperatures are higher than core ones, but there is no systematic trend. All samples that display core-rim variations also show significant dispersion in both core and rim temperatures at the sample scale (bars in Fig. 10). Coarse-granular peridotites 16CA07, 16CA08, 16CA09, and BO9 have intermediate equilibrium temperatures between 800 and 900 °C and less variations at sample scale as well as between cores and rims. Comparison with previous thermometry data on Macau peridotite xenoliths indicates that the present sampling is representative of the variability in this suite (Fig.9). Analysis of the full dataset also highlights that there is no relation between equilibrium temperatures and sampling site. The full range of equilibrium temperatures is observed both among Pico do Cabugi xenoliths, which is the best sampled site, and among xenoliths from other Macau volcanics.

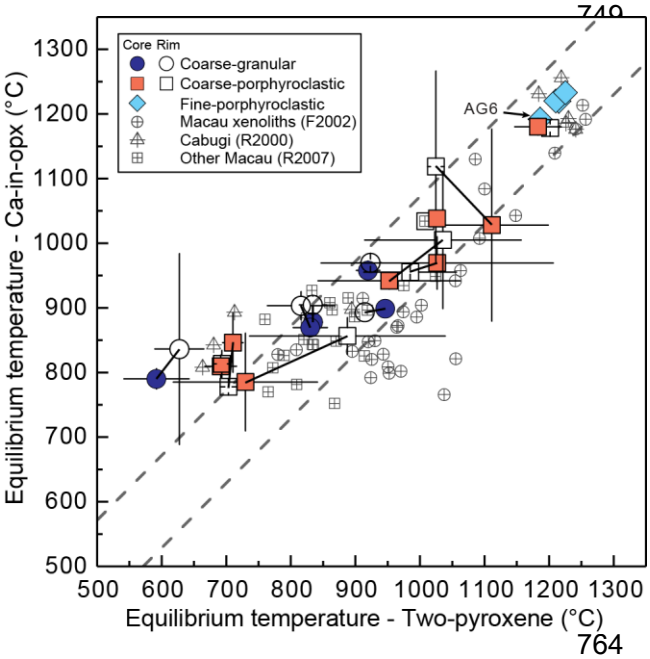

Fig. 9. Average core and rim equilibrium temperatures calculated using the cpx-opx thermometer (TTA98, Taylor, 1998) and the Ca-in-opx thermometer (Ca-in-opx, Brey and Kohler, 1990, revised by Nimis and Grutter, 2010). Chemical compositions from Rivalenti et al. (2000) and (2007) and Fodor et al. (2002) were used to recalculate the equilibrium temperatures for their samples using the same thermometers (data is presented in Supplementary Material Tables S2 and S3). Error bars represent data spread within each sample. Gray dashed lines outline a ±70°C variation between the two thermometers.

To estimate the Cenozoic geotherm in the northern Borborema Province, we plotted the TTA98 equilibrium temperatures of the studied xenoliths against the peridotite phase diagram in the upper mantle (spinel-out, plagioclase-out, and garnet-in curves for different Cr contents from O'Neill, 1981 and Klemme, 2004), as well as equilibrium geotherms for different surface and reduced heat flows (Fig. 11). The geotherms are calculated assuming a surface heat flow of 60 or 70 mW/m^2 (Hamza et al., 2018), a Moho depth of 32 km (Almeida et al., 2015), an exponential decrease of the radiogenic heat production with depth, with a characteristic depth of 10 km, and a reduced heat flow of either 30 or 45 mW/m^2. For comparison, we also indicate the depth of the

lithosphere-asthenosphere boundary determined by P-S receiver functions for seismic station RCBR (Heit et al., 2007) and the partial melting conditions estimated based on the compositions of the most primitive melts of the Cenozoic Macau and Mesozoic Ceará-Mirim suites (Ngonge et al, 2015a,b).

P-T equilibrium conditions of the peridotites are displayed as a fixed temperature corresponding to the TTA98 thermometry prediction, but as a pressure range, because there are no reliable barometers for spinel-facies peridotites. The range of equilibrium pressure conditions is defined by the occurrence of spinel in absence of plagioclase or garnet for the actual Cr content of each peridotite (O'Neill, 1981; Klemme, 2004).

The wide range of equilibrium temperatures suggests that the studied peridotites represent a complete sampling of the subcontinental lithospheric mantle. The absence of garnet in the entire suite, which is largely composed of peridotites with Cr# < 15, constrains a maximum equilibrium depth of the studied peridotites shallower than 75 km (Fig. 10). By consequence, the equilibrium conditions of the Macau peridotite xenoliths, except 16CA14 that has the lowest and likely unreliable equilibrium temperature, are better fitted by the hotter geotherm (green line in Figure 10).

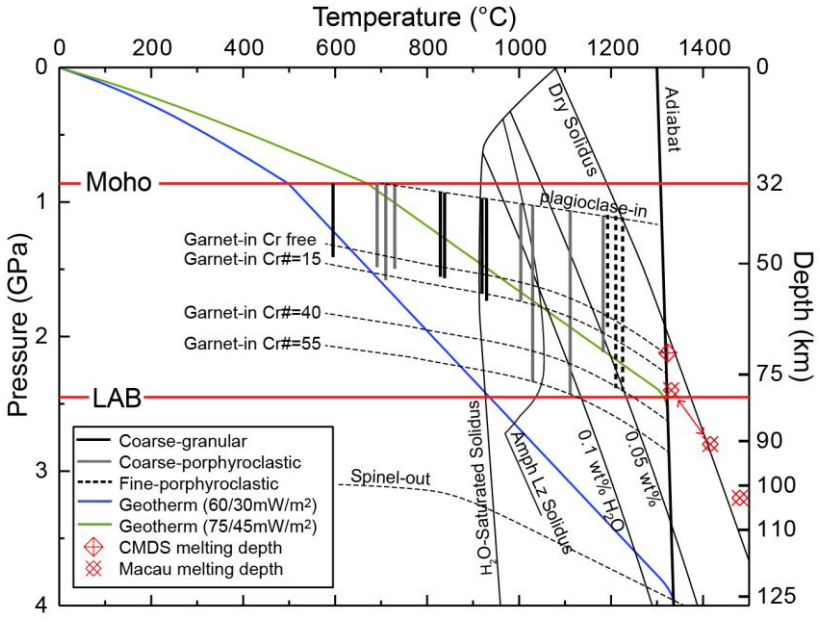

Fig. 10. P-T diagram comparing the equilibration conditions estimated for the studied Macau xenoliths to two possible steady-state geotherms for the north Borborema province (surface / reduced heat flows indicated in parenthesis). Xenolith data is better fitted by the hotter geotherm (surface and reduced heat flows of 75 and 45mW/m^2, respectively). Since no barometers are available for spinel peridotites, equilibrium pressure ranges are presented as bars, based on the absence of plagioclase and of garnet in the studied peridotites, considering their Cr# (Supplementary Information Table S1) and the effect of Cr on the spinel-garnet phase transition (Klemme, 2004; O'Neill, 1981). Dry and wet solidus with variable H_2O contents after Ringwood (1975). Moho and Lithosphere-Asthenosphere Boundary (LAB) depths derived from S-P and P-S receiver function analyses (Almeida et al., 2015, Heit et al., 2007) as well as partial melting conditions derived from the primitive melt compositions of the Cretaceous Ceará-Mirim dyke system (CMDS) and Cenozoic Macau volcanics (Ngonge et al., 2016a,b) are displayed for comparison.

4.6. Seismic properties

For calculating seismic properties, we divided the xenoliths into two groups as a function of their TTA98 equilibrium temperature: low (T < 1000 °C) and high-temperature (T > 1000 °C). Then, we estimated the elastic tensors of the individual samples (Supplementary Material Table S3) for the pressure and temperature conditions predicted at 50 km (1.46 GPa and 916 °C) and 70 km depth (2.12 GPa and 1189°C) for the geotherm that best fits the xenolith data (Qs=70 mW/m^2 and Qm=45 mW/m^2, green line in Figure 10).

Seismic anisotropy patterns of the individual samples vary slightly as a function of the olivine CPO symmetry. As usual, the seismic anisotropy intensity correlates positively with both the olivine CPO strength and olivine modal content (Figure 11). On average, the peridotites equilibrated at temperatures <1000°C tend to display lower anisotropy, due to both more dispersed olivine CPO and lower olivine contents. However, seismic anisotropy intensity does not increase linearly with increasing J-index. By consequence, overestimation of the olivine CPO intensity for fine-porphyroclastic harzburgite AG7 does not result in similar overestimation of its seismic anisotropy. The maximum S-wave polarization anisotropy varies from 5.5 to 7.3% in the low-temperature peridotites and from 5.9 to 10% in the hign-temperature ones (Fig. 11 and Table 3). Similarly, the maximum P-wave propagation anisotropy varies from 7.4 to 10% and from 7.7 to 14.2% (Table 3). The maximum fast (S1) wave propagation anisotropy varies from 3.0 to 5.9% in low-temperature samples and from 4.1 to 7.2% in high-temperature ones, whereas the maximum slow (S2) wave propagation anisotropy varies from 3.4 to 5.2% and from 1.9 to 7.3%, respectively (Table 3).

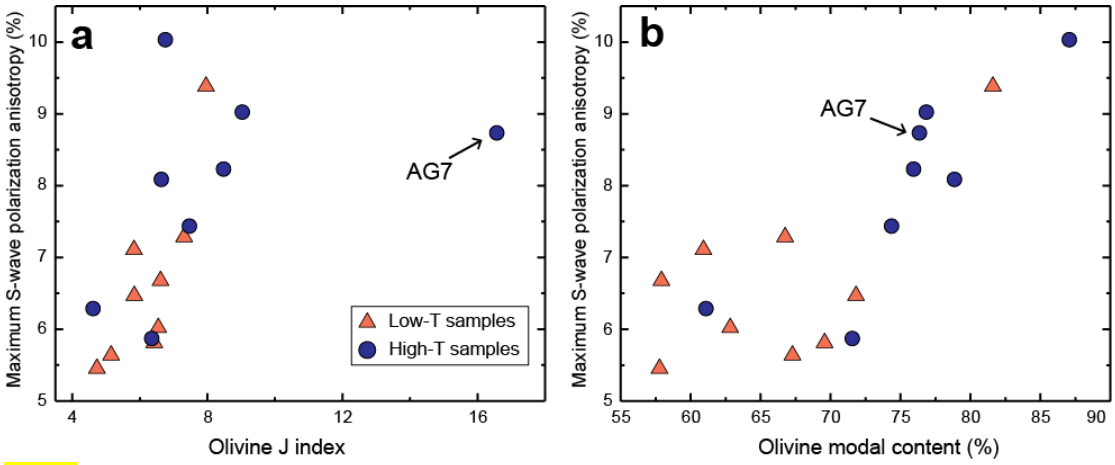

Fig. 11. Maximum S-wave polarization anisotropy (%) vs. (a) olivine CPO intensity (J index) and (b) olivine modal content (%) for all studied xenoliths. Seismic anisotropy data for individual samples are listed in Table 3.

Since seismic waves average elastic properties over large volumes, we calculated average elastic tensors for the low-temperature and high-temperature groups by assuming a coherent orientation of the past flow directions and planes (assumed as parallel to the [100] and [010] maxima of the olivine CPO, respectively – this assumption is justified by the analysis of

the CPO as discussed in the next section) over the entire lithosphere using a constant structural reference frame. These average seismic anisotropy patterns (Fig. 12) represent the maximum possible seismic anisotropy in the shallow (low-temperature group) and deep (high-temperature samples) sections of the lithospheric mantle, if the present sampling is representative of the volumes of the different microstructures and compositions in the lithospheric mantle in this region.

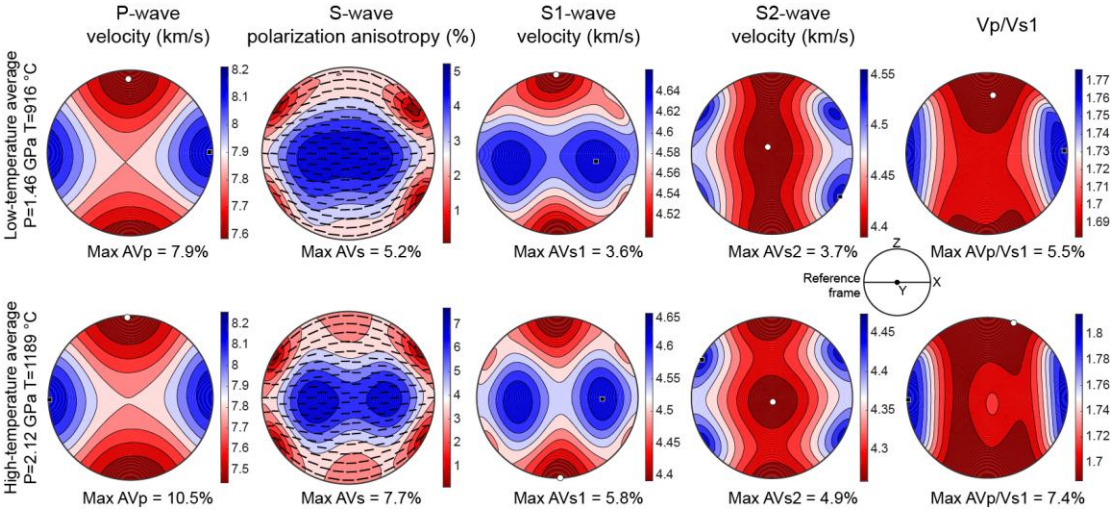

Fig. 12. Average seismic properties for shallow and deep sections of the lithospheric mantle beneath the study area calculated by averaging the elastic constant tensors of the eight low-temperature samples calculated for 916°C, 1.46GPa and of the nine high-temperature samples calculated for 1189°C, 2.12GPa. Lower hemisphere stereographic projections presenting the variation of the property as a function of the propagation direction relatively to the structural reference frame (flow direction (X) and normal to the flow plane (Z) shown by the insert). Black squares mark the highest values and white circles mark the lowest ones. Seismic properties data are listed in Table 3 and the elastic tensors, in Supplementary Material Table S4.

Seismic anisotropy patterns for the shallow and deep lithospheric mantle are similar, but as already discussed, the lower part of the lithosphere is more anisotropic (Fig. 12). The average maximum P-wave propagation anisotropy is 10.5% with velocities ranging between 7.4 and 8.3 km/s, compared to 7.9% in the shallow lithospheric mantle, where P-wave velocities vary between 7.6 km/s normal to the flow plane and 8.2 km/s parallel to the flow direction frozen in the lithospheric mantle (Table 3). The average maximum S-wave polarization anisotropy in the lower lithospheric mantle is 7.7% compared to 5.2% in the shallower levels; in both cases it is observed for S-waves propagating within the flow plane but at <45° of the flow direction. Low S-wave polarization anisotropy is observed for all waves propagating at low angle to the XZ plane, that is, the plane that contains both the flow direction and the normal to the flow plane. For all propagation directions in which a significant polarization anisotropy is observed, the fast S-wave is polarized in the plane containing the flow direction. The average maximum S1-wave propagation

anisotropy increases from 3.6% to 5.8% from the shallow to the deep mantle lithosphere. S1 velocity is maximum within the flow plane and minimum normal to it. S1-waves propagating within this plane show a 90° periodicity in the velocity variation. S2-waves average maximum propagation anisotropy increases from 3.7% to 4.9% with depth. High S2 velocities are associated with propagation within the XZ plane at ca. 45° to the flow direction (X) and low velocities are observed for all propagation directions at high angle to X. The maximum Vp/Vs1 ratio anisotropy increases from 5.5% to 7.4% with depth. Highest Vp/Vs1 ratios (1.78-1.8) are observed for waves propagating parallel to the flow direction and the lowest Vp/Vs1 ratios for waves propagating normal to the flow plane.

5. Discussion

5.1. Deformation, annealing, and reactive melt percolation

Coarse-granular peridotites show polygonal grain shapes for both olivine and pyroxenes and low intragranular misorientations (olivine M2M values < 2°, Fig. 2). However, they have well-developed olivine CPO (Figs. 5 and 6). This association supports that the deformation that produced the CPO was followed by annealing (static recrystallization), which effectively reduced dislocation densities and re-equilibrated grain shapes. The analysis of the relative intensity of the orientation of [100], [010], and [001] of olivine, of the relations between olivine and pyroxene CPOs, and of the relations between olivine CPO and SPO (when a SPO was observed) points to deformation by dislocation creep with dominant activation of the [100](010) slip system in olivine, [001](100) in orthopyroxene, and [001](0kl) in clinopyroxene (Tommasi et al. 2000, Bascou et al. 2002). Coarse-granular peridotites have roughly constant olivine CPO intensities, but variable symmetry, covering the entire range from fiber-[100] to fiber-[010]. Fiber-[100] and orthorhombic olivine CPO are the usual patterns produced by simple shear under dry, high to moderate temperatures, and low pressure in the upper mantle (Tommasi et al., 1999; 2000; Hansen et al. 2014). Fiber-[010] patterns, on the other hand, require particular conditions, which may be: transpression (Tommasi et al., 1999), presence of melts during the deformation (Higgie and Tommasi, 2012, 2014; Qi et al. 2018), changes in the olivine CPO by oriented growth during recrystallization (e.g., Tommasi et al., 2008), or deformation under high stress or high pressure conditions, which would lead to increased activation of [001] glide (Durham and Goetze, 1977; Mainprice et al., 2005; Demouchy et al. 2013). The mineralogy and microstructures and CPO of the coarse-grained peridotites falsify the last hypothesis. However, the present data does not allow for discriminating among the other hypotheses. The different olivine CPO symmetry may therefore result from variations in deformation regime, with fiber-[010] CPO recording transpression (which is the dominant deformation regime in the Seridó belt during the Brasiliano event), presence or not of melts

during the deformation (all deformation events were accompanied by magmatism), or different CPO evolution during recrystallization.

Analysis of the bulk rock Mg# vs. olivine modal content relation (Fig. 13) shows that the compositions of most coarse-granular peridotites deviate from partial melting trends, suggesting the occurrence of refertilization processes. Yet, most coarse-granular peridotites have coherent olivine and pyroxene CPOs (Fig. 6), which indicate co-deformation of the two phases. Thus, if melt-rock reactions leading to refertilization occurred, they predated or were concomitant to the deformation. Refertilization reactions produce sutured pyroxene-olivine boundaries and irregular shapes for both minerals. The equilibrated pyroxenes grain shapes in most coarse-granular peridotites indicate therefore that reactive melt percolation producing refertilization also predated annealing. It also implies that interphase grain boundary rearrangements during annealing were effective. These rearrangements depend on transport of ions along grain boundaries in a similar way to the growth of porphyroblasts in a metamorphic rock, but with weaker driving forces (grain boundary energy reduction opposed to chemical gradients). Most coarse-granular peridotites equilibrated around 900°C (Fig. 9). At this temperature, given the diffusivity of Si along olivine and enstatite grain boundaries ($\leq 10^{-27} m^3/s$; Fisler et al. 1997; Fei et al. 2016), grain boundary equilibration at the 250 µm scale, which is the average amplitude of the sinuosity of the olivine-pyroxene grain boundaries in the coarse-porphyroclastic peridotites (Fig. 3c,d), will occur on time scale of several hundreds of Ma. In contrast, irregular pyroxene grain shapes (high orthopyroxene shape factor ~2°, Fig. 2) in 16CA14 and BO9 point to a later stage of melt percolation. Indeed, in both samples, part of the pyroxenes shows crystal orientations not coherent with the olivine CPO (Fig. 6).

Coarse-porphyroclastic peridotites show less equilibrated microstructures. All major phases show sinuous grain boundaries (higher shape factors) as well as undulose extinction and subgrains, which translate into higher M2M values (Fig. 2). This implies a less effective annealing due to either a more recent deformation or lower post-deformation temperatures. The former hypothesis may apply for the coarse-porphyroclastic peridotites with high equilibrium temperatures (≥1000°C, Fig. 9) and the latter, for those with low equilibrium temperatures (<800°C, Fig. 9). Similarly to the coarse-granular peridotites, olivine CPO in coarse-porphyroclastic peridotites is consistent with deformation by dislocation creep with dominant activation of the [100](010) system. This interpretation is corroborated by the high frequency of (100) subgrain boundaries. However, the CPO patterns and intensities are more varied than those of coarse-granular peridotites (Figs. 5 and 6). Coarse-porphyroclastic harzburgites have strong fiber-[100] olivine CPOs, typical of simple shear deformation (Tommasi et al., 1999; 2000; Bystricky et al, 2000; Hansen et al., 2014). Lherzolites have orthorhombic to fiber-[010] olivine CPOs with variable strength. As for the coarse-granular peridotites, the

fiber-[010] olivine in these coarse-porphyroclastic peridotites may record either a component of transpression or the presence of melts during the deformation.

Although some coarse-porphyroclastic peridotites plot along partial melting trends in Fig. 13, evidence for reactive melt percolation leading to crystallization of pyroxenes or olivine is widespread. It encompasses: (i) the interpenetrating olivine-pyroxene grain boundaries and the locally interstitial shapes of pyroxenes (Figs. 3 and 4), which imply lack of microstructural equilibrium, (ii) the high variability of the olivine and pyroxenes chemical compositions both within grains and between grains in a sample (Fig. 8), which indicates absence of chemical equilibration, and (iii) lack or weak consistency between the olivine and the pyroxenes CPOs (Fig. 6). The latter feature is specific to the coarse-porphyroclastic harzburgites, which also show the highest equilibrium temperatures and least equilibrated mineral compositions among the coarse-porphyroclastic peridotites, implying that reactive melt percolation in these rocks, which sample the lower lithospheric mantle section in the province, postdates the deformation and is rather recent.

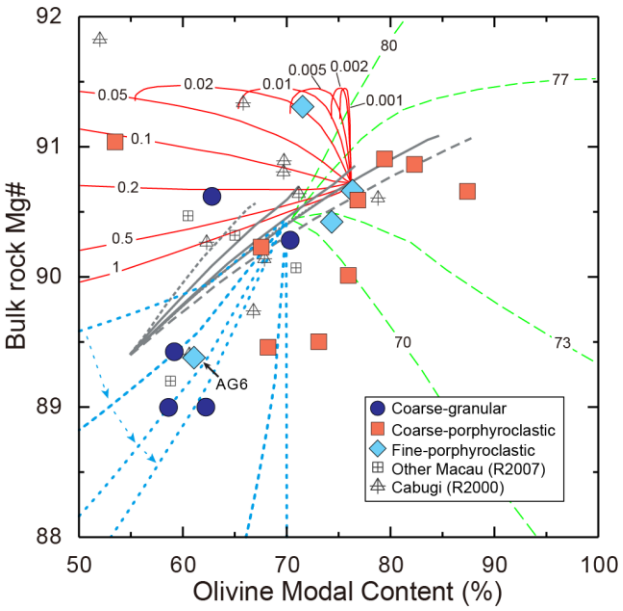

Fig. 13. Olivine modal content (%) vs. bulk rock Mg# in the studied xenoliths compared to evolutions predicted for partial melting and reactive melt percolation in the mantle. Gray lines represent the composition evolution predicted by various partial melting models using a source composition with 89.3 Mg# and 55% of olivine up to complete consumption of clinopyroxene (Bodinier & Godard, 2014). Colored lines represent different melt-rock reactions after Bodinier & Godard (2014). Red solid lines correspond to precipitation of clino- and orthopyroxene at the expense of olivine and melt with different mass ratio of crystallized minerals versus infiltrated melt (numbers of the top of the curves). Green dashed lines show olivine-forming reactions with melts with different Mg# (numbers of the top of the curves). Blue dotted lines represent multiple episodes of refertilization, starting with low Mg# melts ('primitive' melt Mg#=74.5), in which the peridotites successively reacted with the evolved melt resulting from previous infiltration stage (Bodinier et al., 2008). Compositions of Macau peridotite xenoliths previously studied by Rivalenti et al. (2000) and (2007) are plotted for comparison.

Fine-porphyroclastic peridotites show a bimodal olivine grain size distribution and strong intragranular misorientations in the olivine porphyroclasts characterized by dynamic recrystallization (Figs. 3 and 4). At the high equilibrium temperatures recorded by these peridotites (≥1200°C, Fig. 9), diffusion is fast. The low annealing level of the microstructures in these peridotites, indicated by the high intragranular misorientations in the porphyroclasts (Figs. 2 and 3), implies therefore that the deformation episode that produced the recrystallization shortly predated their extraction from the mantle by the Macau volcanism.

The variation in recrystallized grain sizes between the various fine-porphyroclastic peridotites might record variations in stress (from ~75 MPa in AG6 to ~10 MPa using the recrystallized grain size paleopiezometer of Van der Wal et al., 1993), but the coarser recrystallized grain sizes result more probably from partial annealing. The stresses estimated for lherzolite AG6 are high and, for the equilibrium temperature of 1200°C of these peridotites, imply extremely high strain rates of 10^{-6} to 10^{-9} s^{-1} based on usual olivine flow laws (Chopra and Paterson, 1981; Hirth and Kohlstedt, 2003; Gouriet et al. 2019). The microstructure of these peridotites is indeed very similar to the mosaic microstructure of deep sheared kimberlite-borne peridotites, which has been traditionally attributed to the initial stages of kimberlite dyke formation, due to the high stresses and high rates inferred based on the recrystallized grain sizes and equilibrium temperatures (e.g., Green and Gueguen, 1974; Boullier, 1977; Skemer and Karato, 2008; Baptiste et al. 2012). Similar microstructures have been observed in the deepest mantle xenoliths from the Labait alkaline lavas in the Tanzanian craton (Vauchez et al., 2005) and from Malaita alnoites in the Ontong Java plateau (Tommasi and Ishikawa, 2014) with similar interpretations proposed.

Fine-porphyroclastic peridotites with high equilibration temperatures have also been described in Cenozoic peridotite xenoliths, which sample the mantle beneath major Neoproterozoic shear zones at the border of the Hoggar swell, N Africa (Kourim et al., 2015). However, in the Hoggar peridotites, equilibration temperatures are lower (1000-1100°C) and olivine recrystallization was associated with crystallization of elongated aggregates of clinopyroxene and amphibole. The fine-porphyroclastic microstructures were therefore interpreted as resulting from ductile reactivation and melt channeling in Neoproterozoic shear zones in response to the development of the Hoggar swell in the Cenozoic. However, in the fine-porphyroclastic peridotites from the Borborema province, there is no evidence for neocrystallization of pyroxenes or amphiboles within the recrystallized domains. Moreover, the fact that the recrystallized domains in the fine-porphyroclastic peridotites from the Borborema province do not align marking a foliation (Fig. 3e,f) and the lack of elongation of the pyroxenes suggests that the recrystallization was associated with high stresses, but low finite strains. This association, together with the equilibrium temperatures, which imply that these peridotites are derived from

the base of the lithospheric mantle, is consistent with localized deformation associated with the formation of the dykes that fed the Cenozoic magmatism.

Analysis of the olivine modal composition relative to the bulk rock Mg# implies that lherzolites AG7 and AG6 were affected by refertilization processes (Fig. 13). The Fe-rich compositions of olivine and pyroxenes in AG6 (Fig. 8a,b) further point to high cumulated melt-rock ratios. Ortho- and clinopyroxenes in these two lherzolites have unusual irregular, but rounded shapes, which clearly differ from those in coarse-porphyroclastic peridotites (cf. EBSD phase maps in Fig. 3). Yet determining when this refertilization occurred is difficult. At the high temperatures at which these peridotites equilibrated, chemical diffusion is fast. Disequilibrium in mineral chemistry at the sample scale, which would point to melt-rock interaction shortly before extraction is only observed in AG7. Harzburgites PC105 and PC109 plot along the partial melting trends in Fig. 13 and have higher Mg# in olivine and pyroxenes (Fig. 8a,b), but they also display chemical evidence for some melt-rock interaction, like enrichment in Ca in olivine (Fig. 8c).

5.2. Cenozoic geotherm and thermal evolution of the NBP lithospheric mantle

We do have evidence in this study supporting a rather hot Cenozoic geotherm beneath the North Borborema Province. As illustrated in Fig. 10, equilibrium conditions of the xenoliths are consistent with the surface heat flow of 60-70 mW/m^2 measured in the Borborema Province (Hamza et al., 2018) if the heat flow from the convective mantle is rather high (45mW/m^2). This implies a slightly hotter than average sublithospheric mantle beneath the Borborema Province, consistently with the low P-wave velocity anomaly imaged at 100 km depth beneath the Northern Borborema Province east of the Macau-Queimadas volcanic alignment (Simões Neto et al., 2019; Fig. 1) and with the weak low S-wave velocity anomaly imaged beneath this region in a recent global full-waveform tomography model (ca. -2%; French et al., 2013). The equilibrium geotherm that best fits the equilibrium temperature and pressure conditions of the Borborema Province is also consistent with the seismological constraints for the lithosphere-asthenosphere boundary (LAB) depth of 80km (Heit et al., 2007) and with the partial melting conditions calculated for the Macau most primitive basalts (1330-1415°C at 80-93km; Ngonge et al. 2015b; cf. Fig. 10). A hotter than average sublithospheric mantle may also account for the Cenozoic uplift of the Borborema Plateau (Almeida et al., 2015; Luz et al., 2015; Klöcking et al., 2018). The equilibrium temperatures of the studied xenoliths may therefore represent an equilibrium geotherm established in the Cenozoic in response to a slightly hotter than normal convective mantle temperature. Geophysical data imply that these conditions are still active today. Data on the xenoliths does not bring any constraints on the causes of the higher than average sublithospheric temperatures, which may result from a diffuse mantle upwelling, perturbation of the convective pattern by the São Francisco craton, or, as suggested by Simoes Neto et al.

(2018), lateral channeling of hot material from a mantle plume upwelling to the SW of the Province.

The present data also do not constrain the evolution through time of the upper mantle temperatures beneath the North Borborema Province. The estimated melting conditions for the most primitive basalts of the Cretaceous CMDS (ca. 1320 °C at 70 km depth; Ngonge et al., 2015a) are shallower than those for the Cenozoic Macau volcanics (Ngonge et al., 2015b, suggesting an even shallower LAB beneath the North Borborema Province in the Mesozoic. This suggests that the lithosphere beneath the NBP has probably cooled and thickened after the Mesozoic extension. The deepest xenoliths might therefore represent material accreted to the base of the lithosphere after the Mesozoic.

5.3. Seismic anisotropy in the lithospheric mantle: comparison with SKS splitting data

Shear wave splitting data in the Borborema Province is highly heterogeneous and does not relate in a simple way to neither the outcropping geological structures nor the absolute plate motion of the South American plate (Bastow et al., 2015). However, the station RCBR, which is the closest to sampling sites, being located ca. 50 km east of the Pico do Cabugi, displays a NNE-oriented fast S-wave polarization parallel to the trend of the Seridó belt and of the main Brasiliano shear zones in the region, and a high delay time (1.9 s) based on 9 individual measurements (Assumpção et al., 2011).

If we consider that at least part of the SKS splitting measured at RCBR is produced in the lithospheric mantle, the orientation of the fast polarization direction constrains the projection of the lineation on the horizontal plane to be oriented in the NNE direction (9±11°). However, there are no constraints on its plunge or on the dip of the foliation. To draw constraints on the orientation of the foliation and lineation in the lithospheric mantle, which would allow to discuss possible coupling between crustal and mantle structures, we estimate the contribution of the lithospheric mantle to the SKS splitting delay time (Δt) for three end-member orientations of the foliation and lineation in the lithospheric mantle, illustrated in Fig. 14, and compare these predictions to the observations at RCBR.

Common conversion point (CCP) receiver function stacks support that the Moho is at ~32km (Almeida et al., 2015) and the LAB is at ~80km based on the S receiver function data by Heit et al. (2007) in the Northern Borborema Province. The thickness of the lithospheric mantle in this region is therefore 48 km. Based on the thermobarometric data (Fig. 10), we divided the lithosphere into two layers and calculated the lithospheric mantle contribution to the measured delay time using the average seismic anisotropy of the low temperature peridotites (32 - 56km, < 1000 °C) and of the high-temperature ones (56 - 80 km, > 1000 °C).

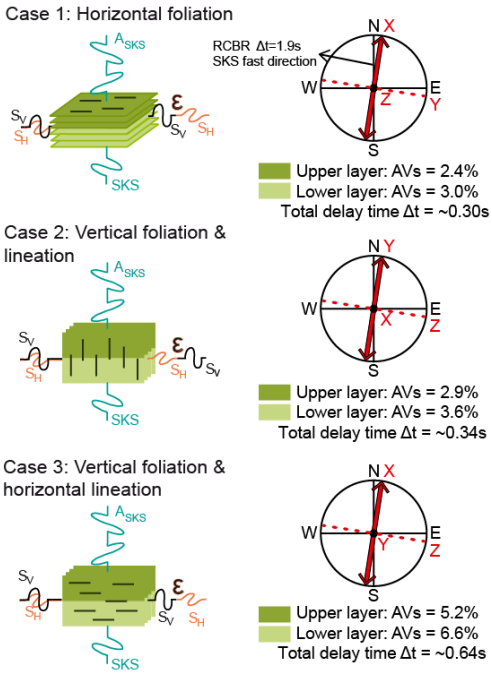

Fig. 14. Estimation of the maximum SKS splitting that may be produced in the lithospheric mantle for three end-member orientations of the flow directions and planes. Stereographic projections show the relation between the geographic (in black) and the structural (in red) reference frames in the three cases. The vertical is in all cases at the center of the diagram. The orientation of the fast SKS polarization (thick red arrow) is based on SKS splitting data for station RCBR.

1136

If the foliation is horizontal and the lineation NE-SW (case 1), the S-wave polarization anisotropy is 2.4% for upper lithospheric mantle and 3.0% for lower lithospheric mantle. The cumulated SKS delay time is only ~0.30s. If both the foliation and lineation are vertical (case 2), the fast SKS polarization constrains the direction of the foliation, and SKS waves propagate parallel to the lineation. The S-wave polarization anisotropy in this direction is low, like in case 1. It is 2.9% for upper layer and 3.6% for lower one and the delay time that may be cumulated in the lithospheric mantle is ~0.34s. If the foliation is vertical but the lineation is horizontal and parallel to the fast SKS polarization direction (case 3), the S-wave polarization anisotropy is higher. It is 5.2% in the upper lithospheric mantle and 6.6% for lower lithospheric mantle, leading to a cumulate delay time in the lithospheric mantle of 0.64s.

In case 3, the lithospheric mantle has a fabric consistent with the crustal deformation around station RCBR, which is dominated by dextral strike-slip in transpressional structures in the Seridó belt and in the shear zones that border it. This case would therefore imply a structuration in the lithospheric mantle coherent with the crustal deformation in the Brasiliano event. Seismic anisotropy in the lithospheric mantle, with anisotropy directions parallel or subparallel to the main nearby Neoproterozoic shear zones is also required by receiver function analysis on most stations in the Borborema Province (Lamarque and Julià, 2019). At station RCBR, this study proposes horizontal anisotropy axis trending NNE in the lithospheric mantle, consistent with case 3.

It is important to note that even for case 3, the lithospheric mantle can contribute to < 1/3 of the SKS delay time measured at the RCBR station (1.9 ± 0.2 s, Assumpção et al., 2011). Thus a large part of the SKS signal at RCBR has to be produced in the asthenosphere and, for the contributions of the lithosphere and asthenosphere to add up, asthenospheric flow directions

should not deviate much from NNE. Present-day absolute plate motion (APM) directions for NE Brazil do not follow this direction. Hotspot reference frame models, such as HS3-Nuvel-1A, predict an ENE direction, whereas no-net rotation models predict a NNW direction (Gripp and Gordon, 2002). However, a NNE flow direction in the sublithospheric mantle beneath the Borborema province is predicted by models in which the present-day mantle flow is calculated based on a density anomaly distribution derived from global seismic tomography models (cf. Fig. 8 in Assumpção et al., 2011).

5.4. Relations between the mantle structure and the geodynamical evolution of the Borborema Province

When did the deformation, annealing, and reactive melt percolation processes recorded by the xenoliths happen? How do they relate to the geodynamical evolution of NE Brazil? There are no ways of dating deformation processes in the mantle. However, we may try to use the data discussed in the previous sections to constrain the imprint of the different tectonic events that affected the Borborema Province in the lithospheric mantle.

The coarse-granular microstructures, with their well-equilibrated pyroxene-olivine grain boundaries, imply effective annealing, which, at the equilibrium temperatures of these xenoliths, require very long time delays, on the order of several hundreds of Ma. Although the temperature may have varied since the deformation of the xenoliths, to re-equilibrate the pyroxene-olivine grain boundaries in <100 Ma, temperatures ≥ 1100°C, that is >200°C above those recorded by the xenoliths at the time of extraction, are needed. Coarse-granular microstructures are well expressed among the low-equilibrium temperature xenoliths, suggesting that the shallow part of the lithospheric mantle beneath the Macau volcanics records essentially old tectonic events. The seismic anisotropy data in the region imply that this lithospheric structure results from Neoproterozoic dextral strike-slip and transpressional intraplate deformation. A pre-Mesozoic origin of this mantle fabric is also suggested by the higher annealing degree of the microstructures of the Borborema xenoliths relative to the Fernando de Noronha ones (Fig. 2). Indeed, Fernando de Noronha mantle xenoliths record deformation frozen up in the oceanic lithosphere by plate cooling, which post-dates the opening of the Atlantic (Liu et al., 2019).

Some coarse-porphyroclastic lherzolites have lower equilibrium temperatures (≤800°C) than most coarse-granular peridotites. This is not a sampling location effect, since both types of peridotites were sampled in Pico do Cabugi. The higher olivine intragranular misorientations and less equilibrated olivine and pyroxene grain shapes indicate less effective annealing, pointing to either slower annealing due to cooler temperatures or a more recent deformation event. In the first case, the deformation recorded by these xenoliths may also be associated with the Brasiliano event. In the second, these peridotite may record Cretaceous or even younger deformation

preserved in the shallow lithospheric mantle. In any case, the studied xenolith suite exhibits no evidence of strong deformation under low temperature conditions. There are no xenoliths displaying mylonitic microstructures, with marked grain size reduction of olivine and strong elongation of olivine and orthopyroxene porphyroclasts, which are usually observed in extensional shear zones developed in peridotite massifs under low temperature conditions (≤1000°C; e.g., Drury et al., 1991; Frets et al., 2014; Kaczmarek and Tommasi, 2011). Although annealing could have partially obliterated the olivine deformation microstructure, it cannot change the aspect ratios of the orthopyroxenes in a time scale of 100 Ma. Thus if the low temperature coarse-granular peridotites correspond to sections of the lithospheric mantle deformed during the Mesozoic, these are low strain zones and their olivine CPO and seismic anisotropy may still preserve orientations produced by the previous deformation episodes.

Based on the microstructures of the low equilibration temperature peridotites and on the seismic anisotropy data, we conclude therefore that the shallow sections of the lithospheric mantle of the Borborema province records coupled crust and mantle deformation during the formation of the Borborema shear zone system in the Neoproterozoic. The present dataset has no evidence for extensive reworking of the shallow lithospheric mantle by the extensional deformation in the Cretaceous or during the Cenozoic uplift of the province. Yet, the absence of (annealed or not) low-temperature mylonites in the xenolith sampling does not imply that shear zones accommodating a Mesozoic extension did not form in the shallow lithospheric mantle of the Borborema Province, since our sampling is punctual and such a deformation would be by nature heterogeneous.

The coarse-porphyroclastic microstructures that characterize the lower part of the lithospheric mantle (equilibrium temperatures > 1000°C) are more difficult to relate to a given tectonic episode. Partial melting conditions estimated for the Ceará-Mirim basalts suggest that the lithosphere-asthenosphere boundary was shallower in the Cretaceous than in the Cenozoic (cf. Fig. 10 and discussion section 5.2). This would imply that the deep lithospheric mantle beneath Borborema might be composed by material accreted by cooling since the Cretaceous. Comparison between the microstructures of these coarse-porphyroclastic peridotites with those of peridotite xenoliths from the nearby Fernando de Noronha (FN) archipelago, formed in response to Cenozoic volcanism onto 100-105 Ma old crust in the equatorial Atlantic (Liu et al., 2019) also favors a Mesozoic age for the deformation of these peridotites. Indeed, the olivine M2M and olivine and pyroxene shape factors of the Borborema peridotites overlap with the lower range of olivine M2M and shape factors, that is, with the most annealed microstructures of the FN peridotites (Fig. 2). The FN peridotites record an asthenospheric deformation, which has been frozen in the oceanic lithosphere by cooling and evolved by annealing since then (Liu et al., 2019). Their

deformation is therefore younger than the opening of the Equatorial Atlantic. The similar to slightly stronger annealing degree of the coarse-porphyroclastic Macau peridotites suggests that the deformation that produced these microstructures in the deep section of the lithospheric mantle beneath the Borborema province might be related to the Cretaceous extension. Thus, although this event did not result in widespread deformation of the shallow levels of the lithospheric mantle, it might have reworked the base of the lithosphere (bottom-up lithospheric thinning?). Yet the high SKS delay times in station RCBR do not favor strong deviations in flow direction from NNE across the entire lithosphere-asthenosphere section, implying that either strains were small and did not change the Neoproterozoic CPO orientations or that flow directions during extension were at high angle to the extensional structures in the Cretaceous basins and to the Equatorial Atlantic spreading directions.

Finally, the very low annealing degree and high equilibration temperatures of the fine-grained porphyroclastic microstructures necessarily imply deformation close in time to the Cenozoic Macau volcanism. Based on the microstructural evidence for high stresses, but low finite strains for this deformation, we propose that it is related to the formation of the dykes that brought the Macau volcanics to the surface. The equilibration temperatures of the xenoliths imply a rather hot geotherm, leading to an 80-km thick lithosphere in the Cenozoic. This is consistent with melting depths inferred for the Macau basalts (Ngonge et al., 2015b). It is also coherent with the present-day thermal state of the lithospheric and sublithospheric mantle as imaged by geophysical data .

Dating the reactive melt percolation events is even more difficult than the deformation ones. The equilibrated microstructures and the coherent olivine and pyroxene CPOs in the coarse-granular peridotites undoubtedly point to a Brasiliano or older reactive melt percolation event. Coarse-porphyroclastic peridotites record younger melt percolation events, which in some cases predated or were synchronous to the main deformation recorded by the samples. However, in other cases, like in the coarse-porphyroclastic harzburgites, melt percolation post-dated the main deformation. Finally, the non-equilibrated chemical compositions at the sample scale observed in many samples, in particular the high-temperature coarse-porphyroclastic harzburgites, point to a last event of melt percolation that shortly predated the extraction of the peridotites. In summary, this peridotite suite recorded multiple reactive melt percolation events, probably well separated in time and related to the different magmatic episodes recorded in the crust.

6. Conclusion

Integrated analysis of microstructures, crystal preferred orientations, mineral chemical compositions, and equilibrium temperatures in a suite of 22 peridotite xenoliths reveals that the lithospheric mantle beneath the Northern Borborema Province preserves microstructures related to different deformation

episodes since at least the Neoproterozoic. In all cases, olivine CPO points to deformation by dislocation creep with dominant activation of [100](010) slip system. However, the deformation microstructures were modified by variable degrees of annealing. The analysis of the extent of the annealing considering the equilibration temperatures allows rough 'dating' of the deformation episodes and relating them to the major deformation events recorded in the crust. The well-annealed olivine microstructures and pyroxene shapes in coarse-granular peridotites equilibrated at ca. 900°C indicate that the last deformation event that affected these peridotites is several hundreds of Ma old. In contrast, the fine-porphyroclastic peridotites, which have equilibrium temperatures ≥1200°C, have suffered a high stress deformation, which shortly predated their extraction, probably related to the dykes that fed the Cenozoic volcanism. The coarse-porphyroclastic microstructures, which are observed both in the shallow and deep lithospheric mantle are more difficult to relate to a given tectonic episode. Yet comparison between the microstructures of these peridotites and those of peridotite xenoliths from nearby Fernando de Noronha island, which sample the oceanic mantle lithosphere of an old domain of the Equatorial Atlantic, suggest that the high-temperature coarse-porphyroclastic peridotites may record deformation related to the Cretaceous extension. Multiple reactive melt percolation events, probably well spaced in time, may also be inferred based on the microstructures, modal, and mineral compositions of the xenoliths.

Comparison of the computed seismic anisotropy of the lithospheric mantle based on the xenolith data to SKS splitting in nearby RCBR station supports that the strongest contribution of the lithospheric mantle to the measured anisotropy would correspond to a frozen strike-slip fabric parallel to the major NNE-NE Neoproterozoic shear zones in the region. A shallow lithospheric mantle fabric parallel to the Neoproterozoic shear zones is also suggested by anisotropic receiver functions (Lamarque and Julia, 2019). These observations corroborate the conclusion that the shallow lithospheric mantle in the Northern Borborema province still preserves a structure acquired by coupled crust-mantle deformation during the formation of the Borborema shear zone system in the Neoproterozoic. It also suggests that Cretaceous extension, which seems to be recorded in the deeper sections of the lithosphere, did not produce pervasive reworking of the shallow lithospheric mantle, pointing to 'partial' or total crust-mantle decoupling during this event. However, even if the entire lithospheric mantle has a frozen strike-slip fabric parallel to the major NNE-NE Neoproterozoic shear zones in the region, it can produce <1/3 of the measured delay time of 1.9s in station RCBR. Thus most of the measured SKS splitting in RCBR should record flow in the sublithospheric mantle, which also has a NNE orientation, which is not parallel to the APM, but is consistent with predictions of mantle circulation models for this region.

Finally, equilibrium temperatures and petrological compositions of the xenoliths indicate a rather hot Cenozoic geotherm, implying a ca. 80 km thick

lithosphere. This estimate is consistent with the melting conditions estimated for the formation of the Macau basalts (Ngonge et al. 2015). It is also coherent with geophysical data that point to a present-day 80-km thick lithosphere (Heit et al. 2007) and hotter than average sublithospheric mantle beneath this region (French et al., 2013; Simões Neto et al., 2019).

7. Acknowledgments

S. Liu was funded during his 14-month stay in Geosciences Montpellier by the China Scholarship Council. M.M. was supported by projects MIUR-PRIN 2005-2005049821 and 2017-20178LPCPW. C. Archanjo and M.H.B.M. Hollanda are thanked for assistance during field work. D. Delmas and C. Nevado prepared high-quality polished thin sections for EBSD measurements, which were performed with the assistance of F. Barou at the EBSD-SEM INSU national facility at Géosciences Montpellier (CNRS & Université de Montpellier). Electron microprobe analyses were carried out with the assistance of B. Boyer at the Service Microsonde Sud, Université de Montpellier. S. Piazolo and T. Morishita are warmly thanked for their constructive reviews.

The data used in this article are presented in the figures, tables, and supporting material. The raw EBSD data are available from the corresponding author upon request.

8. References

Abramson, E.H., Brown, J.M., Slutsky, L.J., Zaug, J.M., 1997. The elastic constants of San Carlos olivine to 17 GPa. J Geophys Res-Sol Ea. 102, 12253-12263.

Almeida, Y.B., Julià, J., Frassetto, A., 2015. Crustal architecture of the Borborema Province, NE Brazil, from receiver function CCP stacks: Implications for Mesozoic stretching and Cenozoic uplift. Tectonophys. 649, 68-80.

Ancelmi, M.F., Santos, T.J.S.d., Amaral, W.d.S., Fuck, R.A., Dantas, E.L., Zincone, S.A., 2015. Provenance of metasedimentary rocks from the Ceará Central Domain of Borborema Province, NE Brazil: implications for the significance of associated retrograded eclogites. J. S. Am. Earth Sci. 58, 82-99.

Anderson, O.L., Isaak, D., Oda, H., 1992. High-Temperature Elastic-Constant Data on Minerals Relevant to Geophysics. Rev. Geophys. 30, 57-90.

Archanjo, C. J., Hollanda, M. H. B., Rodrigues, S. W., Neves, B. B., & Armstrong, R., 2008. Fabrics of pre-and syntectonic granite plutons and chronology of shear zones in the Eastern Borborema Province, NE Brazil. J. Struct. Geol. 30, 310-326

Archanjo, C.J., Viegas, L.G.F., Hollanda, M.H.B.M., Souza, L.C., Liu, D., 2013. Timing of the HT/LP transpression in the Neoproterozoic Seridó Belt

(Borborema Province, Brazil): Constraints from UPb (SHRIMP) geochronology and implications for the connections between NE Brazil and West Africa. Gondwana Res. 23, 701-714.

Assumpção, M., Guarido, M., van der Lee, S., Dourado, J.C., 2011. Upper-mantle seismic anisotropy from SKS splitting in the South American stable platform: A test of asthenospheric flow models beneath the lithosphere. Lithosphere 3, 173-180.

Bachmann, F., Hielscher, R., Schaeben, H., 2010. Texture Analysis with MTEX – Free and Open Source Software Toolbox. Solid State Phenomena 160, 63-68.

Bachmann, F., Hielscher, R., Schaeben, H., 2011. Grain detection from 2d and 3d EBSD data - Specification of the MTEX algorithm. Ultramicroscopy 111, 1720-1733.

Baker, M.B., Stolper, E.M., 1994. Determining the Composition of High-Pressure Mantle Melts Using Diamond Aggregates. Geochim. Cosmochim. Acta 58, 2811-2827.

Baptiste V., Tommasi, A., Demouchy S., 2012. Deformation and hydration of the lithospheric mantle beneath the Kaapval craton. Lithos 149, 31-50.

Barruol, G., Bonnin, M., Pedersen, H., Bokelmann, G.H.R. & Tiberi, C., 2011. Belt-parallel mantle flow beneath a halted continental collision: the Western Alps. Earth Planet. Sci. Lett. 302, 429-438 .

Bascou, J., Tommasi, A., Mainprice, D. 2002. Plastic deformation and development of clinopyroxene lattice preferred orientations in eclogites. *J. Struct. Geol.,* **24**: 1357-1368

Bastow, I.D., Julia, J., do Nascimento, A.F., Fuck, R.A., Buckthorp, T.L., McClellan, J.J., 2015. Upper mantle anisotropy of the Borborema Province, NE Brazil: Implications for intra-plate deformation and sub-cratonic asthenospheric flow. Tectonophys. 657, 81-93.

Berger, E.T., Vannier, M., 1984. Dunites in Alkali Basalts from Oceanic Volcanic Islands - Petrological Approach. Bull. Mineral. 107, 649-663.

Bodinier, J.L., Garrido, C.J., Chanefo, I., Bruguier, O., Gervilla, F., 2008. Origin of Pyroxenite-Peridotite Veined Mantle by Refertilization Reactions: Evidence from the Ronda Peridotite (Southern Spain). J. Petrol. 49, 999-1025.

Bodinier, J.L., Godard, M., 2014. Orogenic, Ophiolitic, and Abyssal Peridotites, in: Holland, H.D., Turekian, K.K. (Eds.), Treatise on Geochemistry (Second Edition). Elsevier, Oxford, pp. 103-167.

Boullier, A.M., 1977. Structure des péridotites en enclaves dans les kimberlites d'Afrique du Sud. Conséquences sur la constitution du manteau supérieur. Bull. Soc. Française Minéral. Cristall.. 100, 214–229.

Bonnin, M., Tommasi, A., Hassani, R., Chévrot, S., Wookey, J., Barruol, G., 2011. Numerical modeling of upper mantle anisotropy beneath a migrating strike-slip plate boundary : the San Andreas fault system. Geophys. J. Intern. 191, 436-458

Brey, G.P., Kohler, T., 1990. Geothermobarometry in 4-Phase Lherzolites .2. New Thermobarometers, and Practical Assessment of Existing Thermobarometers. J. Petrol. 31, 1353-1378.

Bystricky, M., Kunze, K., Burlini, L., Burg, J. P.; 2000. High shear strain of olivine aggregates: Rheological and seismic consequences. Science 290, 1564-1567

Caby, R., Sial, A., Arthaud, M., Vauchez, A., 1991. Crustal evolution and the Brasiliano orogeny in Northeast Brazil. In: The West African orogens and Circum Atlantic correlatives. Springer- Verlag, pp. 373-397.

Castro, D.L., Bezerra, F.H.R., Sousa, M.O.L., Fuck, R.A., 2012. Influence of Neoproterozoic tectonic fabric on the origin of the Potiguar Basin, northeastern Brazil and its links with West Africa based on gravity and magnetic data. J. Geodyn. 54, 29-42

Castro, D.L., Oliveira, D.C., Gomes Castelo Branco, R.M., 2007. On the tectonics of the Neocomian Rio do Peixe Rift Basin, NE Brazil: Lessons from gravity, magnetics, and radiometric data. J. S. Am. Earth Sci. 24, 184-202.

Chai, M., Brown, J.M., Slutsky, L.J., 1997. The elastic constants of an aluminous orthopyroxene to 12.5 GPa. J Geophys Res-Sol Ea. 102, 14779-14785.

Chopra, P.N., Paterson, M.S., 1981. The Experimental Deformation of Dunite. Tectonophys. 78, 453-473.

Comin-Chiaramonti, P., Demarchi, G., Girardi, V.A.V., Princivalle, F., Sinigoi, S., 1986. Evidence of mantle metasomatism and heterogeneity from peridotite inclusions of northeastern Brazil and Paraguay. Earth Planet. Sci. Lett. 77, 203-217.

Costa, A.P., Cunha, A.L.C., Cavalcante, R., Medeiros, V.C., Spicily, A.L., Dantas, A.R., 2016. Carta Geologica Integrada de Areas de Relevante Interesse Mineral: Area Serido, Projeto Metalogenia das Provincias Minerais do Brasil, Escala 1:350000, Companhia de Pesquisas de Recursos Minerais, Brazil.

Darros de Matos, R.M., 1999. History of the northeast Brazilian rift system: kinematic implications for the break-up between Brazil and West Africa. Geological Society, London, Special Publications. 153, 55-73.

Drury, M.R., Vissers, R.L.M., Vanderwal, D., Strating, E.H.H., 1991. Shear Localization in Upper Mantle Peridotites. Pure Appl Geophys. 137, 439-460.

Durham, W.B. and Goetze, C., 1977. Plastic flow of oriented single crystals of olivine. 1.Mechanical data. J. Geophys. Res. 82: doi: 10.1029/JB082i036p05737

Fei, H., Koizumi, S., Sakamoto, N., Hashiguchi, M., Yurimoto, H., Marquardt, K., Katsura, T., 2016. New constraints on upper mantle creep mechanism inferred from silicon grain-boundary diffusion rates. Earth Planet. Sci. Lett.. 433, 350-359.

Fisler, D. K., Mackwell, S. J., Petsch, S., 1997. Grain boundary diffusion in

enstatite. Physics and Chemistry of Minerals. 24, 264-273.
Fodor, R.V., Sial, A.N., Gandhok, G., 2002. Petrology of spinel peridotite xenoliths from northeastern Brazil: lithosphere with a high geothermal gradient imparted by Fernando de Noronha plume. J. S. Am. Earth Sci. 15, 199-214.
French, S., Lekic, V., Romanowicz, B., 2013. Waveform Tomography Reveals Channeled Flow at the Base of the Oceanic Asthenosphere. Science. 342, 227-230.
Frets, E.C., Tommasi, A., Garrido, C.J., Vauchez, A., Mainprice, D., Targuisti, K., Amri, I., 2014. The Beni Bousera Peridotite (Rif Belt, Morocco): an Oblique-slip Low-angle Shear Zone Thinning the Subcontinental Mantle Lithosphere. J. Petrol. 55, 283-313.
Ganade de Araujo, C.E., Weinberg, R.F. and Cordani, U.G., 2014. Extruding the Borborema Province (NE-Brazil): a two-stage Neoproterozoic collision process. Terra Nova 26, 157-168.
Ganade de Araujo, C.E., Cordani, U.G., Agbossoumounde, Y., Caby, R., Basei, M.A.S., Weinberg, R.F. and Sato, K., 2016. Tightening-up NE Brazil and NW Africa connections: New U–Pb/Lu–Hf zircon data of a complete plate tectonic cycle in the Dahomey belt of the West Gondwana Orogen in Togo and Benin. Precambrian Res. 276, 24-42.
Gouriet, K., Cordier, P., Garel, F., Thoraval, C., Demouchy, S., Tommasi, A., Carrez, P., 2019. Dislocation dynamics modelling of the power-law breakdown in olivine single crystals: Toward a unified creep law for the upper mantle. Earth Planet. Sci. Lett. 506, 282-291.
Green, H.W., Gueguen, Y., 1974. Origin of Kimberlite Pipes by Diapiric Upwelling in Upper Mantle. Nature. 249, 617-620.
Gripp, A., Gordon, R., 2002. Young tracks of hotspots and current plate velocities. Geophys. J. Int. 150, 321–361.
Hammond, J.O.S., Kendall, J.M., Wookey, J., Stuart, G.W., Keir, D., Ayele, A., 2014. Differentiating flow, melt, or fossil seismic anisotropy beneath Ethiopia, Geochem. Geophys. Geosyst. (15) DOI:10.1002/2013GC005185
Hamza, V.M., Vieira, F.P., Silva, R.T.A., 2018. Anomalous heat flow belt along the continental margin of Brazil. Int J Earth Sci. 107, 19-33.
Hansen, L. N., Zhao, Y. H., Zimmerman, M. E., Kohlstedt, D. L., 2014. Protracted fabric evolution in olivine: Implications for the relationship among strain, crystallographic fabric, and seismic anisotropy. Earth Planet. Sci. Lett. 387, 157-168
Heine, C., Zoethout, J., Muller, R.D., 2013. Kinematics of the South Atlantic rift. Solid Earth 4, 215-253.
Heit, B., Sodoudi, F., Yuan, X., Bianchi, M., Kind, R., 2007. An S receiver function analysis of the lithospheric structure in South America. Geophys. Res. Lett. 34.
Hielscher, R., Schaeben, H., 2008. A novel pole figure inversion method: specification of the MTEX algorithm. J. Appl. Crystallogr. 41, 1024-1037.

Higgie, K., Tommasi, A., 2012. Feedbacks between deformation and melt distribution in the crust–mantle transition zone of the Oman ophiolite. Earth Planet. Sci. Lett. 359, 61-72.
Higgie, K., Tommasi, A., 2014. Deformation in a partially molten mantle: Constraints from plagioclase lherzolites from Lanzo, western Alps. Tectonophys. 615, 167-181.
Hirth, G., Kohlstedt, D., 2003. Rheology of the upper mantle and the mantle wedge: A view from the experimentalists. Inside the subduction Factory, *138*, 83-105.
Hollanda, M.H.B.M., Archanjo, C.J., Bautista, J.R., Souza, L.C., 2015. Detrital zircon ages and Nd isotope compositions of the Seridó and Lavras da Mangabeira basins (Borborema Province, NE Brazil): Evidence for exhumation and recycling associated with a major shift in sedimentary provenance. Precambrian Res. 258, 186-207.
Hollanda, M.H.B.M., Archanjo, C.J., Souza, L.C., Liu, D.Y., Armstrong, R., 2011. Long-lived Paleoproterozoic granitic magmatism in the Serido-Jaguaribe domain, Borborema Province-NE Brazil. J. S. Am. Earth Sci. 32, 287-300.
Hollanda, M.H.B.M., Archanjo, C.J., Macedo Filho, A.A., Fossen, H., Ernst, R.E., Castro, D.L.d., Melo, A.C. and Oliveira, A.L., 2018. The Mesozoic Equatorial Atlantic Magmatic Province (EQUAMP), in: Dyke Swarms of the World: A Modern Perspective. Springer Singapore, pp. 87-110.
Isaak, D.G., Ohno, I., Lee, P.C., 2006. The elastic constants of monoclinic single-crystal chrome-diopside to 1,300 K. Phys Chem Miner. 32, 691-699.
Jackson, J.M., Sinogeikin, S.V., Bass, J.D., 2007. Sound velocities and single-crystal elasticity of orthoenstatite to 1073 K at ambient pressure. Phys. Earth Planet. Inter. 161, 1-12.
Kaczmarek, M.A., Tommasi, A., 2011. Anatomy of an extensional shear zone in the mantle, Lanzo massif, Italy. Geochem. Geophys. Geosyst. 12, Q0AG06, doi:10.1029/2011GC003627.
Kelemen, P.B., 1990. Reaction between Ultramafic Rock and Fractionating Basaltic Magma .1. Phase-Relations, the Origin of Calc-Alkaline Magma Series, and the Formation of Discordant Dunite. J. Petrol. 31, 51-98.
Klemme, S., 2004. The influence of Cr on the garnet-spinel transition in the Earth's mantle: experiments in the system MgO-Cr2O3-SiO2 and thermodynamic modelling. Lithos 77, 639-646.
Knesel, K.M., Souza, Z.S., Vasconcelos, P.M., Cohen, B.E., Silveira, F.V., 2011. Young volcanism in the Borborema Province, NE Brazil, shows no evidence for a trace of the Fernando de Noronha plume on the continent. Earth Planet. Sci. Lett. 302, 38-50.
Kostopoulos, D.K., 1991. Melting of the Shallow Upper Mantle - a New Perspective. J. Petrol. 32, 671-699.
Kourim, F., Vauchez, A., Bodinier, J. L., Alard, O., Bendaoud, A., 2015. Subcontinental lithosphere reactivation beneath the Hoggar swell (Algeria):

Localized deformation, melt channeling and heat advection. Tectonophys. 650, 18-33.
Lamarque, G., Julià, J., 2019. Lithospheric and sub-lithospheric deformation under the Borborema Province of NE Brazil from receiver function harmonic stripping. Solid Earth Discuss. https://doi.org/10.5194/se-2019-41.
Le Roux, V., Bodinier, J.L., Tommasi, A., Alard, O., Dautria, J.M., Vauchez, A., Riches, A.J.V., 2007. The Lherz spinel lherzolite: Refertilized rather than pristine mantle. Earth Planet. Sci. Lett. 259, 599-612.
Lima, M.V.A.G.d., Berrocal, J., Soares, J.E.P., Fuck, R.A., 2015. Deep seismic refraction experiment in northeast Brazil: New constraints for Borborema province evolution. J. S. Am. Earth Sci. 58, 335-349.
Lissenberg, C.J., Dick, H.J.B., 2008. Melt–rock reaction in the lower oceanic crust and its implications for the genesis of mid-ocean ridge basalt. Earth Planet. Sci. Lett. 271, 311-325.
Liu, S., Tommasi, A., Vauchez, A., Mazzucchelli, M. 2019. Deformation, annealing, melt-rock interaction, and seismic properties of an old domain of the equatorial Atlantic lithospheric mantle. Tectonics 38, doi: 1029/2018TC005373.
Luz, R.M.N., Julià, J., do Nascimento, A.F., 2015. Bulk crustal properties of the Borborema Province, NE Brazil, from P-wave receiver functions: Implications for models of intraplate Cenozoic uplift. Tectonophys. 644-645, 81-91.
Mainprice, D., Bachmann, F., Hielscher, R., Schaeben, H., 2014. Descriptive tools for the analysis of texture projects with large datasets using MTEX: strength, symmetry and components. Geol. Soc. London Spec. Publ. 409, 251-271.
Mainprice, D., Hielscher, R., Schaeben, H., 2011. Calculating anisotropic physical properties from texture data using the MTEX open-source package. Geol. Soc. London Spec. Publ. 360, 175-192.
Marques, F.O., Nogueira, F.C.C., Bezerra, F.H.R., Castro, D.L., 2014. The Araripe Basin in NE Brazil: An intracontinental graben inverted to a high-standing horst. Tectonophys. 630, 251-264.
Klöcking, M., Tribaldos, V.R., Hoggard, M., White, N., Maclennan, J., Rezende Guimarães, A., 2018. Linking uplift and volcanism of the Borborema Province, northeast Brazil. EGU General Assembly Conference Abstracts 20, p. 9966.
Mercier, J.C.C., Nicolas, A., 1975. Textures and Fabrics of Upper-Mantle Peridotites as Illustrated by Xenoliths from Basalts. J. Petrol. 16, 454-487.
Mizusaki, A.M.P., Thomaz-Filho, A., Milani, E.J., Césero, P., 2002. Mesozoic and Cenozoic igneous activity and its tectonic control in northeastern Brazil. J. S. Am. Earth Sci. 15, 183-198.
Moulin, M., Aslanian, D., Unternehr, P., 2010. A new starting point for the South and Equatorial Atlantic Ocean. Earth-Sci Rev. 98, 1-37.
Neves, S.P., 2003. Proterozoic history of the Borborema province (NE Brazil):

Correlations with neighboring cratons and Pan-African belts and implications for the evolution of western Gondwana. Tectonics. 22.
Ngonge, E.D., de Hollanda, M.H.B.M., Archanjo, C.J., de Oliveira, D.C., Vasconcelos, P.M.P., Muñoz, P.R.M., 2016a. Petrology of continental tholeiitic magmas forming a 350-km-long Mesozoic dyke swarm in NE Brazil: Constraints of geochemical and isotopic data. Lithos. 258-259, 228-252.
Ngonge, E.D., de Hollanda, M.H.B.M., Pimentel, M.M., de Oliveira, D.C., 2016b. Petrology of the alkaline rocks of the Macau Volcanic Field, NE Brazil. Lithos. 266-267, 453-470.
Nimis, P., Grutter, H., 2010. Internally consistent geothermometers for garnet peridotites and pyroxenites. Contrib Mineral Petr. 159, 411-427.
Niu, Y.L., 1997. Mantle melting and melt extraction processes beneath ocean ridges: Evidence from abyssal peridotites. J. Petrol. 38, 1047-1074.
Nogueira, F.C.C., Marques, F.O., Bezerra, F.H.R., Castro, D.L., Fuck, R.A., 2015. Cretaceous intracontinental rifting and post-rift inversion in NE Brazil: Insights from the Rio do Peixe Basin. Tectonophysics 644-645, 92-107.
O'Neill, H.S.C., 1981. The transition between spinel lherzolite and garnet lherzolite, and its use as a geobarometer. Contrib. Mineral. Petr. 77, 185-194.
Oliveira, R.G., Medeiros, W.E., 2012. Evidences of buried loads in the base of the crust of Borborema Plateau (NE Brazil) from Bouguer admittance estimates. J. S. Am. Earth Sci. 37, 60-76.
Perlingeiro, G., Vasconcelos, P.M., Knesel, K.M., Thiede, D.S., Cordani, U.G., 2013. Ar-40/Ar-39 geochronology of the Fernando de Noronha Archipelago and implications for the origin of alkaline volcanism in the NE Brazil. J. Volcanol. Geotherm. Res. 249, 140-154.
Princivalle, F., Salviulo, G., Fabro, C., Demarchi, G., 1994. Inter- and intra-crystalline temperature and pressure estimates on pyroxenes from NE Brazil mantle xenoliths. Contrib. Mineral. Petr. 116, 1-6.
Qi, C., Hansen, L. N., Wallis, D., Holtzman, B. K., Kohlstedt, D. L., 2018. Crystallographic Preferred Orientation of Olivine in Sheared Partially Molten Rocks: The Source of the "a-c Switch". Geochem. Geophys. Geosyst. 19, 316-336
Rivalenti, G., Mazzucchelli, M., Girardi, V.A.V., Vannucci, R., Barbieri, M.A., Zanetti, A., Goldstein, S.L., 2000. Composition and processes of the mantle lithosphere in northeastern Brazil and Fernando de Noronha: evidence from mantle xenoliths. Contrib. Mineral. Petr. 138, 308-325.
Rivalenti, G., Zanetti, A., Girardi, V.A.V., Mazzucchelli, M., Tassinari, C.C.G., Bertotto, G.W., 2007. The effect of the Fernando de Noronha plume on the mantle lithosphere in north-eastern Brazil. Lithos 94, 111-131.
Tribaldos, V. R., White, N.J., Roberts, G.G., Hoggard, M.J., 2017. Spatial and temporal uplift history of South America from calibrated drainage analysis. Geochem. Geophys. Geosyst. 18, 2321-2353.
Sa, J.M., McReath, I., Leterrier, J., 1995. Petrology, Geochemistry and

Geodynamic Setting of Proterozoic Igneous Suites of the Oros Fold Belt (Borborema Province, Northeast Brazil). J. S. Am. Earth Sci. 8, 299-314.
Sang, L.Q., Bass, J.D., 2014. Single-crystal elasticity of diopside to 14 GPa by Brillouin scattering. Phys. Earth Planet. Inter. 228, 75-79.
Santos, E.J., Schmus, W.R.V., Kozuch, M., Neves, B.B.d.B., 2010. The Cariris Velhos tectonic event in Northeast Brazil. J. S. Am. Earth Sci. 29, 61-76.
Schutt, D.L., Lowry, A.R., Buehler, J.S., 2018. Moho temperature and mobility of lower crust in the western United States. Geology 46, 219–222.
Silveira, F.V., 2006. Magmatismo cenozóico da porção central do Rio Grande do Norte, NE do Brasil. Ph.D. Thesis, Univ. Federal do Rio Grande do Norte, UFRN, Brazil.
Simões Neto, F.L., Julià, J. Schimmel, M., 2019. Upper-mantle structure of the Borborema Province, NE Brazil, from *P*-wave tomography: implications for rheology and volcanism, *Geophys. J. Intern.* 216, 231–250.
Skemer, P., Karato, S.I., 2008. Sheared lherzolite xenoliths revisited. J. Geophys. Res. 113, B07205.
Souza, Z.S., Vasconcelos, P., Nascimento, M., V. Silveira, F., S. Paiva, H., Dias, L.G., Thiede, D., Carmo, I., 2003. 40Ar/39Ar geochronology of Mesozoic and Cenozoic magmatism in NE Brazil. In Proceedings of IV South American Symposium on Isotope Geology, 691-694.
Souza, Z.S., Kalsbeek, F., Deng, X.-D., Frei, R., Kokfelt, T.F., Dantas, E.L., Li, J.-W., Pimentel, M.M., Galindo, A.C., 2016. Generation of continental crust in the northern part of the Borborema Province, northeastern Brazil, from Archaean to Neoproterozoic. J. S. Am. Earth Sci. 68, 68-96.
Taylor, W.R., 1998. An experimental test of some geothermometer and geobarometer formulations for upper mantle peridotites with application to the thermobarometry of fertile lherzolite and garnet websterite. Neues Jb. Miner. Abh. 172, 381-408.
Tikoff, B., Russo, R., Teyssier, C., Tommasi, A. 2004. Mantle-driven deformation of orogenic zones and clutch tectonics. In: J. Grocott, K. McCaffrey, G. Taylor & B. Tikoff (eds) Vertical and horizontal decoupling in the lithosphere. Geol. Soc. London Spec. Publ. 227, 41-64.
Tommasi, A., Ishikawa, A., 2014. Microstructures, composition, and seismic properties of the Ontong Java Plateau mantle root. *Geochem. Geophys. Geosyst.*, 15, doi: 10.1002/2014GC005452
Tommasi, A., Vauchez, A., 2015. Heterogeneity and anisotropy in the lithospheric mantle. Tectonophys. 661, 11-37.
Tommasi, A., Vauchez, A., Daudré, B., 1995. Initiation and propagation of shear zones in a heterogeneous continental lithosphere. J. Geophys. Res. 100, 22083-22101.
Tommasi, A, Mainprice, D., Canova, G., Chastel, Y. 2000. Viscoplastic self-consistent and equilibrium-based modeling of olivine lattice preferred

orientations. Implications for the upper mantle seismic anisotropy. J. Geophys. Res. 105, 7893-7908

Tommasi, A., Tikoff, B., Vauchez, A. 1999. Upper mantle tectonics: Three-dimensional deformation, olivine crystallographic fabrics and seismic properties. Earth Planet. Sci. Lett. 168, 173-186

Tommasi, A., Vauchez, A., Ionov, D. A., 2008. Deformation, static recrystallization, and reactive melt transport in shallow subcontinental mantle xenoliths (Tok Cenozoic volcanic field, SE Siberia). Earth Planet. Sci. Lett. 272, 65-77

Ussami, N., Molina, E.C., Medeiros, W.E., 1999. Novos vinculos sobre a Evolução Térmica da Margem Continental Leste do Brasil, *In VII National Symposium on Tectonic Studies, Extended Abstracts*: Sociedade Brasileira de Geologia, **7,** 20–23

Van der Wal, D., Chopra, P., Drury, M., Gerald, J.F., 1993. Relationships between dynamically recrystallized grain size and deformation conditions in experimentally deformed olivine rocks. Geophys. Res. Lett. 20, 1479-1482.

van Schmus, W.R., Oliveira, E.P., da Silva Filho, A.F., Toteu, S.F., Penaye, J., Guimarães, I.P., 2008. Proterozoic links between the Borborema Province, NE Brazil, and the Central African Fold Belt. Geol. Soc. London Spec. Publ. 294, 69-99.

Vauchez, A., Nicolas, A., 1991. Mountain building: strike-parallel motion and mantle anisotropy. Tectonophys. 185, 183-201

Vauchez, A., Dineur, F., Rudnick, R., 2005. Microstructure, texture and seismic anisotropy of the lithospheric mantle above a mantle plume: insights from the Labait volcano xenoliths (Tanzania). Earth and Planetary Science Letters 232, 295-314.

Vauchez, A., Neves, S., Caby, R., Corsini, M., Egydio-Silva, M., Arthaud, M., Amaro, V., 1995. The Borborema Shear Zone System, NE Brazil. J. S. Am. Earth Sci. 8, 247-266.

Vauchez, A., Tommasi, A., Mainprice, D., 2012. Faults (shear zones) in the Earth's mantle. Tectonophys. 558, 1-27.

Viegas, L.G.F., Archanjo, C.J., Hollanda, M.H.B.M. and Vauchez, A., 2014. Microfabrics and zircon U/Pb (SHRIMP) chronology of mylonites from the Patos shear zone (Borborema Province, NE Brazil). Precambrian Research 243, 1-17.

Walter, M.J., Sisson, T.W., Presnall, D.C., 1995. A Mass Proportion Method for Calculating Melting Reactions and Application to Melting of Model Upper-Mantle Lherzolite. Earth Planet. Sci. Lett. 135, 77-90.

Workman, R.K., Hart, S.R., 2005. Major and trace element composition of the depleted MORB mantle (DMM). Earth Planet. Sci. Lett. 231, 53-72.

Wu, J., Zhang, Z., Kong, F., Yang, B.B., Yu, Y., Liu, K.H., Gao, S.S., 2015. Complex seismic anisotropy beneath western Tibet and its geodynamic implications. Earth Planet. Sci. Lett. 413, 167-175.

Crust-mantle coupling during continental convergence and break-up: Constraints from peridotite xenoliths from the Borborema Province, northeast Brazil

Shiran Liu[1,2], Andréa Tommasi[1], Alain Vauchez[1], Maurizio Mazzucchelli[3]

[1]Géosciences Montpellier, CNRS & Université de Montpellier, Montpellier, France.
[2]Key Laboratory of Orogenic Belts and Crustal Evolution, School of Earth and Space Sciences, Peking University, Beijing, China.
[3]Dipartimento di Scienze Chimiche e Geologiche, Università di Modena e Reggio Emilia, Modena, Italy.

Corresponding author: Shiran Liu (hbhslsr@gmail.com), Andréa Tommasi (andrea.tommasi@umontpellier.fr)

Keywords:
Subcontinental mantle lithosphere
Crust-mantle coupling
Melt-rock interaction
Olivine crystal preferred orientation
Seismic anisotropy

Highlights:

- Mainly coarse-granular and porphyroclastic peridotites with [100](010) olivine textures
- Equilibrium temperatures consistent with a 80 km thick lithosphere in the Cenozoic
- Extensive annealing implies that deformation frozen in the shallow mantle is 100s Ma old
- Mantle fabric related to Neoproterozoic shear zones may partially explain SKS splitting
- Limited reworking of the lithospheric mantle during Cretaceous rifting

Abstract

We studied a suite of mantle xenoliths carried by Cenozoic volcanism in the Borborema Province, NE Brazil. These xenoliths sample a subcontinental lithospheric mantle affected by multiple continental convergence and rifting events since the Archean. Equilibrium temperatures indicate a rather hot geotherm, implying a ca. 80 km thick lithosphere. Most xenoliths have coarse-granular and coarse-porphyroclastic microstructures, recording variable degrees of annealing following deformation. The high annealing degree and equilibrated pyroxene shapes in coarse-granular peridotites equilibrated at ~900°C indicate that the last deformation event that affected these peridotites is several hundreds of Ma old. Coarse-porphyroclastic peridotites equilibrated at 950-1100°C probably record younger (Cretaceous?) deformation in the deep lithospheric mantle. In addition, a few xenoliths show fine-porphyroclastic microstructures and equilibrium temperatures ≥1200°C, which imply a recent deformation, probably related to the dykes that fed the Cenozoic volcanism. Chemical and microstructural evidence for reactive percolation of melts is widespread. Variation in textural and chemical equilibrium among samples implies multiple melt percolation events well spaced in time (from Neoproterozoic or older to Cenozoic). Crystal preferred orientations of olivine and pyroxenes point to deformation controlled by dislocation creep with dominant activation of the [100](010) and [001]{0kl} slip systems in olivine and pyroxenes for all microstructures. Comparison of xenoliths' seismic properties to SKS splitting data in the nearby RCBR station together with the equilibrated microstructures in the low-temperature xenoliths

point to coupled crust-mantle deformation in the Neoproterozoic (Brasiliano) continental-scale shear zones, which is still preserved in the shallow lithospheric mantle. This implies limited reworking of the lithospheric mantle in response to extension during the opening of the Equatorial Atlantic in the Cretaceous, which in the present sampling is restricted to the base of the lithosphere.

1. Introduction

Continental plates have long-lived histories. They are usually composed by crustal domains with varied tectonic ages. Tectonic reworking is a common feature in crustal exposures. Yet, major tectonic events such as convergence, collision, and rifting involve the entire plate, not only the crust. By consequence, large volumes of the subcontinental lithospheric mantle must have been affected by a succession of tectono-thermal events (cf. reviews in Tommasi and Vauchez, 2015; Vauchez et al., 2012). In addition, during orogenic events, the strain regime frequently changes across the belt, with contiguous domains accommodating transcurrent motions and others accommodating thrusting for instance. However, how the deformation is accommodated in the lithospheric mantle and the level of coupling between crust and mantle deformation during these major tectonic episodes are still matter of debate.

Comparison between SKS splitting data and crustal structures points to coherent kinematics, implying at least partial coupling between the crust and the mantle in many orogenic belts (Tikoff et al., 2004). As recognized since the early times of seismic anisotropy measurements (e.g., Vauchez et al., 1991), crust-mantle coupling is well documented beneath large-scale strike slip faults and transpressional belts, such as the San Andreas fault (Bonnin et al. 2012) or the Pyrenees, the Appalachians, and the neoproterozoic Ribeira-Aracuai belt of SE Brazil (cf. review in Vauchez et al., 2012). In contrast, in collisional domains submitted to large amounts of thickening, like the Alps and the Southern Tibet, or in active continental rifts, such as the East African rift system, polarization directions of fast split SKS or SKKS waves are usually parallel to the trend of the belts or rifts, but at high angle to the lineations marking flow directions in the ductile crust and to the slip directions in active faults (e.g., Barruol et al., 2011; Wu et al., 2015; Hammond et al., 2014). This suggests at least partial decoupling between the crust and lithospheric mantle (Tommasi et al., 1999).

However, seismic anisotropy data only offer indirect information on the present-day structure of the upper mantle. Moreover, unless a variety of methods based on waves with different incidence angles and propagation directions are employed, localizing vertically the source of the anisotropy remains difficult. Analysis of mantle xenoliths, which are mantle fragments (peridotite xenoliths) carried to the surface by volcanic episodes, allows for direct sampling of the lithospheric mantle. This sampling is imperfect: it is discontinuous, non-oriented, and focused along the magmatic conduits.

Nevertheless, the characterization of the microstructures and associated crystal preferred orientations, as well as of the chemical compositions and mineralogy of the mantle xenoliths, allows determining the relative deformation, annealing, and petrological (partial melting, reactive melt transport, solid-state reequilibration) history, even if no dating is possible. Coupling petrophysical analyses on mantle xenoliths to seismological data may allow better constraining the deformation history of the lithospheric mantle and hence discussing crust-mantle coupling during major tectonic events.

In this article, we present a petrostructural study of peridotite xenoliths entrained by Cenozoic volcanism in NE Brazil. Based on these data and on published SKS splitting measurements (Assumpção et al., 2011; Bastow et al., 2015), we try to unravel the tectono-thermal evolution of the continental lithospheric mantle in this region, which has been affected by multiple collisional and extensional episodes since the Archean. Analysis of the presently outcropping crustal structures highlights a series of tectono-magmatic episodes, among which the most important and recent ones are: (i) extensive intraplate deformation in a convergent setting, which produced a continental-scale system of strike-slip shear zones and transpressional belts accommodating lateral escape of this domain during the formation of the Gondwana and (ii) extension, localized in a series of intracontinental basins, during the early stages of the opening of the Equatorial Atlantic.

2. Geological and geophysical background

2.1 Evolution of the Northern Borborema Province (NBP)

The analysis of the crustal rocks outcropping in the Northern Borborema Province (NBP) points to a complex tectonic evolution, which probably started in the Archean, as indicated by U-Pb ages ranging from 3.4 to 2.7 Ga recorded in the São José Massif (Souza et al., 2016), ca. 100 km to the east of the study area and in smaller nuclei elsewhere in the province. Between 2.1-2.4 Ga, a major crust formation event produced ca. of the 50% of the present-day outcropping rocks (Hollanda et al., 2011; Souza et al., 2016). The tectonic setting for this extensive magmatic activity is discussed, but isotopic data indicates significant recycling of pre-existing crustal material (Hollanda et al., 2011).

The Meso- to Neoproterozoic evolution of the Borborema Province is characterized by a series of failed intracontinental rifting episodes. At 1.8-1.9 Ga, the Orós and Jaguaribe volcano-sedimentary basins formed to the west of the study area (Fig. 1). Localized extension was accompanied by intrusion of small volumes of alkaline granites and anorthosites elsewhere in the province, which extended until 1.75 Ga (Sa et al., 1995; Hollanda et al., 2011). At 1-0.9 Ga, extension affected the central Borborema Province (Santos et al., 2010; Van Schmus et al., 2008). The last Proterozoic extensional episode affected most of the province and formed the Seridó basin within the study area (Fig. 1).

The youngest sedimentation in this basin occurred at ~630-615 Ma, but early sedimentation may be as old as 1.8 Ga (Hollanda et al., 2015), suggesting an early rifting episode simultaneous with the formation of the Orós and Jaguaribe basins.

The major tectono-magmatic episode that affected the Borborema Province, shaping its present-day geology, is, however, the compressional Brasiliano event between 595-540 Ma (Neves, 2003; Archanjo et al. 2008; Viegas et al., 2014). This event resulted in extensive tectono-thermal reworking of the province through the formation of a continental-scale transcurrent shear zone system – the Borborema shear zone system, transpressional inversion of the Proterozoic metasedimentary basins, and widespread emplacement of granitoids (Fig. 1). The granitoids geochemistry indicates a dominant component of crustal reworking (Neves, 2003; Souza et al., 2016), implying an intraplate setting for the Brasiliano deformation, with a possible convergent plate boundary > 500 km to the NW from the study area (e.g., Caby et al., 1991; Ancelmi et al., 2015). The complex network of anastomosing E-W and NE-SW trending ductile dextral strike-slip shear zones, some up to ~25 km wide, and transpressional belts deformed under high temperature, low pressure conditions that compose the Borborema shear zone system (Vauchez et al., 1995) is therefore the expression of strain localization in an intraplate setting controlled by large-scale intraplate rheological heterogeneities (the basins) in response to the convergence between São Francisco, Amazonian, and West African cratons during the construction of the Gondwana (Tommasi et al., 1995). This shear zone system allowed for tectonic extrusion of the Borborema Province towards the NE (Ganade de Araújo et al., 2014, 2016), that is, towards the Saharan province, which, like Borborema, had been weakened by tectono-magmatic activity during the Meso- and Neoproterozoic.

In the early Cretaceous, the Borborema province experienced regional extension before rifting localized at the present location of the equatorial Atlantic Ocean (Darros de Matos, 1999). Structures associated with these early stages of rifting in the northern Borborema Province include several intracontinental basins or aborted rifts and a large tholeiitic dyke swarm. The basins formed as NW-SE trending asymmetric grabens (e.g., Potiguar, Rio do Peixe, Araripe in Fig. 1) controlled by reactivation of the Brasiliano shear zones (Darros de Matos, 1999; Castro et al., 2007, 2012; Marques et al., 2014). They contain dominantly continental sediments of fluviatile and lacustrine origin, which attain thicknesses of 2000 m, deposited between 145-125 Ma. The Potiguar basin is the best developed among these basins; its offshore domain is the only one involved in the final opening of the Atlantic. The Ceará-Mirim dyke swarm is a >350-km-long tholeiitic dyke swarm with a dominantly E-W trend that rotates to NE-SW at the southern termination of the Potiguar basin (Fig. 1). The dykes have ages between 135 Ma and 120 Ma (Hollanda et al, 2018 and references therein). Their emplacement is therefore synchronous to

the formation of the intracontinental basins. Geochemical data points to primary magmas formed by melting of an enriched mantle (EMI ± FOZO isotopic signatures) at shallow depths (<90 km; Ngonge et al., 2016).

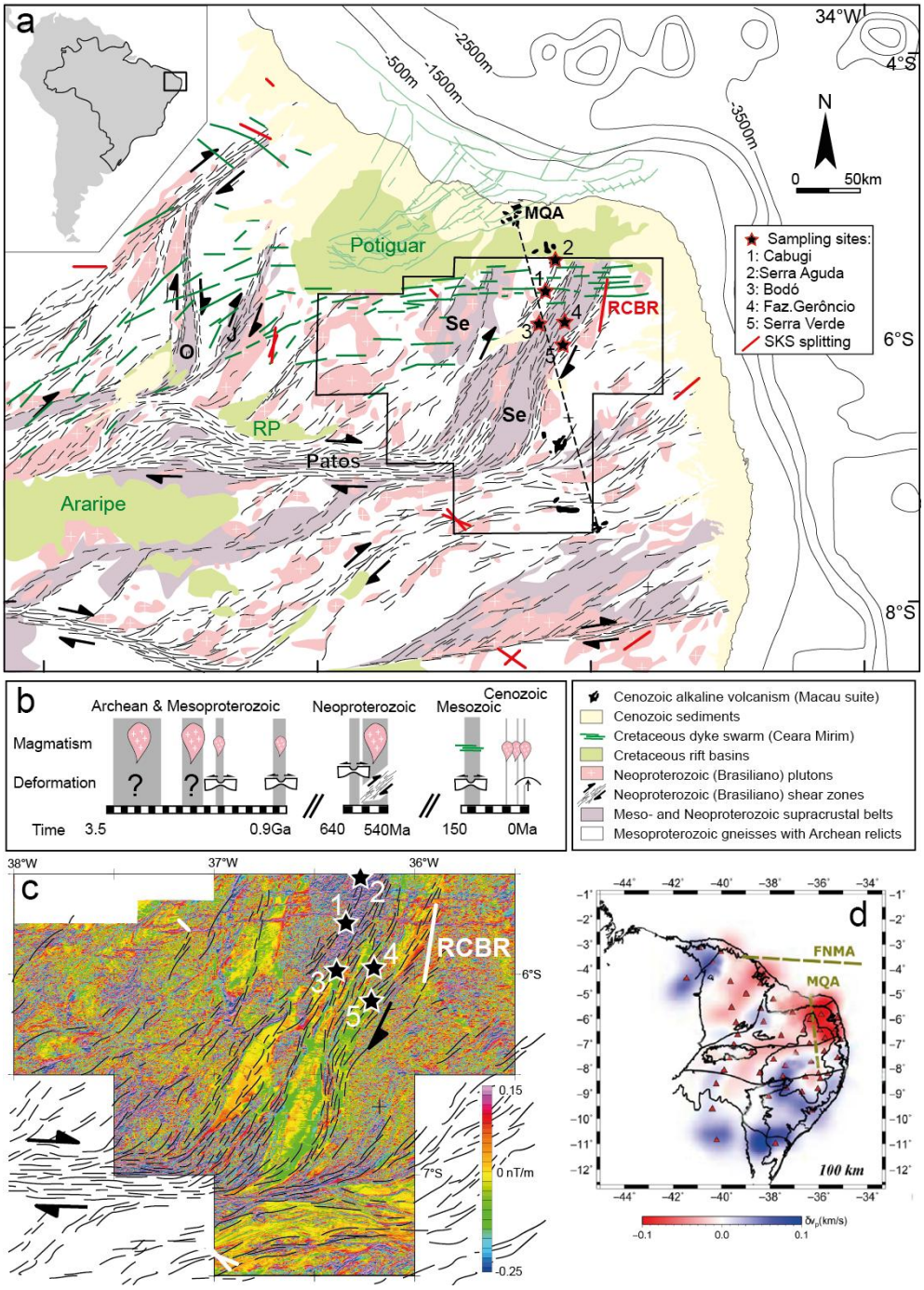

Fig. 1. (a) Simplified geological map (after Vauchez et al., 1995 and Oliveira and Medeiros, 2018) displaying xenolith sampling locations. (b) Time line of the major tectono-magmatic events in the Borborema Province. (c) Aeromagnetic anomalies map (1st vertical derivative; Costa et al., 2016) imaging middle crust structures in and around the Seridó belt. (d) P-wave tomography model for the Borborema Province at 100 km depth (Simões Neto et al., 2018) characterized by a marked low velocity anomaly east of the Macau-Queimadas volcanic alignment (MQA) and north of the Patos shear zone. SKS splitting data in (a) and (c) from Assumpção et al. (2011) and Bastow et al. (2015). RP: Rio do Peixe

Cretaceous basin. Se: Seridó, O:Orós, and J: Jaguaribe supracrustal belts.

The Cenozoic is characterized by a long-lived, but small-volume alkaline volcanism (both onshore and offshore), tectonic inversion of the Mesozoic intracontinental basins, and uplift of the Borborema Plateau. The entire Borborema Province sits nowadays on average at ~800m above the sea level and the Araripe basin is topographically more than 500 m above the Precambrian basement. Analysis of river profiles implies that most uplift occurred within the last 30 Ma (Tribaldos et al., 2017), but earlier events may have occurred (Marques et al., 2014; Nogueira et al., 2015). The present day crustal thickness of 30-35 km implies some degree of sub-lithospheric support for the uplift. The offshore Cenozoic volcanism forms an E-W volcanic alignment that extends from the Ceará coast in northeast Brazil (the Mecejana volcanic field) to the Fernando de Noronha archipelago. The Mecejana volcanics yield K-Ar ages between 26 and 44 Ma (Mizusaki et al., 2002), whereas volcanism in Fernando de Noronha has Ar-Ar ages between 12.5 and 6 Ma (Perlingeiro et al., 2013). The onshore Cenozoic volcanism is distributed along a N-S trend, forming the Macau–Queimadas Alignment (MQA, Fig. 1). Emplacement ages range between 52 Ma and 7 Ma, with two peaks around 26-29 Ma and 7-9 Ma and no clear age progression along the MQA (Souza et al., 2003; Silveira 2006; Knesel et al., 2011).

The Macau volcanics that entrained the studied mantle xenoliths (Fig. 1) erupted onto metasediments from the Neoproterozoic Seridó belt or Mesoproterozoic gneisses that form their basement. In the study area, the Brasiliano event is recorded by multiple NE-SW shear zones, which branch off from the E-W Patos shear zone in the south, by transpressional structures in the Seridó belt, and by intrusion of granitoids. The Cretaceous Ceará-Mirim dyke swarm crosscuts the study area with an E-W trend and the Potiguar basin outcrops to the north and west of it (Fig. 1).

2.2 Geophysical data

P-wave receiver functions, deep seismic refraction experiments, and surface-wave dispersion data indicate that the crust is 30 ~ 32km thick in the northern Borborema Province, but 36 ~ 38 km thick in the southern part of the province (Oliveira and Medeiros, 2012; Almeida et al., 2015; Lima et al., 2015; Luz et al., 2015). This variation in crustal thickness is consistent with gravity data (Oliveira and Medeiros, 2018) and correlated with topography: elevated regions show thicker crust. Receiver function data also imply an intra-crustal discontinuity at 9-18 depth, most often observed in domains with thinner crust, such as the area sampled by the studied xenoliths (Almeida et al., 2015).

Gravity and magnetic data illuminate the structuration of the deep crust in the Borborema province (Oliveira and Medeiros, 2018). These data establish the Patos, Pernambuco, and Jaguaribe shear zones as major structures, which splay of from the Transbrasiliano Lineament, separating four crustal blocks with different geophysical characteristics: the Southern, the Transversal,

the Ceará, and the Rio Grande do Norte domains. The studied xenoliths sample the mantle beneath the Rio Grande do Norte domain, which is delimited by the Jaguaribe and Patos shear zones to the west and south, and by the Atlantic Ocean to the north and east. This domain is characterized by strong magnetic contrasts with E-W or NNE trends, correlated with the outcropping Brasiliano structures (Fig. 1c). Magnetic anomalies also clearly define the Ceará-Mirim dykes (Fig. 1c). In addition, analysis of the Bouguer gravity anomaly shows that most of the Rio Grande do Norte domain is characterized by weak long wavelength positive anomalies, which follow the trend of the coastline (cf. Fig. 7 of Oliveira and Medeiros, 2018), suggesting that crustal thinning related to the Atlantic opening affected most of the domain.

The first kilometers of the lithospheric mantle structure may be probed by the analysis of Pn velocities, which decrease from 8.1 km/s to 7.9 km/s in a NW-SE refraction profile across the Borborema Province to the south of the study area (Lima et al., 2015). In the vicinity of the study area, Pn velocities are ~8.0 km/s, which for an isotropic mantle with a spinel-lherzolite composition would correspond to sub-Moho temperatures of 700-750°C (Schutt et al., 2018).

No seismic velocity data is available for the deeper sections of the lithospheric mantle, but a recent P-wave regional travel-time tomography model (Simões Neto et al., 2019) imaged slower than average velocities at depths <150 km in the northeastern Borborema province, just east of the study area (Fig. 1d). This low velocity anomaly coincides with a local geoid anomaly of +10 m (Ussami et al. 1999). Slower than average P-wave velocities in the shallow mantle beneath the study area are coherent with a rather shallow Lithosphere Asthenosphere boundary (LAB), estimated at 80 km depth based on S receiver function data from the station RCBR (Heit et al., 2007). The results of the regional P-wave tomography for the northeastern Borborema Province are also consistent with global finite-frequency tomography models, which image lower than average S-wave velocities in the mantle at 250-km depth in this region (French et al. 2013).

SKS splitting data in the Borborema Province (Bastow et al., 2015) show a complex pattern, with highly variable delay times and fast polarization directions, which in some places closely follow the Neoproterozoic crustal fabric, but are oblique to it in others (Fig. 1a,c). The station closest to the xenolith sampling sites, RCBR (Fig. 1a,c), shows a NNE-oriented fast S-wave polarization subparallel to the Brasiliano transpressive structures, which structure the northern Seridó belt and its gneissic basement, and a high delay time (1.9±0.2 s) based on 9 individual measurements (Assumpção et al., 2011).

2.3 Previous studies of Macau peridotite xenoliths

The petrology and the geochemistry of Macau mantle xenoliths were

studied by Comin-Chiaramonti et al. (1986), Princivalle et al. (1994), Fodor et al. (2002), Rivalenti et al. (2000; 2007). These studies identified two microstructural groups: protogranular (the dominant type) and (rare) porphyroclastic (partially recrystallized) peridotites. Protogranular microstructures are mainly observed in lherzolites, whereas porphyroclastic microstructures are usually observed in harzburgites. Protogranular peridotites also yield lower two-pyroxene equilibrium temperatures (825±116°C) than porphyroclastic ones (>1150°C). Trace-element patterns and isotopic compositions of the peridotites indicate variable degrees of metasomatism by alkali-basaltic melts with EMI and minor EMII isotopic signatures, probably during multiple metasomatic events (Rivalenti et al., 2000, 2007).

3. Methods

3.1. Sampling

We have studied 22 xenoliths from 5 different Macau volcanic sites, which extend in a rough N-S trend, from the limit of the Potiguar basin to ~70 km south of it (Fig. 1). Most xenoliths analyzed in the present study come from the Pico do Cabugi basaltic neck (5°42.3'S, 36°19.4'W). The Pico do Cabugi basalts yield Ar-Ar ages 24.6 ± 0.8 Ma (Souza et al., 2003 and references therein). Among the 16 xenoliths of the Pico do Cabugi in this study, 14 (marked as CA) have been collected by the authors in a field campaign in 2016 and two (marked as PC) were previously studied by Rivalenti et al. (2000).

We also analyzed 6 xenoliths previously studied by Rivalenti et al. (2007): two from the Serra Aguda neck (AG, 5°31'S, 36°17'W), ~30 km north of the Pico do Cabugi, at the border of the Potiguar basin (Fig. 1), one from the Serra Preta do Bodó dykes (BO, 5°58'S, 36°22'W), ~20 km south of Pico do Cabugi, and four from Fazenda Geroncio (GR, 5°58'S, 36°14'W) and Serra Verde localities (SV, 6°06'S, 36°12'W), located ~30 and ~50 km south of Pico do Cabugi (Fig. 1). There are no ages for the Fazenda Geroncio and Serra Verde volcanics, but the Serra Aguda basalts were dated at 26 Ma (Silveira, 2006) and those at Serra Preta do Bodó, at 7.1 Ma (Knesel et al, 2010).

Most xenoliths are small (on average 3 cm of diameter), but they are very fresh. The samples display no macroscopic evidence for major interaction with the host lava. However, small pockets of fine-grained clinopyroxene, spinel, and olivine, as well as melt films along grain boundaries were observed under the microscope, in particular close to the borders of many xenoliths. In addition, some xenoliths have pyroxenes with spongy borders, indicative of limited partial melting during extraction. These domains were carefully avoided during microprobe analyses. They were sometimes included in the EBSD analyses, but affect weakly the results because of their small area.

3.1 Electron-backscattered diffraction (EBSD) data acquisition and treatment

Petrostructural analyses were performed on all samples. Crystallographic preferred orientations (CPOs) of olivine, pyroxenes, and spinel were measured

by indexing of electron-backscattered diffraction patterns in the SEM-EBSD facility at Geosciences Montpellier, France. Data acquisition was performed using a JEOL JSM 5600 scanning electron microscope with 17kV acceleration voltage and 24mm working distance. We performed EBSD mapping over the entire thin section (areas ≥ 2x3 cm^2) with step sizes between 14µm and 35 µm, depending on grain size. Indexation rates varied between 84% and 97%. Non-indexed points correspond mainly to fractures. During post-acquisition data treatment, we eliminated inaccurate indexing points (MAD > 1.3° and wild spikes), corrected for rare olivine pseudo-symmetry misindexing, and filled up non-indexed pixels with at least 6 coherent neighboring measurements with the average of the neighbors' orientations.

The CPO data analysis, that is, the calculation of the orientation distribution functions (ODF) and of the misorientations, the computation of the strength and symmetry of the olivine CPO, the plotting of pole figures, and the quantification of the microstructure (grains' size, shape, and orientation) was performed using the MTEX toolbox in Matlab (http://mtex-toolbox.github.io/; Hielscher and Schaeben, 2008; Bachmann et al., 2010; Bachmann et al., 2011). The ODFs were calculated using a "de la Vallée Poussin" kernel function with a half-width of 10°. The CPO is presented as one crystallographic orientation per pixel in pole figures (lower hemispheric stereographic projections). Thin sections were cut in random orientations, because of the small size of the xenoliths. To facilitate comparison between samples, we rotated the CPO of all samples into a common reference frame, in which the maximum concentration of [100] of olivine is parallel to the E-W direction and the maximum concentration of [010] axis of olivine is parallel to the N-S direction of the pole figure. The choice of this reference frame can be justified a-posteriori by the analysis of the CPO, which indicates that this reference frame probably corresponds to the lineation and normal to the foliation directions (cf. discussion).

The strength of the CPO was quantified using the dimensionless J-index (Bunge, 1982). The J-index for a random CPO is 1; it can reach up to 20 in natural peridotites, with a peak at 3-5 (Tommasi and Vauchez, 2015). We use the dimensionless BA-index, based on the eigenvalues of the [100] and [010] axes orientation distributions (Mainprice et al., 2014), to characterize the olivine CPO symmetry. This index allows classifying the olivine CPO into three types: (i) fiber-[010], characterized by a [010] point maxima and girdle distributions of [100] and [001] (BA-index < 0.35), (ii) orthorhombic, characterized by point maxima of [100], [010], and [001] (0.35 < BA-index < 0.65) and (iii) fiber-[100], characterized by a point maxima of [010] and girdle distributions of [010] and [001] (BA-index > 0.65). J- and BA-indexes do not depend on the reference frame.

To analyze quantitatively the microstructure, we used the grain detection method in MTEX (Bachmann et al., 2011) defining grains boundaries by misorientation angles between adjacent pixels higher than 15°. Grains

composed by less than 10 pixels were not considered in the microstructural analysis. The misorientation of each pixel relative to the mean orientation of the grain (M2M) and the grain orientation spread (GOS) were calculated to quantify the intracrystalline orientation gradients, which are a proxy of the dislocation density. In addition, we characterized the sinuosity of the grain boundaries by the shape factor, which is the ratio of the perimeter of the grain over the perimeter of a circle with the same area. Both the intra-granular misorientation (M2M and GOS) and the sinuosity of grain boundaries (shape factor) should decrease in response to recrystallization.

3.2 Mineral compositions and equilibrium temperatures

Mineral compositions of olivine, orthopyroxene, clinopyroxene, and spinel were analyzed in ten samples, selected based on their microstructure, so that all microstructural types were represented. Measurements were performed in a Cameca SX100 electron microprobe at the Microsonde Sud facility at the University of Montpellier, France at a 20kV accelerating voltage and a 10nA current. For each sample, we analyzed both rim and core composition in 3 to 4 grains for olivine, orthopyroxene, clinopyroxene, and spinel.

We calculated equilibrium temperatures based on the clinopyroxene-orthopyroxene geothermometer (Taylor, 1998) and on the Ca-in-opx geothermometer (Brey and Kohler, 1990; revised by Nimis and Grutter, 2010). Average rim and core equilibrium temperatures were calculated by averaging the temperatures calculated using 3-4 rim or core compositions of individual opx grains or opx-cpx pairs for each sample. Since no reliable barometers are available for spinel-facies peridotites, we chose arbitrarily 1.5 GPa (~46 km depth) as the pressure to calculate the two thermometers. Changes in the assumed pressure produce a variation of ~10 °C per 0.5 GPa (~11 km).

3.3 Seismic properties

Seismic properties of each sample were computed using the MTEX toolbox (Mainprice et al., 2011), using Voigt-Reuss-Hill averaging based on the CPOs and modal content of olivine, orthopyroxene, and clinopyroxene derived from the EBSD maps and on the single crystal elastic constant tensors of the three minerals and their temperature and pressure derivatives (Abramson et al., 1997; Anderson et al., 1992; Chai et al., 1997; Isaak et al., 2006; Jackson et al., 2007; Sang and Bass, 2014). Average seismic properties for the lithospheric mantle beneath the study area were estimated by averaging the elastic constant tensors of all samples with all CPO data rotated into a common reference frame. The assumption is that the orientation of the lineation and foliation is constant both laterally and vertically. The average seismic properties provide therefore an estimate of the maximum seismic anisotropy that could be produced, if the xenolith sampling is representative of the variability of compositions and CPO in the lithospheric mantle beneath the

studied area.

4. Data

4.1 Microstructures

Previous studies (Fodor et al., 2002; Rivalenti et al., 2000; Rivalenti et al., 2007) have correlated optical observations of the microstructures with chemical compositions and equilibrium temperatures to divide the Macau peridotite xenoliths into two groups: protogranular and porphyroclastic. In the present study, we associated to the optical observations quantitative analysis of the microstructural data derived from EBSD mapping. Based on these data, in particular the intragranular misorientation of olivine and the olivine and orthopyroxene grain shapes (Fig. 2), we classify the Macau peridotites into three microstructural groups (Table 1): coarse-granular (6), coarse-porphyroclastic (12), and fine-porphyroclastic (4). The coarse-granular and coarse-porphyroclastic groups correspond to a continuous variation in microstructure (Figs. 2 and 3). They were described as protogranular in the previous studies. The fine-porphyroclastic group is clearly different from the other two groups (Figs. 2 and 3); it was described as porphyroclastic in the previous studies.

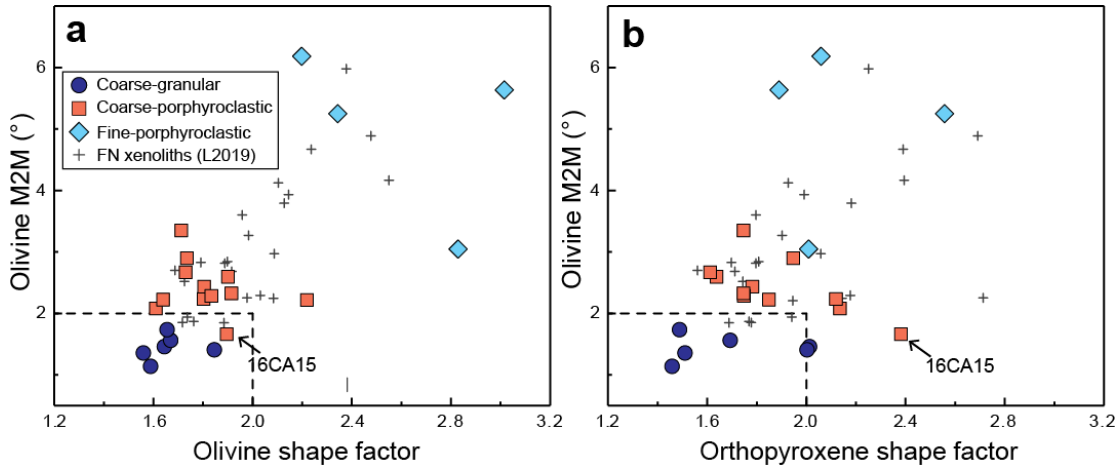

Fig. 2. Microstructural parameters calculated from EBSD data: (a) Olivine shape factor vs. intragranular misorientation relative to the mean orientation of the grain (M2M); (b) Orthopyroxene shape factor vs. olivine M2M. All quantities are average values at the sample scale weighted by the grains' area (cf. Table 2). Similar data for Fernando de Noronha (FN) xenoliths, which sample an old domain of the equatorial Atlantic (Liu et al., 2019), are presented for comparison.

There is no relation between microstructure and sampling site. All three microstructures are represented among the Pico do Cabugi peridotites, which is the best-sampled site in the present study, and in at least one of the other sampling localities (Table 1). This observation is corroborated by the previous studies, which analyzed a larger number of peridotite xenoliths from other Macau volcanic centers (Fodor et al. 2002; Rivalenti et al. 2007). Coarse

granular and coarse porphyroclastic microstructures predominate in all sites. Fine-porphyroclastic peridotites are always minor. They were only recovered in three sites, which are nevertheless >60 km apart (Fig. 1): Serra Aguda, Cabugi, and Serrote Preto (a small plug ca. 30 km to the SSE of Pico do Cabugi, Fodor et al. 2002).

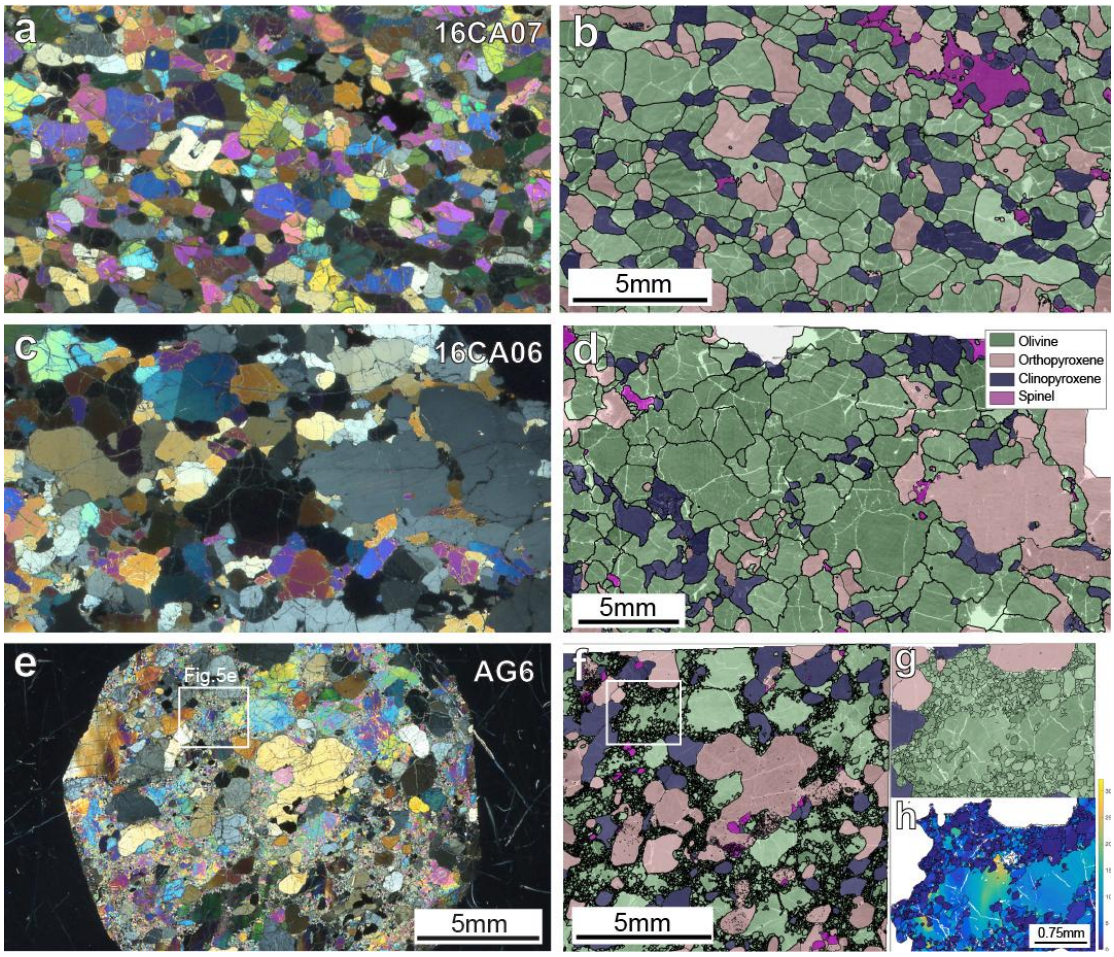

Fig. 3. Typical microstructures of Macau peridotite xenoliths: (a-b) coarse-granular, (c-d) coarse-porphyroclastic, and (e-f) fine-porphyroclastic. (a,c,e) Photomicrographs in cross-polarized light; scale bar is the same in all photomicrographs. (b,d,f,g) EBSD phase maps, which better illustrate the variation in shape of olivine and pyroxenes between the three microstructures. (g) Detail of a partially recrystallized domain in fine-porphyroclastic lherzolite AG6. (h) Misorientation relative to the mean orientation of the grain (M2M) map illustrating the difference in intragranular misorientation in olivine between porphyroclasts (high M2M) and neoblasts (low M2M) in the same domain.

Coarse-granular peridotites are characterized by roughly equigranular microstructures (Fig. 3a-b). Olivine and orthopyroxene pyroxene grains are on average 1-3 mm, clinopyroxene slightly smaller: 0.8-1 mm (Table 2). Both olivine and pyroxenes have curvilinear to straight grain boundaries, evolving locally into polygonal shapes with 120° triple junctions (Fig. 4a), and very low densities of intracrystalline deformation features, such as undulose extinction, subgrains, or kinks (Fig. 3a and 4a). Quantitatively, these observations

translate into low shape factors ≤ 1.85 for olivine and ≤ 2 for orthopyroxene and into low M2M values ≤ 2° for olivine (Fig. 2). Lherzolite 16CA14 has an intermediate microstructure characterized by polygonal olivine grains, but pyroxenes with irregular shapes (Figs. 2 and 4b). Most coarse-granular peridotites display a weak olivine shape-preferred orientation (SPO) (Fig. 3a), but BO09 has higher olivine aspect ratios (Table 2) and a clear olivine SPO, which results in a tabular microstructure. Pyroxene grains usually show no exsolutions (Fig. 3a and 4a-b). Spinel grains have holy-leaf or interstitial shapes. Coarse holy-leaf spinels may contain rounded inclusions of olivine or pyroxenes (Fig. 3b).

Coarse-porphyroclastic microstructures are characterized by variable grain sizes. In most cases, the grain size variation is continuous and it is difficult to discriminate between porphyroclasts and neoblasts (Fig. 3c-d). Olivine has more irregular grain shapes and clear evidence for intracrystalline plastic deformation (Fig. 3c-d and 4c). Olivine grains have shape factors between 1.6 and 2.2, consistently with the more sinuous grain boundaries, and higher M2M values ranging from 2° to 3.4° (except 16CA15), consistent with the higher frequency of undulose extinction and subgrain boundaries (Fig. 2). Orthopyroxene grains also have irregular shapes (Fig. 3c-d and 4c-d), which are associated with shape factors from 1.6 to 2.4 (Fig. 2b). Orthopyroxene grain boundaries often show embayments or cuspate shapes at the contact with olivine grains (Fig. 4c-d). Clinopyroxene grains also show irregular or interstitial shapes (Fig. 3c-d). In some samples, orthopyroxene grains display exsolutions (Fig. 3c). Undulose extinction and kinks are observed locally. Spinel usually has irregular shapes and occurs in association with ortho- or clinopyroxene (Fig. 3d).

Fine-porphyroclastic peridotites show a well-developed bimodal olivine grain size distribution, characterized by coexistence of coarse porphyroclasts with serrated grain boundaries, undulose extinction, and closely-spaced subgrain boundaries with a recrystallized matrix composed by polygonal olivine neoblasts free of intracrystalline deformation (Figs. 3e-h and 4e-f). The average size of the recrystallized grains varies between samples (Table 2): it is ~100 µm in AG6 (Fig. 4e), but >300 µm in the other fine-porphyroclastic peridotites (Fig. 4f, Table 2). It is noteworthy that the recrystallized olivine grains are not organized in a planar mode, marking a foliation, but either form irregular pockets or vein-like structures (Fig. 3e-f). Orthopyroxene is usually coarser than clinopyroxene (Fig. 3f). Exsolutions were not observed in this group. Shape factors of orthopyroxene vary between 1.89 and 2.56 (Fig. 2). In AG6 and AG7, pyroxenes have rounded shapes (Fig. 3f), whereas in PC105 and PC109 fine-porphyroclastic samples, pyroxenes have irregular shapes, with cusp-like terminations when in contact with olivine, similarly to pyroxenes in coarse-porphyroclastic peridotites. Spinel occurs as fine rounded grains (Fig. 3f).

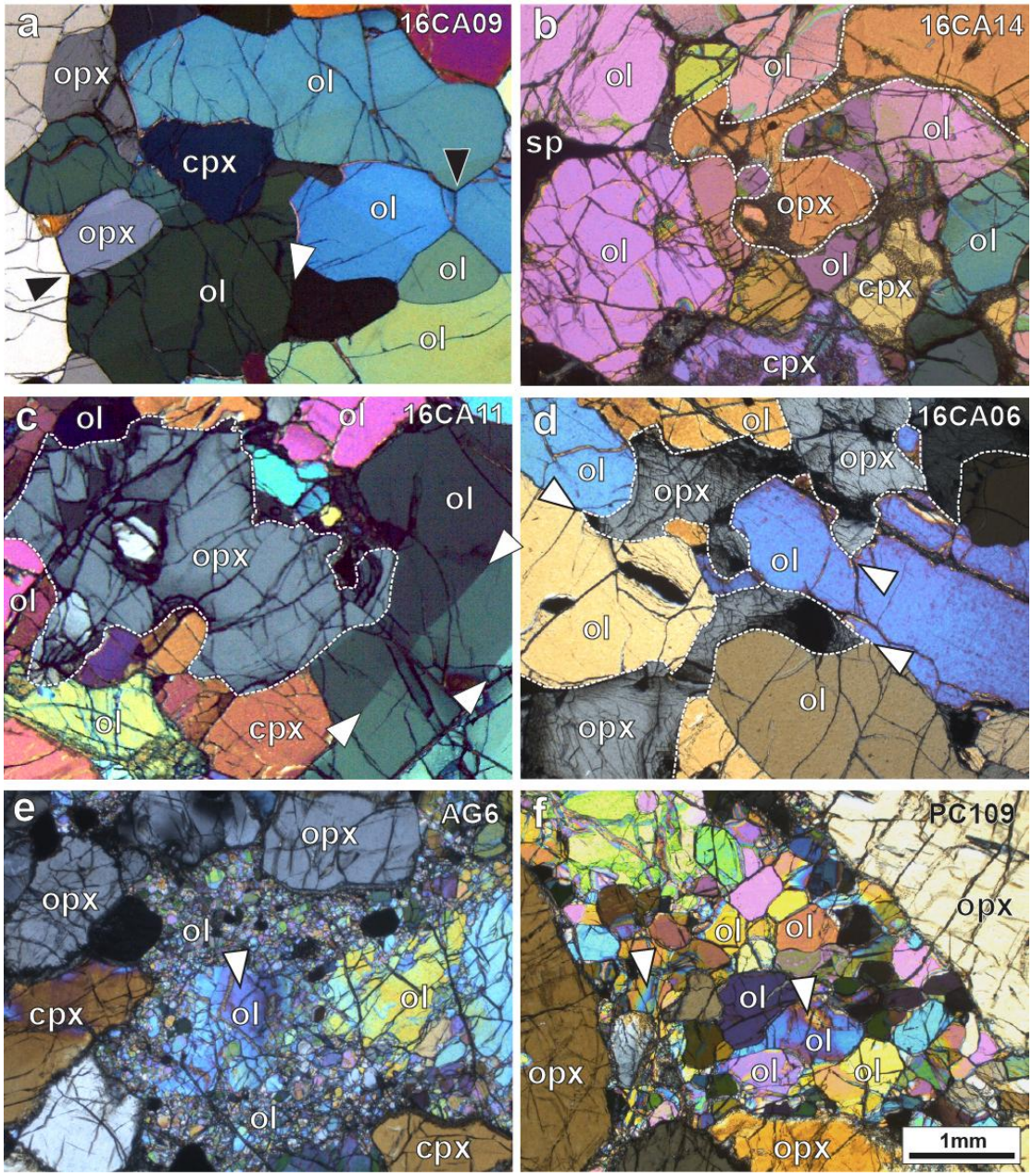

Fig. 4. Photomicrographs in cross-polarized light displaying typical features for the three microstructural groups. (a) Coarse granular lherzolite displaying polygonal grains (black arrow marks a 120° triple junction) almost free of intracrystalline deformation features, white arrow indicates a relict subgrain boundary in olivine (ol); (b) Coarse granular lherzolite 16CA14 displaying polygonal strain-free olivine grains, but irregularly-shaped orthopyroxene (opx) grains (highlighted by dashed line). (c-d) Coarse porphyroclastic lherzolites 16CA11 and 16CA06 showing irregularly shaped olivine, orthopyroxene (highlighted by dashed line), and clinopyroxene (cpx) grains with interpenetrating interphase boundaries, white arrows indicate subgrain boundaries in ol in (c) and mark cusp shaped opx in contact with ol in (d); (e) Fine-porphyroclastic lherzolite AG6 showing a matrix of very fine recrystallized olivine neoblasts surrounding a coarse olivine porphyroclast with ondulose extinction and subgrains (white arrow); (f) Fine-porphyroclastic harzburgite PC109 showing tabular, strain-free olivine neoblasts as well as relicts of olivine porphyroclasts with undulose extinction (white arrow) within a strongly recrystallized domain between opx porphyroclasts. Scale bar is the same in all photomicrographs.

4.2 Crystallographic preferred orientations (CPO)

Quantitative data on the intensity and symmetry of the olivine CPO (J- and BA-indexes) as well as pole figures of the olivine, orthopyroxene, and clinopyroxene CPOs for all studied samples are presented in Figs. 5 and 6 and Table 2. For the samples in which a foliation was observed, the latter is displayed on the pole figures (Fig. 6). In these samples, the olivine [010] maximum is normal to the foliation.

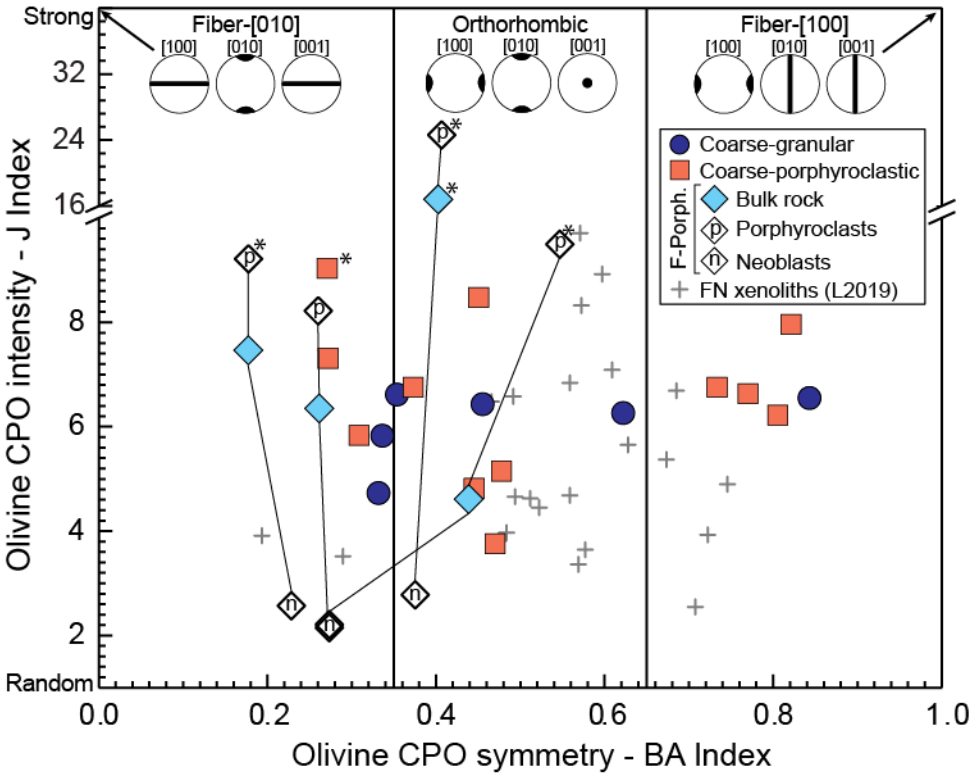

Fig. 5. Olivine CPO symmetry (BA-index) vs. CPO strength (J-index). The variation in olivine CPO pattern as a function of BA-index is illustrated at the top of the diagram. For fine-porphyroclastic peridotites, we present data for the bulk rock and for porphyroclasts and neoblasts separately. Values are presented in Table 2. * indicates J-indexes that are probably overestimated, because <100 grains could be analyzed in the thin section. CPO data for Fernando de Noronha (FN) xenoliths (Liu et al., 2019) are displayed for comparison.

Olivine has moderate to strong CPO (Figs. 5 and 6). With exception of harzburgite AG7, which has a very high J-index of 16.6 due to a few coarse olivine porphyroclasts that occupy most of the thin section, the J-index varies between 3.8 and 8.5, with a mean of 6.4. The CPO symmetry varies between fiber-[010], orthorhombic, and fiber-[100] patterns. Fine-porphyroclastic peridotites display olivine CPO patterns intermediate between fiber-[010] and orthorhombic and the neoblasts have systematically weaker olivine CPO (Figs. 5 and 6a). There is no systematic variation of J-index or BA-index within the two other microstructural groups. Coarse-granular samples display dominantly orthorhombic olivine CPO patterns with J-indexes around 6 (Figs. 5 and 6a). Coarse-porphyroclastic samples have more variable CPO patterns and

intensities (Fig. 5). Four coarse-porphyroclastic harzburgites (16CA01, 16CA02, 16CA03, and 16CA18) have strong CPO with fiber-[100] patterns (Fig. 6b). The remainder coarse-porphyroclastic peridotites display variable CPO intensity orthorhombic patterns with a tendency towards fiber-[010], expressed as girdle of [100] with a maximum within it and a point maximum of [010] (Fig. 6b).

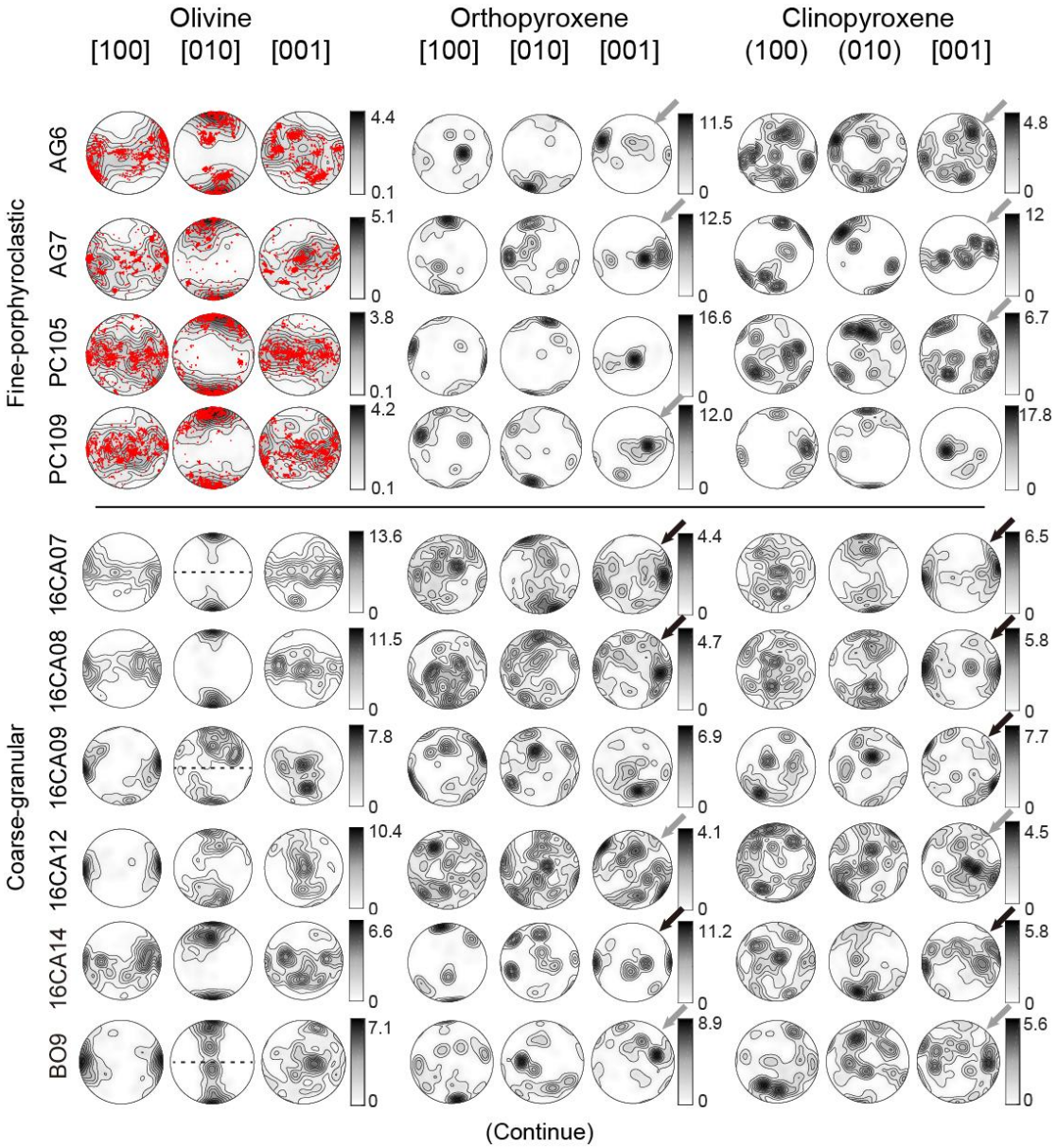

Fig. 6. Crystal preferred orientations (CPO) of olivine, orthopyroxene, and clinopyroxene for all studied fine-porphyroclastic and coarse-granular peridotites and coarse-porphyroclastic peridotites. Lower hemisphere stereographic projections with contours at 1 multiple of a uniform distribution intervals. The three pole figures for each mineral are plotted using the same gray scale. For the fine-porphyroclastic peridotites, the CPO of olivine porphyroclasts is presented as points and the CPO of olivine neoblasts is presented as contours. Black arrows indicate pyroxene CPO that are well correlated with the olivine CPO and gray arrows indicate those partially correlated. When the sample shows a olivine shape preferred orientation marking a foliation, the latter is displayed as a dashed

line in the olivine [010] pole figure.

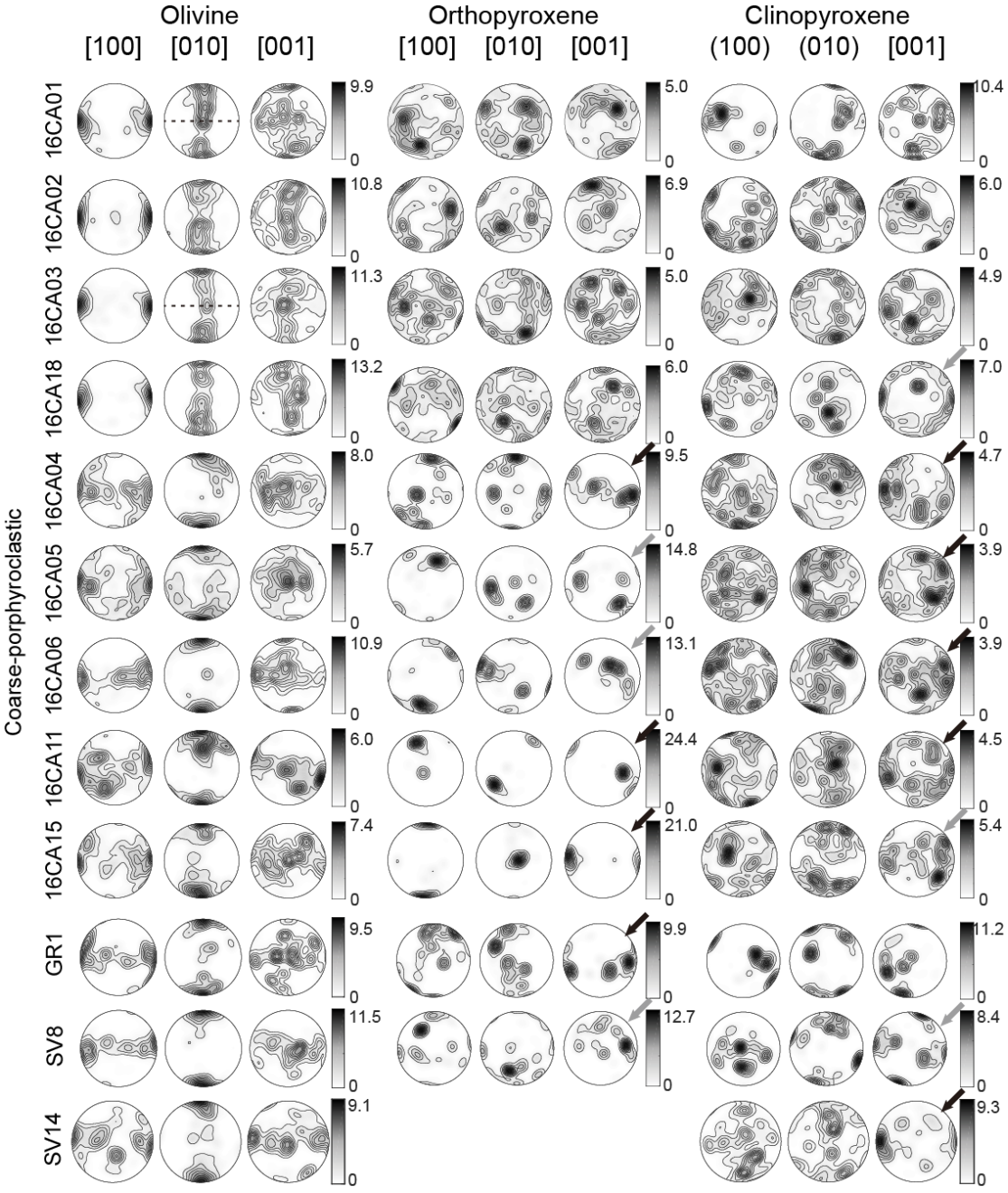

Orthopyroxene CPO is consistent with the olivine CPO in the majority of the studied peridotites. It is characterized by $[001]_{opx}$ and $[100]_{opx}$ (or $[010]_{opx}$) maxima parallel to the $[100]_{ol}$ and $[010]_{ol}$ maxima, respectively, suggesting a common deformation history (arrows in Fig. 6). However, coarse-porphyroclastic harzburgites 16CA01, 16CA02, 16CA03, 16CA18 and coarse-granular lherzolite 16CA09 show weak orthopyroxene CPO that are not consistent with the olivine CPO, characterized by a weak $[001]_{opx}$ maximum at high angle to a well-developed $[100]_{ol}$ maximum.

Clinopyroxene shows more dispersed CPO, but which are, in many samples, consistent with both olivine and orthopyroxene CPO patterns,

characterized by $[001]_{cpx}$ and $[010]_{cpx}$ maxima subparallel to $[100]_{ol}$ and $[010]_{ol}$ maxima (arrows in Fig. 6). However, in most fine-porphyroclastic peridotites and in coarse-granular lherzolite 16CA12, although the orthopyroxene CPO is consistent with the olivine CPO, the clinopyroxene CPO is not. In coarse-porphyroclastic harzburgites (16CA01, 16CA02, 16CA03, 16CA18) neither the orthopyroxene nor the clinopyroxene CPO are correlated with the olivine CPO.

4.3 Modal compositions

Modal compositions were determined based on the area fraction of each mineral in the EBSD maps (Fig. 7 and Table 1). All samples are spinel-facies peridotites. Lherzolites predominate (14/22), but the sampling also includes 7 harzburgites and 1 wehrlite. Predominance of fertile peridotites with no dependence on sampling site was also observed in previous sampling of Macau xenoliths by Rivalenti et al. (2000, 2007; Fig. 7).

The compositions of the two microstructural groups overlap, but coarse-granular peridotites are on average more fertile (ol contents of 57-70%) than coarse-porphyroclastic peridotites (ol contents between 67-87%, with one outlier – 16CA04, which has 59% of olivine and an intermediate microstructure). Fine-porphyroclastic peridotites display variable olivine contents overlapping with the two other groups.

Comparison of the modal compositions to those predicted by various partial melting models highlights that roughly half of the studied Macau xenoliths are enriched in clinopyroxene or olivine relatively to the models' predictions (Fig. 7). Even for those samples plotting along the partial melting trends, a large variability in partial melting degrees, from 1-20% melting, has to be invoked to explain the full range of observed modal compositions. Such a variation in partial melting is difficult to reconcile within the limited volume of the mantle sampled by these volcanic eruptions. This suggests reactive melt percolation leading to either crystallization of clinopyroxene and/or orthopyroxene at the expenses of olivine (refertilization processes, e.g. Le Roux et al., 2007; represented by gray arrows in Fig. 7) or crystallization of olivine at the expense of pyroxenes (dunitization processes, e.g., Berger and Vannier, 1984; Kelemen, 1990; black arrows in Fig. 7). The observed deviations in modal compositions relatively to partial melting trends are consistent with microstructural evidence for reactive melt percolation, such as the sinuous olivine-pyroxene boundaries and the cusp-like shapes of pyroxenes when in contact with two olivine grains (cf. Figs. 3 and 4).

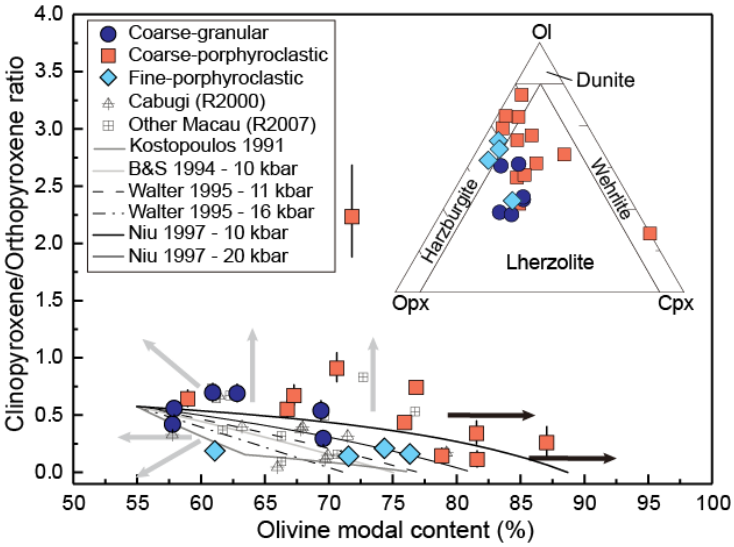

Fig. 7. Modal compositions of the studied peridotites presented as clinopyroxene/orthopyroxene ratio vs. olivine modal content and as the traditional ol-opx-cpx ternary diagram (insert). Modal compositions of Cabugi and other Macau volcanics peridotite xenoliths studied by Rivalenti et al. (2000) and (2007) are plotted for comparison. Black and gray curves represent the evolution of the modal composition predicted by different partial melting models for an initial fertile modal composition of 55% ol, 28.5% opx, and 16.5% cpx (Baker and Stolper, 1994; Kostopoulos, 1991; Niu, 1997; Walter et al., 1995). Gray arrows indicate evolution trends associated with cpx and/or opx crystallization at the expense of ol (refertilization reactions). Black arrow indicates evolution trends associated with ol crystallization at the expense of pyroxenes (dunitization reactions).

4.4. Mineral compositions

The chemical compositions of main mineral phases in the studied Macau peridotite xenoliths are listed in Supplementary Material Table S1. Representative results are displayed in Fig. 8 together with previous data for Macau peridotite xenoliths (Supplementary Material Table S2). Comparison between the present and previous datasets indicates that our sampling is representative of the variability in composition for these localities. Analysis of the present dataset indicates that there is no simple correlation between microstructural types and chemical compositions (Fig. 8). There is also no relation between mineral chemistry and sampling locality.

The Mg# number [Mg# = 100×Mg/(Fe + Mg), atomic ratio] of olivine, orthopyroxene, and clinopyroxene ranges between 89.1 – 91.6 (average 90.0), 89.1 - 91.7 (average 90.4), and 87.9 – 92 (average 90.9), respectively (Figs. 8a,b). Core-rim variations in Mg# are weak for all three minerals in most samples. Olivine and orthopyroxene Mg# within each sample show low dispersion and are positively correlated, with the orthopyroxene being slightly enriched in Mg relatively to olivine (all data points, except fine-porphyroclastic peridotites AG6 and AG7, plot slightly above the 1:1 line in Fig. 8b). Clinopyroxene Mg# shows much higher variability at the sample scale, in particular within coarse-porphyroclastic harzburgites, indicating chemical disequilibrium at the mm-scale. Moreover, average clinopyroxene Mg# in

neither cores nor rims does not display a simple correlation with the olivine Mg# (Fig. 8a). Most measured Mg# spread between the 1:1 and the Fe-Mg partition trend between olivine, clinopyroxene, and melt in oceanic troctolites (Lissenberg and Dick 2008), but fine-porphyroclastic peridotites AG6 and AG7 have clinopyroxenes enriched in Fe relatively to olivine.

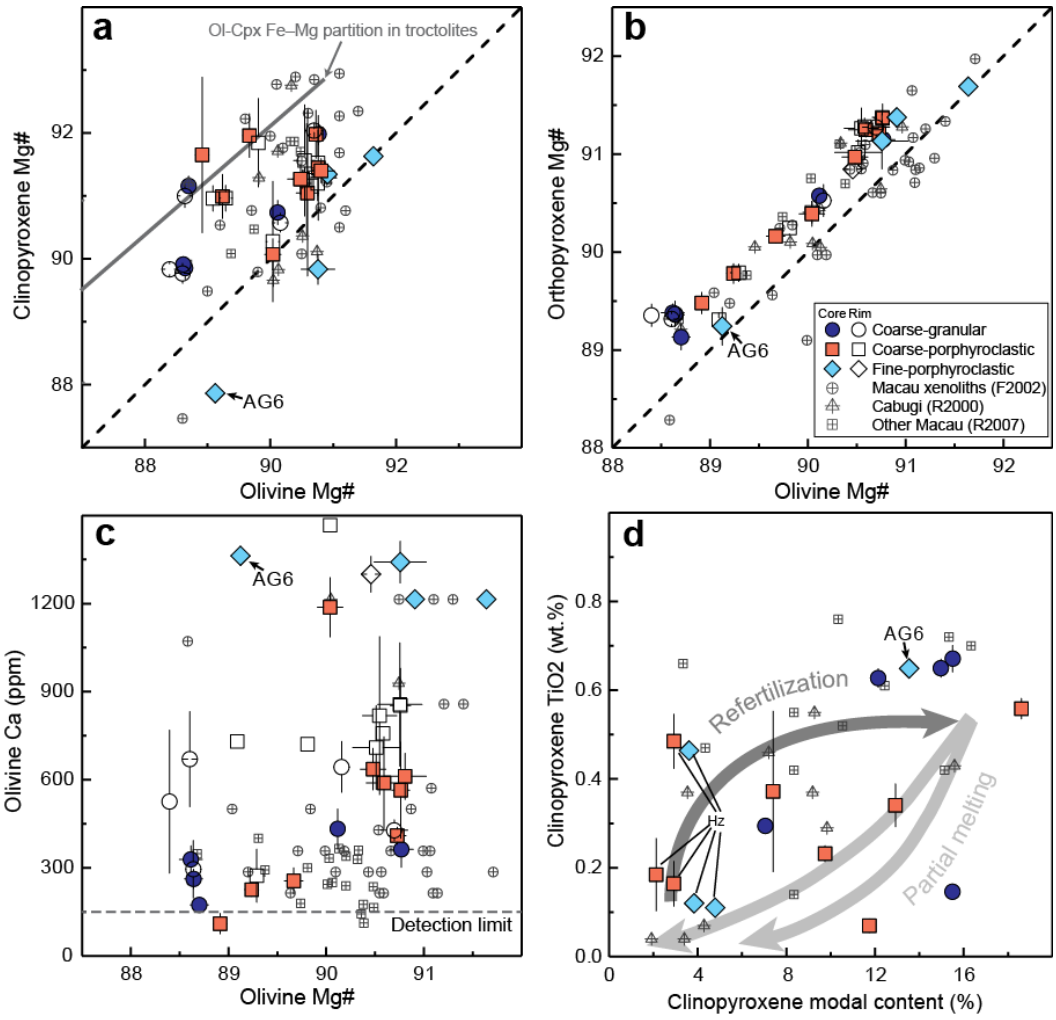

Fig. 8. Chemical compositions for major rock-forming minerals: (a-c) Clinopyroxene Mg#, orthopyroxene Mg#, and olivine Ca content (ppm) vs. olivine Mg#, (d) Clinopyroxene TiO2 content (wt.%) vs. modal content (%). Minerals chemical compositions for Macau peridotite xenoliths previously studied by Rivalenti et al. (2000), (2007), and Fodor et al. (2002) are plotted for comparison. The value of the depleted mantle (DM) from Workman and Hart (2005) is displayed in (a) and (b). Fe-Mg partition between olivine and clinopyroxenes in troctolites (Lissenberg and Dick, 2008) is plotted in (a). Partial melting and refertilization trends proposed by Le Roux et al. (2007) are plotted in (d). Hollow symbols represent rim compositions and solid symbols represent core ones. Error bars represent the chemical variation at the sample scale. Data is presented in Supplementary Material Table S1.

Olivine cores show low Ca contents with a weak positive correlation with Mg#, (Fig. 8c), except for the fine-porphyroclastic peridotites and the coarse-porphyroclastic lherzolite GR1, which have high Ca contents. Olivine rims in all studied peridotites are enriched in Ca and show a high variability at

687 the thin section (mm-cm) scale.
688 Clinopyroxene TiO_2 contents (wt.%) do not show the simple positive
689 correlation with cpx modal content (%) expected if partial melting controlled the
690 chemistry of the peridotites (Fig. 8d). Among the harzburgites, four have
691 Ti-poor clinopyroxene grains (TiO_2 contents < 0.2%), while the other two have
692 clinopyroxene grains with TiO_2 contents of 0.55%. All harzburgites show
693 marked variability in the Ti-content of clinopyroxene at the sample scale,
694 indicating disequilibrium. Half of the lherzolites have clinopyroxenes with
695 almost constant TiO_2 contents between 0.55-0.65%, independently of the
696 clinopyroxene modal content. The remaining lherzolites have rather Ti-poor
697 clinopyroxene grains.
698 Spinel Cr# [Cr# = 100×Cr/(Cr+Al) and Mg# contents correlate with the
699 modal composition. Harzburgites have spinel with Cr# ranging between
700 40-57.5 and Mg# ranging between 61-72, whereas lherzolites have spinel with
701 Cr# between 8-20 and Mg# between 73-84 (Supplementary Material Fig. S1a).
702 Yet, the lherzolites show a clear enrichment in Mg in spinel relatively to a
703 typical depleted mantle composition. Fine-porphyroclastic lherzolite AG6 has
704 the highest spinel Mg# (83) and lowest Cr# (11). TiO_2 contents (wt. %) in spinel
705 are low (≤0.18%) in most lherzolites (Supplementary Material Fig. S1b). In
706 contrast, spinel in coarse-porphyroclastic harzburgites and lherzolite GR1 has
707 a wide range of average TiO_2 contents, which may reach 1.03%, with strong
708 variations within each sample, indicating disequilibrium. Spinel in
709 fine-porphyroclastic lherzolite AG6 also has a fairly high TiO_2 content of 0.45%.
710
711 *4.5. Equilibrium temperatures and geotherm estimation*
712 Most equilibrium temperatures determined using two-pyroxenes
713 geothermometer of Taylor (1998; TTA98) and the Ca in orthopyroxene
714 (Ca-in-opx) of Brey and Kohler (1990) revised by Nimis and Grutter (2010)
715 agree within ±70 °C (gray dashed lines in Fig. 9). This suggests that they are
716 reliable. However, peridotites with cpx-opx temperatures < 800 °C show larger
717 discrepancies (>90 °C), with systematically higher Ca-in-opx equilibrium
718 temperatures. This inconsistency between the predictions of the two
719 thermometers is observed for both core and rim temperatures and is not
720 correlated with the microstructure. It affects two coarse-porphyroclastic
721 peridotites (16CA06, 16CA11) and one coarse-granular lherzolite (16CA14).
722 The latter has the lowest temperature among all samples with strong
723 inconsistency between the predictions of the two thermometers (592°C and
724 790°C, Table 1).
725 Following Nimis and Grutter (2010), we use the temperature predictions
726 of TTA98 thermometer as the equilibrium temperatures. All
727 fine-porphyroclastic peridotites and the coarse-porphyroclastic peridotite GR1
728 have high equilibrium temperatures over 1200 °C. Coarse-porphyroclastic
729 peridotites have two ranges of equilibrium temperatures: harzburgites
730 (16CA01, 16CA03, 16CA18) as well as clinopyroxene-poor lherzolite SV8

have equilibrium temperatures between 900 and 1100 °C, whereas the clinopyroxene-rich coarse-porphyroclastic lherzolites (16CA06, 16CA11, 16CA15) have lower equilibrium temperatures between 600 and 700 °C. Coarse-porphyroclastic peridotites 16CA03, 16CA15, and 16CA18 display core-rim variations in equilibrium temperature. In most cases, rim Ca-in-opx temperatures are higher than core ones, but there is no systematic trend. All samples that display core-rim variations also show significant dispersion in both core and rim temperatures at the sample scale (bars in Fig. 10). Coarse-granular peridotites 16CA07, 16CA08, 16CA09, and BO9 have intermediate equilibrium temperatures between 800 and 900 °C and less variations at sample scale as well as between cores and rims. Comparison with previous thermometry data on Macau peridotite xenoliths indicates that the present sampling is representative of the variability in this suite (Fig.9). Analysis of the full dataset also highlights that there is no relation between equilibrium temperatures and sampling site. The full range of equilibrium temperatures is observed both among Pico do Cabugi xenoliths, which is the best sampled site, and among xenoliths from other Macau volcanics.

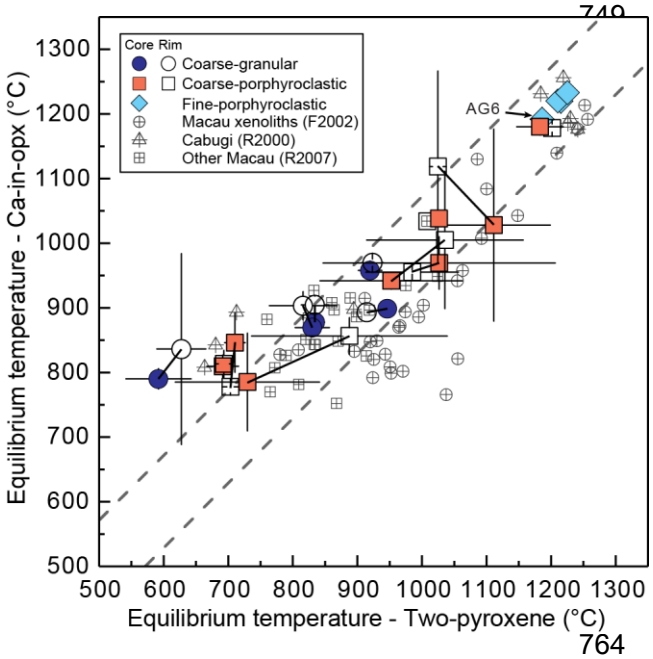

Fig. 9. Average core and rim equilibrium temperatures calculated using the cpx-opx thermometer (TTA98, Taylor, 1998) and the Ca-in-opx thermometer (Ca-in-opx, Brey and Kohler, 1990, revised by Nimis and Grutter, 2010). Chemical compositions from Rivalenti et al. (2000) and (2007) and Fodor et al. (2002) were used to recalculate the equilibrium temperatures for their samples using the same thermometers (data is presented in Supplementary Material Tables S2 and S3). Error bars represent data spread within each sample. Gray dashed lines outline a ±70°C variation between the two thermometers.

To estimate the Cenozoic geotherm in the northern Borborema Province, we plotted the TTA98 equilibrium temperatures of the studied xenoliths against the peridotite phase diagram in the upper mantle (spinel-out, plagioclase-out, and garnet-in curves for different Cr contents from O'Neill, 1981 and Klemme, 2004), as well as equilibrium geotherms for different surface and reduced heat flows (Fig. 11). The geotherms are calculated assuming a surface heat flow of 60 or 70 mW/m^2 (Hamza et al., 2018), a Moho depth of 32 km (Almeida et al., 2015), an exponential decrease of the radiogenic heat production with depth, with a characteristic depth of 10 km, and a reduced heat flow of either 30 or 45 mW/m^2. For comparison, we also indicate the depth of the

lithosphere-asthenosphere boundary determined by P-S receiver functions for seismic station RCBR (Heit et al., 2007) and the partial melting conditions estimated based on the compositions of the most primitive melts of the Cenozoic Macau and Mesozoic Ceará-Mirim suites (Ngonge et al, 2015a,b).

P-T equilibrium conditions of the peridotites are displayed as a fixed temperature corresponding to the TTA98 thermometry prediction, but as a pressure range, because there are no reliable barometers for spinel-facies peridotites. The range of equilibrium pressure conditions is defined by the occurrence of spinel in absence of plagioclase or garnet for the actual Cr content of each peridotite (O'Neill, 1981; Klemme, 2004).

The wide range of equilibrium temperatures suggests that the studied peridotites represent a complete sampling of the subcontinental lithospheric mantle. The absence of garnet in the entire suite, which is largely composed of peridotites with Cr# < 15, constrains a maximum equilibrium depth of the studied peridotites shallower than 75 km (Fig. 10). By consequence, the equilibrium conditions of the Macau peridotite xenoliths, except 16CA14 that has the lowest and likely unreliable equilibrium temperature, are better fitted by the hotter geotherm (green line in Figure 10).

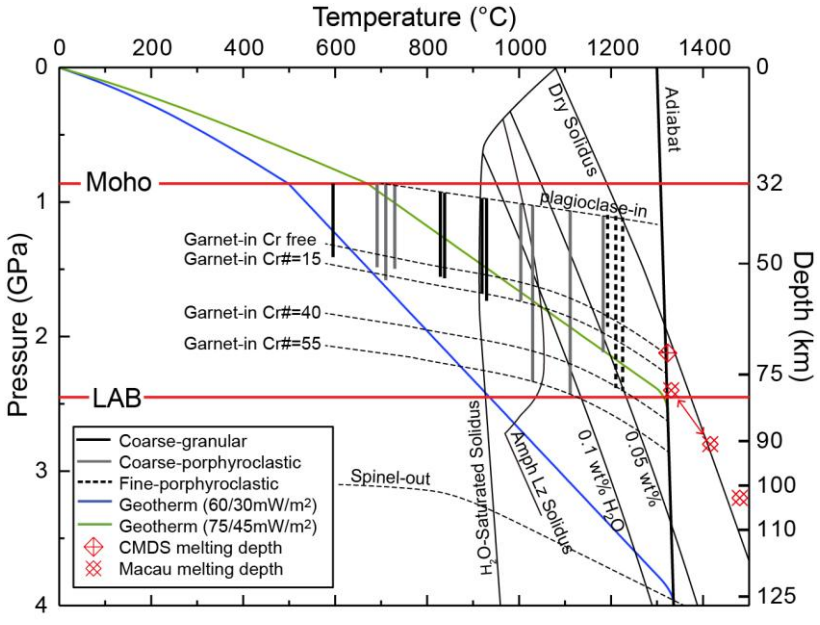

Fig. 10. P-T diagram comparing the equilibration conditions estimated for the studied Macau xenoliths to two possible steady-state geotherms for the north Borborema province (surface / reduced heat flows indicated in parenthesis). Xenolith data is better fitted by the hotter geotherm (surface and reduced heat flows of 75 and 45mW/m^2, respectively). Since no barometers are available for spinel peridotites, equilibrium pressure ranges are presented as bars, based on the absence of plagioclase and of garnet in the studied peridotites, considering their Cr# (Supplementary Information Table S1) and the effect of Cr on the spinel-garnet phase transition (Klemme, 2004; O'Neill, 1981). Dry and wet solidus with variable H_2O contents after Ringwood (1975). Moho and Lithosphere-Asthenosphere Boundary (LAB) depths derived from S-P and P-S receiver function analyses (Almeida et al., 2015, Heit et al., 2007) as well as partial melting conditions derived from the primitive melt compositions of the Cretaceous Ceará-Mirim dyke system (CMDS) and Cenozoic Macau volcanics (Ngonge et al., 2016a,b) are displayed for comparison.

4.6. Seismic properties

For calculating seismic properties, we divided the xenoliths into two groups as a function of their TTA98 equilibrium temperature: low (T < 1000 °C) and high-temperature (T > 1000 °C). Then, we estimated the elastic tensors of the individual samples (Supplementary Material Table S3) for the pressure and temperature conditions predicted at 50 km (1.46 GPa and 916 °C) and 70 km depth (2.12 GPa and 1189°C) for the geotherm that best fits the xenolith data (Qs=70 mW/m^2 and Qm=45 mW/m^2, green line in Figure 10).

Seismic anisotropy patterns of the individual samples vary slightly as a function of the olivine CPO symmetry. As usual, the seismic anisotropy intensity correlates positively with both the olivine CPO strength and olivine modal content (Figure 11). On average, the peridotites equilibrated at temperatures <1000°C tend to display lower anisotropy, due to both more dispersed olivine CPO and lower olivine contents. However, seismic anisotropy intensity does not increase linearly with increasing J-index. By consequence, overestimation of the olivine CPO intensity for fine-porphyroclastic harzburgite AG7 does not result in similar overestimation of its seismic anisotropy. The maximum S-wave polarization anisotropy varies from 5.5 to 7.3% in the low-temperature peridotites and from 5.9 to 10% in the hign-temperature ones (Fig. 11 and Table 3). Similarly, the maximum P-wave propagation anisotropy varies from 7.4 to 10% and from 7.7 to 14.2% (Table 3). The maximum fast (S1) wave propagation anisotropy varies from 3.0 to 5.9% in low-temperature samples and from 4.1 to 7.2% in high-temperature ones, whereas the maximum slow (S2) wave propagation anisotropy varies from 3.4 to 5.2% and from 1.9 to 7.3%, respectively (Table 3).

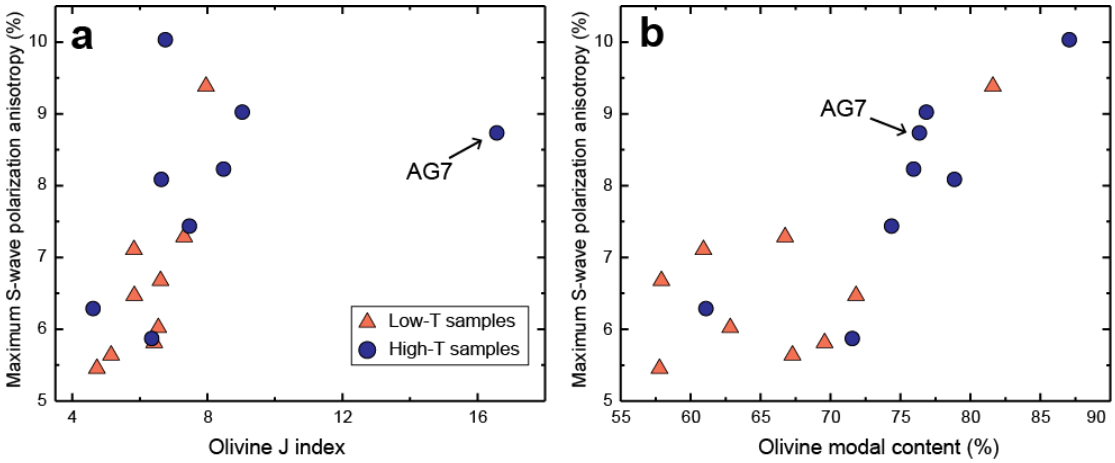

Fig. 11. Maximum S-wave polarization anisotropy (%) vs. (a) olivine CPO intensity (J index) and (b) olivine modal content (%) for all studied xenoliths. Seismic anisotropy data for individual samples are listed in Table 3.

Since seismic waves average elastic properties over large volumes, we calculated average elastic tensors for the low-temperature and high-temperature groups by assuming a coherent orientation of the past flow directions and planes (assumed as parallel to the [100] and [010] maxima of the olivine CPO, respectively – this assumption is justified by the analysis of

the CPO as discussed in the next section) over the entire lithosphere using a constant structural reference frame. These average seismic anisotropy patterns (Fig. 12) represent the maximum possible seismic anisotropy in the shallow (low-temperature group) and deep (high-temperature samples) sections of the lithospheric mantle, if the present sampling is representative of the volumes of the different microstructures and compositions in the lithospheric mantle in this region.

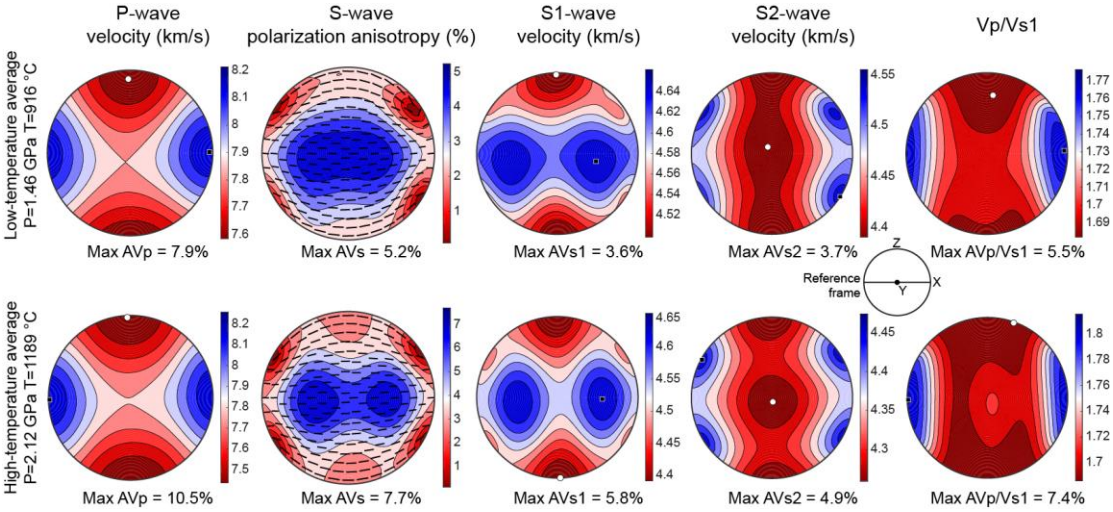

Fig. 12. Average seismic properties for shallow and deep sections of the lithospheric mantle beneath the study area calculated by averaging the elastic constant tensors of the eight low-temperature samples calculated for 916°C, 1.46GPa and of the nine high-temperature samples calculated for 1189°C, 2.12GPa. Lower hemisphere stereographic projections presenting the variation of the property as a function of the propagation direction relatively to the structural reference frame (flow direction (X) and normal to the flow plane (Z) shown by the insert). Black squares mark the highest values and white circles mark the lowest ones. Seismic properties data are listed in Table 3 and the elastic tensors, in Supplementary Material Table S4.

Seismic anisotropy patterns for the shallow and deep lithospheric mantle are similar, but as already discussed, the lower part of the lithosphere is more anisotropic (Fig. 12). The average maximum P-wave propagation anisotropy is 10.5% with velocities ranging between 7.4 and 8.3 km/s, compared to 7.9% in the shallow lithospheric mantle, where P-wave velocities vary between 7.6 km/s normal to the flow plane and 8.2 km/s parallel to the flow direction frozen in the lithospheric mantle (Table 3). The average maximum S-wave polarization anisotropy in the lower lithospheric mantle is 7.7% compared to 5.2% in the shallower levels; in both cases it is observed for S-waves propagating within the flow plane but at <45° of the flow direction. Low S-wave polarization anisotropy is observed for all waves propagating at low angle to the XZ plane, that is, the plane that contains both the flow direction and the normal to the flow plane. For all propagation directions in which a significant polarization anisotropy is observed, the fast S-wave is polarized in the plane containing the flow direction. The average maximum S1-wave propagation

anisotropy increases from 3.6% to 5.8% from the shallow to the deep mantle lithosphere. S1 velocity is maximum within the flow plane and minimum normal to it. S1-waves propagating within this plane show a 90° periodicity in the velocity variation. S2-waves average maximum propagation anisotropy increases from 3.7% to 4.9% with depth. High S2 velocities are associated with propagation within the XZ plane at ca. 45° to the flow direction (X) and low velocities are observed for all propagation directions at high angle to X. The maximum Vp/Vs1 ratio anisotropy increases from 5.5% to 7.4% with depth. Highest Vp/Vs1 ratios (1.78-1.8) are observed for waves propagating parallel to the flow direction and the lowest Vp/Vs1 ratios for waves propagating normal to the flow plane.

5. Discussion

5.1. Deformation, annealing, and reactive melt percolation

Coarse-granular peridotites show polygonal grain shapes for both olivine and pyroxenes and low intragranular misorientations (olivine M2M values < 2°, Fig. 2). However, they have well-developed olivine CPO (Figs. 5 and 6). This association supports that the deformation that produced the CPO was followed by annealing (static recrystallization), which effectively reduced dislocation densities and re-equilibrated grain shapes. The analysis of the relative intensity of the orientation of [100], [010], and [001] of olivine, of the relations between olivine and pyroxene CPOs, and of the relations between olivine CPO and SPO (when a SPO was observed) points to deformation by dislocation creep with dominant activation of the [100](010) slip system in olivine, [001](100) in orthopyroxene, and [001](0kl) in clinopyroxene (Tommasi et al. 2000, Bascou et al. 2002). Coarse-granular peridotites have roughly constant olivine CPO intensities, but variable symmetry, covering the entire range from fiber-[100] to fiber-[010]. Fiber-[100] and orthorhombic olivine CPO are the usual patterns produced by simple shear under dry, high to moderate temperatures, and low pressure in the upper mantle (Tommasi et al., 1999; 2000; Hansen et al. 2014). Fiber-[010] patterns, on the other hand, require particular conditions, which may be: transpression (Tommasi et al., 1999), presence of melts during the deformation (Higgie and Tommasi, 2012, 2014; Qi et al. 2018), changes in the olivine CPO by oriented growth during recrystallization (e.g., Tommasi et al., 2008), or deformation under high stress or high pressure conditions, which would lead to increased activation of [001] glide (Durham and Goetze, 1977; Mainprice et al., 2005; Demouchy et al. 2013). The mineralogy and microstructures and CPO of the coarse-grained peridotites falsify the last hypothesis. However, the present data does not allow for discriminating among the other hypotheses. The different olivine CPO symmetry may therefore result from variations in deformation regime, with fiber-[010] CPO recording transpression (which is the dominant deformation regime in the Seridó belt during the Brasiliano event), presence or not of melts

during the deformation (all deformation events were accompanied by magmatism), or different CPO evolution during recrystallization.

Analysis of the bulk rock Mg# vs. olivine modal content relation (Fig. 13) shows that the compositions of most coarse-granular peridotites deviate from partial melting trends, suggesting the occurrence of refertilization processes. Yet, most coarse-granular peridotites have coherent olivine and pyroxene CPOs (Fig. 6), which indicate co-deformation of the two phases. Thus, if melt-rock reactions leading to refertilization occurred, they predated or were concomitant to the deformation. Refertilization reactions produce sutured pyroxene-olivine boundaries and irregular shapes for both minerals. The equilibrated pyroxenes grain shapes in most coarse-granular peridotites indicate therefore that reactive melt percolation producing refertilization also predated annealing. It also implies that interphase grain boundary rearrangements during annealing were effective. These rearrangements depend on transport of ions along grain boundaries in a similar way to the growth of porphyroblasts in a metamorphic rock, but with weaker driving forces (grain boundary energy reduction opposed to chemical gradients). Most coarse-granular peridotites equilibrated around 900°C (Fig. 9). At this temperature, given the diffusivity of Si along olivine and enstatite grain boundaries ($\leq 10^{-27} m^3/s$; Fisler et al. 1997; Fei et al. 2016), grain boundary equilibration at the 250 µm scale, which is the average amplitude of the sinuosity of the olivine-pyroxene grain boundaries in the coarse-porphyroclastic peridotites (Fig. 3c,d), will occur on time scale of several hundreds of Ma. In contrast, irregular pyroxene grain shapes (high orthopyroxene shape factor ~2°, Fig. 2) in 16CA14 and BO9 point to a later stage of melt percolation. Indeed, in both samples, part of the pyroxenes shows crystal orientations not coherent with the olivine CPO (Fig. 6).

Coarse-porphyroclastic peridotites show less equilibrated microstructures. All major phases show sinuous grain boundaries (higher shape factors) as well as undulose extinction and subgrains, which translate into higher M2M values (Fig. 2). This implies a less effective annealing due to either a more recent deformation or lower post-deformation temperatures. The former hypothesis may apply for the coarse-porphyroclastic peridotites with high equilibrium temperatures (≥1000°C, Fig. 9) and the latter, for those with low equilibrium temperatures (<800°C, Fig. 9). Similarly to the coarse-granular peridotites, olivine CPO in coarse-porphyroclastic peridotites is consistent with deformation by dislocation creep with dominant activation of the [100](010) system. This interpretation is corroborated by the high frequency of (100) subgrain boundaries. However, the CPO patterns and intensities are more varied than those of coarse-granular peridotites (Figs. 5 and 6). Coarse-porphyroclastic harzburgites have strong fiber-[100] olivine CPOs, typical of simple shear deformation (Tommasi et al., 1999; 2000; Bystricky et al, 2000; Hansen et al., 2014). Lherzolites have orthorhombic to fiber-[010] olivine CPOs with variable strength. As for the coarse-granular peridotites, the

fiber-[010] olivine in these coarse-porphyroclastic peridotites may record either a component of transpression or the presence of melts during the deformation.

Although some coarse-porphyroclastic peridotites plot along partial melting trends in Fig. 13, evidence for reactive melt percolation leading to crystallization of pyroxenes or olivine is widespread. It encompasses: (i) the interpenetrating olivine-pyroxene grain boundaries and the locally interstitial shapes of pyroxenes (Figs. 3 and 4), which imply lack of microstructural equilibrium, (ii) the high variability of the olivine and pyroxenes chemical compositions both within grains and between grains in a sample (Fig. 8), which indicates absence of chemical equilibration, and (iii) lack or weak consistency between the olivine and the pyroxenes CPOs (Fig. 6). The latter feature is specific to the coarse-porphyroclastic harzburgites, which also show the highest equilibrium temperatures and least equilibrated mineral compositions among the coarse-porphyroclastic peridotites, implying that reactive melt percolation in these rocks, which sample the lower lithospheric mantle section in the province, postdates the deformation and is rather recent.

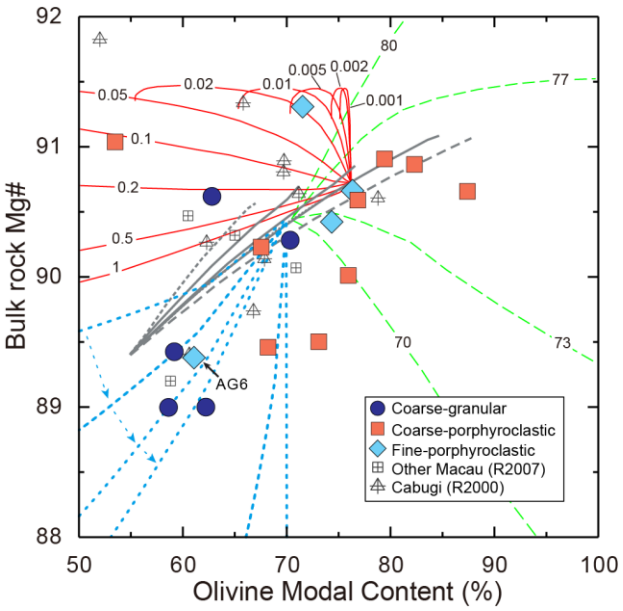

Fig. 13. Olivine modal content (%) vs. bulk rock Mg# in the studied xenoliths compared to evolutions predicted for partial melting and reactive melt percolation in the mantle. Gray lines represent the composition evolution predicted by various partial melting models using a source composition with 89.3 Mg# and 55% of olivine up to complete consumption of clinopyroxene (Bodinier & Godard, 2014). Colored lines represent different melt-rock reactions after Bodinier & Godard (2014). Red solid lines correspond to precipitation of clino- and orthopyroxene at the expense of olivine and melt with different mass ratio of crystallized minerals versus infiltrated melt (numbers of the top of the curves). Green dashed lines show olivine-forming reactions with melts with different Mg# (numbers of the top of the curves). Blue dotted lines represent multiple episodes of refertilization, starting with low Mg# melts ('primitive' melt Mg#=74.5), in which the peridotites successively reacted with the evolved melt resulting from previous infiltration stage (Bodinier et al., 2008). Compositions of Macau peridotite xenoliths previously studied by Rivalenti et al. (2000) and (2007) are plotted for comparison.

Fine-porphyroclastic peridotites show a bimodal olivine grain size distribution and strong intragranular misorientations in the olivine porphyroclasts characterized by dynamic recrystallization (Figs. 3 and 4). At the high equilibrium temperatures recorded by these peridotites (≥1200°C, Fig. 9), diffusion is fast. The low annealing level of the microstructures in these peridotites, indicated by the high intragranular misorientations in the porphyroclasts (Figs. 2 and 3), implies therefore that the deformation episode that produced the recrystallization shortly predated their extraction from the mantle by the Macau volcanism.

The variation in recrystallized grain sizes between the various fine-porphyroclastic peridotites might record variations in stress (from ~75 MPa in AG6 to ~10 MPa using the recrystallized grain size paleopiezometer of Van der Wal et al., 1993), but the coarser recrystallized grain sizes result more probably from partial annealing. The stresses estimated for lherzolite AG6 are high and, for the equilibrium temperature of 1200°C of these peridotites, imply extremely high strain rates of 10^{-6} to 10^{-9} s^{-1} based on usual olivine flow laws (Chopra and Paterson, 1981; Hirth and Kohlstedt, 2003; Gouriet et al. 2019). The microstructure of these peridotites is indeed very similar to the mosaic microstructure of deep sheared kimberlite-borne peridotites, which has been traditionally attributed to the initial stages of kimberlite dyke formation, due to the high stresses and high rates inferred based on the recrystallized grain sizes and equilibrium temperatures (e.g., Green and Gueguen, 1974; Boullier, 1977; Skemer and Karato, 2008; Baptiste et al. 2012). Similar microstructures have been observed in the deepest mantle xenoliths from the Labait alkaline lavas in the Tanzanian craton (Vauchez et al., 2005) and from Malaita alnoites in the Ontong Java plateau (Tommasi and Ishikawa, 2014) with similar interpretations proposed.

Fine-porphyroclastic peridotites with high equilibration temperatures have also been described in Cenozoic peridotite xenoliths, which sample the mantle beneath major Neoproterozoic shear zones at the border of the Hoggar swell, N Africa (Kourim et al., 2015). However, in the Hoggar peridotites, equilibration temperatures are lower (1000-1100°C) and olivine recrystallization was associated with crystallization of elongated aggregates of clinopyroxene and amphibole. The fine-porphyroclastic microstructures were therefore interpreted as resulting from ductile reactivation and melt channeling in Neoproterozoic shear zones in response to the development of the Hoggar swell in the Cenozoic. However, in the fine-porphyroclastic peridotites from the Borborema province, there is no evidence for neocrystallization of pyroxenes or amphiboles within the recrystallized domains. Moreover, the fact that the recrystallized domains in the fine-porphyroclastic peridotites from the Borborema province do not align marking a foliation (Fig. 3e,f) and the lack of elongation of the pyroxenes suggests that the recrystallization was associated with high stresses, but low finite strains. This association, together with the equilibrium temperatures, which imply that these peridotites are derived from

the base of the lithospheric mantle, is consistent with localized deformation associated with the formation of the dykes that fed the Cenozoic magmatism.

Analysis of the olivine modal composition relative to the bulk rock Mg# implies that lherzolites AG7 and AG6 were affected by refertilization processes (Fig. 13). The Fe-rich compositions of olivine and pyroxenes in AG6 (Fig. 8a,b) further point to high cumulated melt-rock ratios. Ortho- and clinopyroxenes in these two lherzolites have unusual irregular, but rounded shapes, which clearly differ from those in coarse-porphyroclastic peridotites (cf. EBSD phase maps in Fig. 3). Yet determining when this refertilization occurred is difficult. At the high temperatures at which these peridotites equilibrated, chemical diffusion is fast. Disequilibrium in mineral chemistry at the sample scale, which would point to melt-rock interaction shortly before extraction is only observed in AG7. Harzburgites PC105 and PC109 plot along the partial melting trends in Fig. 13 and have higher Mg# in olivine and pyroxenes (Fig. 8a,b), but they also display chemical evidence for some melt-rock interaction, like enrichment in Ca in olivine (Fig. 8c).

5.2. Cenozoic geotherm and thermal evolution of the NBP lithospheric mantle

We do have evidence in this study supporting a rather hot Cenozoic geotherm beneath the North Borborema Province. As illustrated in Fig. 10, equilibrium conditions of the xenoliths are consistent with the surface heat flow of 60-70 mW/m^2 measured in the Borborema Province (Hamza et al., 2018) if the heat flow from the convective mantle is rather high ($45mW/m^2$). This implies a slightly hotter than average sublithospheric mantle beneath the Borborema Province, consistently with the low P-wave velocity anomaly imaged at 100 km depth beneath the Northern Borborema Province east of the Macau-Queimadas volcanic alignment (Simões Neto et al., 2019; Fig. 1) and with the weak low S-wave velocity anomaly imaged beneath this region in a recent global full-waveform tomography model (ca. -2%; French et al., 2013). The equilibrium geotherm that best fits the equilibrium temperature and pressure conditions of the Borborema Province is also consistent with the seismological constraints for the lithosphere-asthenosphere boundary (LAB) depth of 80km (Heit et al., 2007) and with the partial melting conditions calculated for the Macau most primitive basalts (1330-1415°C at 80-93km; Ngonge et al. 2015b; cf. Fig. 10). A hotter than average sublithospheric mantle may also account for the Cenozoic uplift of the Borborema Plateau (Almeida et al., 2015; Luz et al., 2015; Klöcking et al., 2018). The equilibrium temperatures of the studied xenoliths may therefore represent an equilibrium geotherm established in the Cenozoic in response to a slightly hotter than normal convective mantle temperature. Geophysical data imply that these conditions are still active today. Data on the xenoliths does not bring any constraints on the causes of the higher than average sublithospheric temperatures, which may result from a diffuse mantle upwelling, perturbation of the convective pattern by the São Francisco craton, or, as suggested by Simoes Neto et al.

(2018), lateral channeling of hot material from a mantle plume upwelling to the SW of the Province.

The present data also do not constrain the evolution through time of the upper mantle temperatures beneath the North Borborema Province. The estimated melting conditions for the most primitive basalts of the Cretaceous CMDS (ca. 1320 °C at 70 km depth; Ngonge et al., 2015a) are shallower than those for the Cenozoic Macau volcanics (Ngonge et al., 2015b, suggesting an even shallower LAB beneath the North Borborema Province in the Mesozoic. This suggests that the lithosphere beneath the NBP has probably cooled and thickened after the Mesozoic extension. The deepest xenoliths might therefore represent material accreted to the base of the lithosphere after the Mesozoic.

5.3. Seismic anisotropy in the lithospheric mantle: comparison with SKS splitting data

Shear wave splitting data in the Borborema Province is highly heterogeneous and does not relate in a simple way to neither the outcropping geological structures nor the absolute plate motion of the South American plate (Bastow et al., 2015). However, the station RCBR, which is the closest to sampling sites, being located ca. 50 km east of the Pico do Cabugi, displays a NNE-oriented fast S-wave polarization parallel to the trend of the Seridó belt and of the main Brasiliano shear zones in the region, and a high delay time (1.9 s) based on 9 individual measurements (Assumpção et al., 2011).

If we consider that at least part of the SKS splitting measured at RCBR is produced in the lithospheric mantle, the orientation of the fast polarization direction constrains the projection of the lineation on the horizontal plane to be oriented in the NNE direction (9±11°). However, there are no constraints on its plunge or on the dip of the foliation. To draw constraints on the orientation of the foliation and lineation in the lithospheric mantle, which would allow to discuss possible coupling between crustal and mantle structures, we estimate the contribution of the lithospheric mantle to the SKS splitting delay time (Δt) for three end-member orientations of the foliation and lineation in the lithospheric mantle, illustrated in Fig. 14, and compare these predictions to the observations at RCBR.

Common conversion point (CCP) receiver function stacks support that the Moho is at ~32km (Almeida et al., 2015) and the LAB is at ~80km based on the S receiver function data by Heit et al. (2007) in the Northern Borborema Province. The thickness of the lithospheric mantle in this region is therefore 48 km. Based on the thermobarometric data (Fig. 10), we divided the lithosphere into two layers and calculated the lithospheric mantle contribution to the measured delay time using the average seismic anisotropy of the low temperature peridotites (32 - 56km, < 1000 °C) and of the high-temperature ones (56 - 80 km, > 1000 °C).

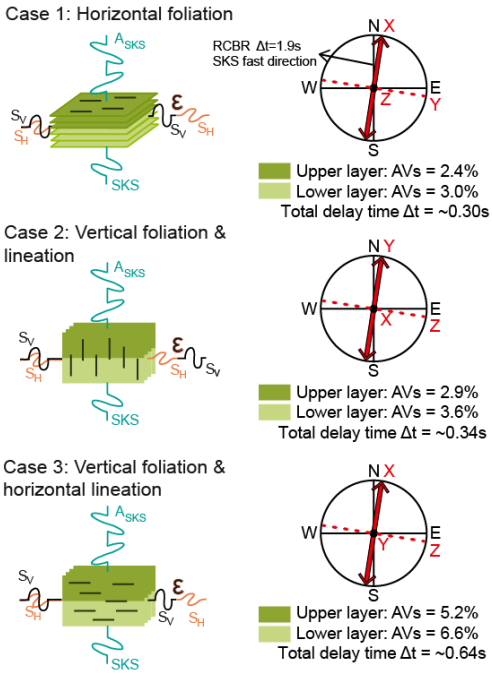

Fig. 14. Estimation of the maximum SKS splitting that may be produced in the lithospheric mantle for three end-member orientations of the flow directions and planes. Stereographic projections show the relation between the geographic (in black) and the structural (in red) reference frames in the three cases. The vertical is in all cases at the center of the diagram. The orientation of the fast SKS polarization (thick red arrow) is based on SKS splitting data for station RCBR.

If the foliation is horizontal and the lineation NE-SW (case 1), the S-wave polarization anisotropy is 2.4% for upper lithospheric mantle and 3.0% for lower lithospheric mantle. The cumulated SKS delay time is only ~0.30s. If both the foliation and lineation are vertical (case 2), the fast SKS polarization constrains the direction of the foliation, and SKS waves propagate parallel to the lineation. The S-wave polarization anisotropy in this direction is low, like in case 1. It is 2.9% for upper layer and 3.6% for lower one and the delay time that may be cumulated in the lithospheric mantle is ~0.34s. If the foliation is vertical but the lineation is horizontal and parallel to the fast SKS polarization direction (case 3), the S-wave polarization anisotropy is higher. It is 5.2% in the upper lithospheric mantle and 6.6% for lower lithospheric mantle, leading to a cumulate delay time in the lithospheric mantle of 0.64s.

In case 3, the lithospheric mantle has a fabric consistent with the crustal deformation around station RCBR, which is dominated by dextral strike-slip in transpressional structures in the Seridó belt and in the shear zones that border it. This case would therefore imply a structuration in the lithospheric mantle coherent with the crustal deformation in the Brasiliano event. Seismic anisotropy in the lithospheric mantle, with anisotropy directions parallel or subparallel to the main nearby Neoproterozoic shear zones is also required by receiver function analysis on most stations in the Borborema Province (Lamarque and Julià, 2019). At station RCBR, this study proposes horizontal anisotropy axis trending NNE in the lithospheric mantle, consistent with case 3.

It is important to note that even for case 3, the lithospheric mantle can contribute to < 1/3 of the SKS delay time measured at the RCBR station (1.9 ± 0.2 s, Assumpção et al., 2011). Thus a large part of the SKS signal at RCBR has to be produced in the asthenosphere and, for the contributions of the lithosphere and asthenosphere to add up, asthenospheric flow directions

should not deviate much from NNE. Present-day absolute plate motion (APM) directions for NE Brazil do not follow this direction. Hotspot reference frame models, such as HS3-Nuvel-1A, predict an ENE direction, whereas no-net rotation models predict a NNW direction (Gripp and Gordon, 2002). However, a NNE flow direction in the sublithospheric mantle beneath the Borborema province is predicted by models in which the present-day mantle flow is calculated based on a density anomaly distribution derived from global seismic tomography models (cf. Fig. 8 in Assumpção et al., 2011).

5.4. Relations between the mantle structure and the geodynamical evolution of the Borborema Province

When did the deformation, annealing, and reactive melt percolation processes recorded by the xenoliths happen? How do they relate to the geodynamical evolution of NE Brazil? There are no ways of dating deformation processes in the mantle. However, we may try to use the data discussed in the previous sections to constrain the imprint of the different tectonic events that affected the Borborema Province in the lithospheric mantle.

The coarse-granular microstructures, with their well-equilibrated pyroxene-olivine grain boundaries, imply effective annealing, which, at the equilibrium temperatures of these xenoliths, require very long time delays, on the order of several hundreds of Ma. Although the temperature may have varied since the deformation of the xenoliths, to re-equilibrate the pyroxene-olivine grain boundaries in <100 Ma, temperatures ≥ 1100°C, that is >200°C above those recorded by the xenoliths at the time of extraction, are needed. Coarse-granular microstructures are well expressed among the low-equilibrium temperature xenoliths, suggesting that the shallow part of the lithospheric mantle beneath the Macau volcanics records essentially old tectonic events. The seismic anisotropy data in the region imply that this lithospheric structure results from Neoproterozoic dextral strike-slip and transpressional intraplate deformation. A pre-Mesozoic origin of this mantle fabric is also suggested by the higher annealing degree of the microstructures of the Borborema xenoliths relative to the Fernando de Noronha ones (Fig. 2). Indeed, Fernando de Noronha mantle xenoliths record deformation frozen up in the oceanic lithosphere by plate cooling, which post-dates the opening of the Atlantic (Liu et al., 2019).

Some coarse-porphyroclastic lherzolites have lower equilibrium temperatures (≤800°C) than most coarse-granular peridotites. This is not a sampling location effect, since both types of peridotites were sampled in Pico do Cabugi. The higher olivine intragranular misorientations and less equilibrated olivine and pyroxene grain shapes indicate less effective annealing, pointing to either slower annealing due to cooler temperatures or a more recent deformation event. In the first case, the deformation recorded by these xenoliths may also be associated with the Brasiliano event. In the second, these peridotite may record Cretaceous or even younger deformation

preserved in the shallow lithospheric mantle. In any case, the studied xenolith suite exhibits no evidence of strong deformation under low temperature conditions. There are no xenoliths displaying mylonitic microstructures, with marked grain size reduction of olivine and strong elongation of olivine and orthopyroxene porphyroclasts, which are usually observed in extensional shear zones developed in peridotite massifs under low temperature conditions (≤1000°C; e.g., Drury et al., 1991; Frets et al., 2014; Kaczmarek and Tommasi, 2011). Although annealing could have partially obliterated the olivine deformation microstructure, it cannot change the aspect ratios of the orthopyroxenes in a time scale of 100 Ma. Thus if the low temperature coarse-granular peridotites correspond to sections of the lithospheric mantle deformed during the Mesozoic, these are low strain zones and their olivine CPO and seismic anisotropy may still preserve orientations produced by the previous deformation episodes.

Based on the microstructures of the low equilibration temperature peridotites and on the seismic anisotropy data, we conclude therefore that the shallow sections of the lithospheric mantle of the Borborema province records coupled crust and mantle deformation during the formation of the Borborema shear zone system in the Neoproterozoic. The present dataset has no evidence for extensive reworking of the shallow lithospheric mantle by the extensional deformation in the Cretaceous or during the Cenozoic uplift of the province. Yet, the absence of (annealed or not) low-temperature mylonites in the xenolith sampling does not imply that shear zones accommodating a Mesozoic extension did not form in the shallow lithospheric mantle of the Borborema Province, since our sampling is punctual and such a deformation would be by nature heterogeneous.

The coarse-porphyroclastic microstructures that characterize the lower part of the lithospheric mantle (equilibrium temperatures > 1000°C) are more difficult to relate to a given tectonic episode. Partial melting conditions estimated for the Ceará-Mirim basalts suggest that the lithosphere-asthenosphere boundary was shallower in the Cretaceous than in the Cenozoic (cf. Fig. 10 and discussion section 5.2). This would imply that the deep lithospheric mantle beneath Borborema might be composed by material accreted by cooling since the Cretaceous. Comparison between the microstructures of these coarse-porphyroclastic peridotites with those of peridotite xenoliths from the nearby Fernando de Noronha (FN) archipelago, formed in response to Cenozoic volcanism onto 100-105 Ma old crust in the equatorial Atlantic (Liu et al., 2019) also favors a Mesozoic age for the deformation of these peridotites. Indeed, the olivine M2M and olivine and pyroxene shape factors of the Borborema peridotites overlap with the lower range of olivine M2M and shape factors, that is, with the most annealed microstructures of the FN peridotites (Fig. 2). The FN peridotites record an asthenospheric deformation, which has been frozen in the oceanic lithosphere by cooling and evolved by annealing since then (Liu et al., 2019). Their

deformation is therefore younger than the opening of the Equatorial Atlantic. The similar to slightly stronger annealing degree of the coarse-porphyroclastic Macau peridotites suggests that the deformation that produced these microstructures in the deep section of the lithospheric mantle beneath the Borborema province might be related to the Cretaceous extension. Thus, although this event did not result in widespread deformation of the shallow levels of the lithospheric mantle, it might have reworked the base of the lithosphere (bottom-up lithospheric thinning?). Yet the high SKS delay times in station RCBR do not favor strong deviations in flow direction from NNE across the entire lithosphere-asthenosphere section, implying that either strains were small and did not change the Neoproterozoic CPO orientations or that flow directions during extension were at high angle to the extensional structures in the Cretaceous basins and to the Equatorial Atlantic spreading directions.

Finally, the very low annealing degree and high equilibration temperatures of the fine-grained porphyroclastic microstructures necessarily imply deformation close in time to the Cenozoic Macau volcanism. Based on the microstructural evidence for high stresses, but low finite strains for this deformation, we propose that it is related to the formation of the dykes that brought the Macau volcanics to the surface. The equilibration temperatures of the xenoliths imply a rather hot geotherm, leading to an 80-km thick lithosphere in the Cenozoic. This is consistent with melting depths inferred for the Macau basalts (Ngonge et al., 2015b). It is also coherent with the present-day thermal state of the lithospheric and sublithospheric mantle as imaged by geophysical data .

Dating the reactive melt percolation events is even more difficult than the deformation ones. The equilibrated microstructures and the coherent olivine and pyroxene CPOs in the coarse-granular peridotites undoubtedly point to a Brasiliano or older reactive melt percolation event. Coarse-porphyroclastic peridotites record younger melt percolation events, which in some cases predated or were synchronous to the main deformation recorded by the samples. However, in other cases, like in the coarse-porphyroclastic harzburgites, melt percolation post-dated the main deformation. Finally, the non-equilibrated chemical compositions at the sample scale observed in many samples, in particular the high-temperature coarse-porphyroclastic harzburgites, point to a last event of melt percolation that shortly predated the extraction of the peridotites. In summary, this peridotite suite recorded multiple reactive melt percolation events, probably well separated in time and related to the different magmatic episodes recorded in the crust.

6. Conclusion

Integrated analysis of microstructures, crystal preferred orientations, mineral chemical compositions, and equilibrium temperatures in a suite of 22 peridotite xenoliths reveals that the lithospheric mantle beneath the Northern Borborema Province preserves microstructures related to different deformation

episodes since at least the Neoproterozoic. In all cases, olivine CPO points to deformation by dislocation creep with dominant activation of [100](010) slip system. However, the deformation microstructures were modified by variable degrees of annealing. The analysis of the extent of the annealing considering the equilibration temperatures allows rough 'dating' of the deformation episodes and relating them to the major deformation events recorded in the crust. The well-annealed olivine microstructures and pyroxene shapes in coarse-granular peridotites equilibrated at ca. 900°C indicate that the last deformation event that affected these peridotites is several hundreds of Ma old. In contrast, the fine-porphyroclastic peridotites, which have equilibrium temperatures ≥1200°C, have suffered a high stress deformation, which shortly predated their extraction, probably related to the dykes that fed the Cenozoic volcanism. The coarse-porphyroclastic microstructures, which are observed both in the shallow and deep lithospheric mantle are more difficult to relate to a given tectonic episode. Yet comparison between the microstructures of these peridotites and those of peridotite xenoliths from nearby Fernando de Noronha island, which sample the oceanic mantle lithosphere of an old domain of the Equatorial Atlantic, suggest that the high-temperature coarse-porphyroclastic peridotites may record deformation related to the Cretaceous extension. Multiple reactive melt percolation events, probably well spaced in time, may also be inferred based on the microstructures, modal, and mineral compositions of the xenoliths.

Comparison of the computed seismic anisotropy of the lithospheric mantle based on the xenolith data to SKS splitting in nearby RCBR station supports that the strongest contribution of the lithospheric mantle to the measured anisotropy would correspond to a frozen strike-slip fabric parallel to the major NNE-NE Neoproterozoic shear zones in the region. A shallow lithospheric mantle fabric parallel to the Neoproterozoic shear zones is also suggested by anisotropic receiver functions (Lamarque and Julia, 2019). These observations corroborate the conclusion that the shallow lithospheric mantle in the Northern Borborema province still preserves a structure acquired by coupled crust-mantle deformation during the formation of the Borborema shear zone system in the Neoproterozoic. It also suggests that Cretaceous extension, which seems to be recorded in the deeper sections of the lithosphere, did not produce pervasive reworking of the shallow lithospheric mantle, pointing to 'partial' or total crust-mantle decoupling during this event. However, even if the entire lithospheric mantle has a frozen strike-slip fabric parallel to the major NNE-NE Neoproterozoic shear zones in the region, it can produce <1/3 of the measured delay time of 1.9s in station RCBR. Thus most of the measured SKS splitting in RCBR should record flow in the sublithospheric mantle, which also has a NNE orientation, which is not parallel to the APM, but is consistent with predictions of mantle circulation models for this region.

Finally, equilibrium temperatures and petrological compositions of the xenoliths indicate a rather hot Cenozoic geotherm, implying a ca. 80 km thick

lithosphere. This estimate is consistent with the melting conditions estimated for the formation of the Macau basalts (Ngonge et al. 2015). It is also coherent with geophysical data that point to a present-day 80-km thick lithosphere (Heit et al. 2007) and hotter than average sublithospheric mantle beneath this region (French et al., 2013; Simões Neto et al., 2019).

7. Acknowledgments

S. Liu was funded during his 14-month stay in Geosciences Montpellier by the China Scholarship Council. M.M. was supported by projects MIUR-PRIN 2005-2005049821 and 2017-20178LPCPW. C. Archanjo and M.H.B.M. Hollanda are thanked for assistance during field work. D. Delmas and C. Nevado prepared high-quality polished thin sections for EBSD measurements, which were performed with the assistance of F. Barou at the EBSD-SEM INSU national facility at Géosciences Montpellier (CNRS & Université de Montpellier). Electron microprobe analyses were carried out with the assistance of B. Boyer at the Service Microsonde Sud, Université de Montpellier. S. Piazolo and T. Morishita are warmly thanked for their constructive reviews.

The data used in this article are presented in the figures, tables, and supporting material. The raw EBSD data are available from the corresponding author upon request.

8. References

Abramson, E.H., Brown, J.M., Slutsky, L.J., Zaug, J.M., 1997. The elastic constants of San Carlos olivine to 17 GPa. J Geophys Res-Sol Ea. 102, 12253-12263.

Almeida, Y.B., Julià, J., Frassetto, A., 2015. Crustal architecture of the Borborema Province, NE Brazil, from receiver function CCP stacks: Implications for Mesozoic stretching and Cenozoic uplift. Tectonophys. 649, 68-80.

Ancelmi, M.F., Santos, T.J.S.d., Amaral, W.d.S., Fuck, R.A., Dantas, E.L., Zincone, S.A., 2015. Provenance of metasedimentary rocks from the Ceará Central Domain of Borborema Province, NE Brazil: implications for the significance of associated retrograded eclogites. J. S. Am. Earth Sci. 58, 82-99.

Anderson, O.L., Isaak, D., Oda, H., 1992. High-Temperature Elastic-Constant Data on Minerals Relevant to Geophysics. Rev. Geophys. 30, 57-90.

Archanjo, C. J., Hollanda, M. H. B., Rodrigues, S. W., Neves, B. B., & Armstrong, R., 2008. Fabrics of pre-and syntectonic granite plutons and chronology of shear zones in the Eastern Borborema Province, NE Brazil. J. Struct. Geol. 30, 310-326

Archanjo, C.J., Viegas, L.G.F., Hollanda, M.H.B.M., Souza, L.C., Liu, D., 2013. Timing of the HT/LP transpression in the Neoproterozoic Seridó Belt

(Borborema Province, Brazil): Constraints from UPb (SHRIMP) geochronology and implications for the connections between NE Brazil and West Africa. Gondwana Res. 23, 701-714.

Assumpção, M., Guarido, M., van der Lee, S., Dourado, J.C., 2011. Upper-mantle seismic anisotropy from SKS splitting in the South American stable platform: A test of asthenospheric flow models beneath the lithosphere. Lithosphere 3, 173-180.

Bachmann, F., Hielscher, R., Schaeben, H., 2010. Texture Analysis with MTEX – Free and Open Source Software Toolbox. Solid State Phenomena 160, 63-68.

Bachmann, F., Hielscher, R., Schaeben, H., 2011. Grain detection from 2d and 3d EBSD data - Specification of the MTEX algorithm. Ultramicroscopy 111, 1720-1733.

Baker, M.B., Stolper, E.M., 1994. Determining the Composition of High-Pressure Mantle Melts Using Diamond Aggregates. Geochim. Cosmochim. Acta 58, 2811-2827.

Baptiste V., Tommasi, A., Demouchy S., 2012. Deformation and hydration of the lithospheric mantle beneath the Kaapval craton. Lithos 149, 31-50.

Barruol, G., Bonnin, M., Pedersen, H., Bokelmann, G.H.R. & Tiberi, C., 2011. Belt-parallel mantle flow beneath a halted continental collision: the Western Alps. Earth Planet. Sci. Lett. 302, 429-438 .

Bascou, J., Tommasi, A., Mainprice, D. 2002. Plastic deformation and development of clinopyroxene lattice preferred orientations in eclogites. *J. Struct. Geol.,* **24**: 1357-1368

Bastow, I.D., Julia, J., do Nascimento, A.F., Fuck, R.A., Buckthorp, T.L., McClellan, J.J., 2015. Upper mantle anisotropy of the Borborema Province, NE Brazil: Implications for intra-plate deformation and sub-cratonic asthenospheric flow. Tectonophys. 657, 81-93.

Berger, E.T., Vannier, M., 1984. Dunites in Alkali Basalts from Oceanic Volcanic Islands - Petrological Approach. Bull. Mineral. 107, 649-663.

Bodinier, J.L., Garrido, C.J., Chanefo, I., Bruguier, O., Gervilla, F., 2008. Origin of Pyroxenite-Peridotite Veined Mantle by Refertilization Reactions: Evidence from the Ronda Peridotite (Southern Spain). J. Petrol. 49, 999-1025.

Bodinier, J.L., Godard, M., 2014. Orogenic, Ophiolitic, and Abyssal Peridotites, in: Holland, H.D., Turekian, K.K. (Eds.), Treatise on Geochemistry (Second Edition). Elsevier, Oxford, pp. 103-167.

Boullier, A.M., 1977. Structure des péridotites en enclaves dans les kimberlites d'Afrique du Sud. Conséquences sur la constitution du manteau supérieur. Bull. Soc. Française Minéral. Cristall.. 100, 214–229.

Bonnin, M., Tommasi, A., Hassani, R., Chévrot, S., Wookey, J., Barruol, G., 2011. Numerical modeling of upper mantle anisotropy beneath a migrating strike-slip plate boundary : the San Andreas fault system. Geophys. J. Intern. 191, 436-458

Brey, G.P., Kohler, T., 1990. Geothermobarometry in 4-Phase Lherzolites .2. New Thermobarometers, and Practical Assessment of Existing Thermobarometers. J. Petrol. 31, 1353-1378.

Bystricky, M., Kunze, K., Burlini, L., Burg, J. P.; 2000. High shear strain of olivine aggregates: Rheological and seismic consequences. Science 290, 1564-1567

Caby, R., Sial, A., Arthaud, M., Vauchez, A., 1991. Crustal evolution and the Brasiliano orogeny in Northeast Brazil. In: The West African orogens and Circum Atlantic correlatives. Springer- Verlag, pp. 373-397.

Castro, D.L., Bezerra, F.H.R., Sousa, M.O.L., Fuck, R.A., 2012. Influence of Neoproterozoic tectonic fabric on the origin of the Potiguar Basin, northeastern Brazil and its links with West Africa based on gravity and magnetic data. J. Geodyn. 54, 29-42

Castro, D.L., Oliveira, D.C., Gomes Castelo Branco, R.M., 2007. On the tectonics of the Neocomian Rio do Peixe Rift Basin, NE Brazil: Lessons from gravity, magnetics, and radiometric data. J. S. Am. Earth Sci. 24, 184-202.

Chai, M., Brown, J.M., Slutsky, L.J., 1997. The elastic constants of an aluminous orthopyroxene to 12.5 GPa. J Geophys Res-Sol Ea. 102, 14779-14785.

Chopra, P.N., Paterson, M.S., 1981. The Experimental Deformation of Dunite. Tectonophys. 78, 453-473.

Comin-Chiaramonti, P., Demarchi, G., Girardi, V.A.V., Princivalle, F., Sinigoi, S., 1986. Evidence of mantle metasomatism and heterogeneity from peridotite inclusions of northeastern Brazil and Paraguay. Earth Planet. Sci. Lett. 77, 203-217.

Costa, A.P., Cunha, A.L.C., Cavalcante, R., Medeiros, V.C., Spicily, A.L., Dantas, A.R., 2016. Carta Geologica Integrada de Areas de Relevante Interesse Mineral: Area Serido, Projeto Metalogenia das Provincias Minerais do Brasil, Escala 1:350000, Companhia de Pesquisas de Recursos Minerais, Brazil.

Darros de Matos, R.M., 1999. History of the northeast Brazilian rift system: kinematic implications for the break-up between Brazil and West Africa. Geological Society, London, Special Publications. 153, 55-73.

Drury, M.R., Vissers, R.L.M., Vanderwal, D., Strating, E.H.H., 1991. Shear Localization in Upper Mantle Peridotites. Pure Appl Geophys. 137, 439-460.

Durham, W.B. and Goetze, C., 1977. Plastic flow of oriented single crystals of olivine. 1.Mechanical data. J. Geophys. Res. 82: doi: 10.1029/JB082i036p05737

Fei, H., Koizumi, S., Sakamoto, N., Hashiguchi, M., Yurimoto, H., Marquardt, K., Katsura, T., 2016. New constraints on upper mantle creep mechanism inferred from silicon grain-boundary diffusion rates. Earth Planet. Sci. Lett.. 433, 350-359.

Fisler, D. K., Mackwell, S. J., Petsch, S., 1997. Grain boundary diffusion in

enstatite. Physics and Chemistry of Minerals. 24, 264-273.
Fodor, R.V., Sial, A.N., Gandhok, G., 2002. Petrology of spinel peridotite xenoliths from northeastern Brazil: lithosphere with a high geothermal gradient imparted by Fernando de Noronha plume. J. S. Am. Earth Sci. 15, 199-214.
French, S., Lekic, V., Romanowicz, B., 2013. Waveform Tomography Reveals Channeled Flow at the Base of the Oceanic Asthenosphere. Science. 342, 227-230.
Frets, E.C., Tommasi, A., Garrido, C.J., Vauchez, A., Mainprice, D., Targuisti, K., Amri, I., 2014. The Beni Bousera Peridotite (Rif Belt, Morocco): an Oblique-slip Low-angle Shear Zone Thinning the Subcontinental Mantle Lithosphere. J. Petrol. 55, 283-313.
Ganade de Araujo, C.E., Weinberg, R.F. and Cordani, U.G., 2014. Extruding the Borborema Province (NE-Brazil): a two-stage Neoproterozoic collision process. Terra Nova 26, 157-168.
Ganade de Araujo, C.E., Cordani, U.G., Agbossoumounde, Y., Caby, R., Basei, M.A.S., Weinberg, R.F. and Sato, K., 2016. Tightening-up NE Brazil and NW Africa connections: New U–Pb/Lu–Hf zircon data of a complete plate tectonic cycle in the Dahomey belt of the West Gondwana Orogen in Togo and Benin. Precambrian Res. 276, 24-42.
Gouriet, K., Cordier, P., Garel, F., Thoraval, C., Demouchy, S., Tommasi, A., Carrez, P., 2019. Dislocation dynamics modelling of the power-law breakdown in olivine single crystals: Toward a unified creep law for the upper mantle. Earth Planet. Sci. Lett. 506, 282-291.
Green, H.W., Gueguen, Y., 1974. Origin of Kimberlite Pipes by Diapiric Upwelling in Upper Mantle. Nature. 249, 617-620.
Gripp, A., Gordon, R., 2002. Young tracks of hotspots and current plate velocities. Geophys. J. Int. 150, 321–361.
Hammond, J.O.S., Kendall, J.M., Wookey, J., Stuart, G.W., Keir, D., Ayele, A., 2014. Differentiating flow, melt, or fossil seismic anisotropy beneath Ethiopia, Geochem. Geophys. Geosyst. (15) DOI:10.1002/2013GC005185
Hamza, V.M., Vieira, F.P., Silva, R.T.A., 2018. Anomalous heat flow belt along the continental margin of Brazil. Int J Earth Sci. 107, 19-33.
Hansen, L. N., Zhao, Y. H., Zimmerman, M. E., Kohlstedt, D. L., 2014. Protracted fabric evolution in olivine: Implications for the relationship among strain, crystallographic fabric, and seismic anisotropy. Earth Planet. Sci. Lett. 387, 157-168
Heine, C., Zoethout, J., Muller, R.D., 2013. Kinematics of the South Atlantic rift. Solid Earth 4, 215-253.
Heit, B., Sodoudi, F., Yuan, X., Bianchi, M., Kind, R., 2007. An S receiver function analysis of the lithospheric structure in South America. Geophys. Res. Lett. 34.
Hielscher, R., Schaeben, H., 2008. A novel pole figure inversion method: specification of the MTEX algorithm. J. Appl. Crystallogr. 41, 1024-1037.

Higgie, K., Tommasi, A., 2012. Feedbacks between deformation and melt distribution in the crust–mantle transition zone of the Oman ophiolite. Earth Planet. Sci. Lett. 359, 61-72.
Higgie, K., Tommasi, A., 2014. Deformation in a partially molten mantle: Constraints from plagioclase lherzolites from Lanzo, western Alps. Tectonophys. 615, 167-181.
Hirth, G., Kohlstedt, D., 2003. Rheology of the upper mantle and the mantle wedge: A view from the experimentalists. Inside the subduction Factory, *138*, 83-105.
Hollanda, M.H.B.M., Archanjo, C.J., Bautista, J.R., Souza, L.C., 2015. Detrital zircon ages and Nd isotope compositions of the Seridó and Lavras da Mangabeira basins (Borborema Province, NE Brazil): Evidence for exhumation and recycling associated with a major shift in sedimentary provenance. Precambrian Res. 258, 186-207.
Hollanda, M.H.B.M., Archanjo, C.J., Souza, L.C., Liu, D.Y., Armstrong, R., 2011. Long-lived Paleoproterozoic granitic magmatism in the Serido-Jaguaribe domain, Borborema Province-NE Brazil. J. S. Am. Earth Sci. 32, 287-300.
Hollanda, M.H.B.M., Archanjo, C.J., Macedo Filho, A.A., Fossen, H., Ernst, R.E., Castro, D.L.d., Melo, A.C. and Oliveira, A.L., 2018. The Mesozoic Equatorial Atlantic Magmatic Province (EQUAMP), in: Dyke Swarms of the World: A Modern Perspective. Springer Singapore, pp. 87-110.
Isaak, D.G., Ohno, I., Lee, P.C., 2006. The elastic constants of monoclinic single-crystal chrome-diopside to 1,300 K. Phys Chem Miner. 32, 691-699.
Jackson, J.M., Sinogeikin, S.V., Bass, J.D., 2007. Sound velocities and single-crystal elasticity of orthoenstatite to 1073 K at ambient pressure. Phys. Earth Planet. Inter. 161, 1-12.
Kaczmarek, M.A., Tommasi, A., 2011. Anatomy of an extensional shear zone in the mantle, Lanzo massif, Italy. Geochem. Geophys. Geosyst. 12, Q0AG06, doi:10.1029/2011GC003627.
Kelemen, P.B., 1990. Reaction between Ultramafic Rock and Fractionating Basaltic Magma .1. Phase-Relations, the Origin of Calc-Alkaline Magma Series, and the Formation of Discordant Dunite. J. Petrol. 31, 51-98.
Klemme, S., 2004. The influence of Cr on the garnet-spinel transition in the Earth's mantle: experiments in the system MgO-Cr2O3-SiO2 and thermodynamic modelling. Lithos 77, 639-646.
Knesel, K.M., Souza, Z.S., Vasconcelos, P.M., Cohen, B.E., Silveira, F.V., 2011. Young volcanism in the Borborema Province, NE Brazil, shows no evidence for a trace of the Fernando de Noronha plume on the continent. Earth Planet. Sci. Lett. 302, 38-50.
Kostopoulos, D.K., 1991. Melting of the Shallow Upper Mantle - a New Perspective. J. Petrol. 32, 671-699.
Kourim, F., Vauchez, A., Bodinier, J. L., Alard, O., Bendaoud, A., 2015. Subcontinental lithosphere reactivation beneath the Hoggar swell (Algeria):

Localized deformation, melt channeling and heat advection. Tectonophys. 650, 18-33.
Lamarque, G., Julià, J., 2019. Lithospheric and sub-lithospheric deformation under the Borborema Province of NE Brazil from receiver function harmonic stripping. Solid Earth Discuss. https://doi.org/10.5194/se-2019-41.
Le Roux, V., Bodinier, J.L., Tommasi, A., Alard, O., Dautria, J.M., Vauchez, A., Riches, A.J.V., 2007. The Lherz spinel lherzolite: Refertilized rather than pristine mantle. Earth Planet. Sci. Lett. 259, 599-612.
Lima, M.V.A.G.d., Berrocal, J., Soares, J.E.P., Fuck, R.A., 2015. Deep seismic refraction experiment in northeast Brazil: New constraints for Borborema province evolution. J. S. Am. Earth Sci. 58, 335-349.
Lissenberg, C.J., Dick, H.J.B., 2008. Melt–rock reaction in the lower oceanic crust and its implications for the genesis of mid-ocean ridge basalt. Earth Planet. Sci. Lett. 271, 311-325.
Liu, S., Tommasi, A., Vauchez, A., Mazzucchelli, M. 2019. Deformation, annealing, melt-rock interaction, and seismic properties of an old domain of the equatorial Atlantic lithospheric mantle. Tectonics 38, doi: 1029/2018TC005373.
Luz, R.M.N., Julià, J., do Nascimento, A.F., 2015. Bulk crustal properties of the Borborema Province, NE Brazil, from P-wave receiver functions: Implications for models of intraplate Cenozoic uplift. Tectonophys. 644-645, 81-91.
Mainprice, D., Bachmann, F., Hielscher, R., Schaeben, H., 2014. Descriptive tools for the analysis of texture projects with large datasets using MTEX: strength, symmetry and components. Geol. Soc. London Spec. Publ. 409, 251-271.
Mainprice, D., Hielscher, R., Schaeben, H., 2011. Calculating anisotropic physical properties from texture data using the MTEX open-source package. Geol. Soc. London Spec. Publ. 360, 175-192.
Marques, F.O., Nogueira, F.C.C., Bezerra, F.H.R., Castro, D.L., 2014. The Araripe Basin in NE Brazil: An intracontinental graben inverted to a high-standing horst. Tectonophys. 630, 251-264.
Klöcking, M., Tribaldos, V.R., Hoggard, M., White, N., Maclennan, J., Rezende Guimarães, A., 2018. Linking uplift and volcanism of the Borborema Province, northeast Brazil. EGU General Assembly Conference Abstracts 20, p. 9966.
Mercier, J.C.C., Nicolas, A., 1975. Textures and Fabrics of Upper-Mantle Peridotites as Illustrated by Xenoliths from Basalts. J. Petrol. 16, 454-487.
Mizusaki, A.M.P., Thomaz-Filho, A., Milani, E.J., Césero, P., 2002. Mesozoic and Cenozoic igneous activity and its tectonic control in northeastern Brazil. J. S. Am. Earth Sci. 15, 183-198.
Moulin, M., Aslanian, D., Unternehr, P., 2010. A new starting point for the South and Equatorial Atlantic Ocean. Earth-Sci Rev. 98, 1-37.
Neves, S.P., 2003. Proterozoic history of the Borborema province (NE Brazil):

Correlations with neighboring cratons and Pan-African belts and implications for the evolution of western Gondwana. Tectonics. 22.
Ngonge, E.D., de Hollanda, M.H.B.M., Archanjo, C.J., de Oliveira, D.C., Vasconcelos, P.M.P., Muñoz, P.R.M., 2016a. Petrology of continental tholeiitic magmas forming a 350-km-long Mesozoic dyke swarm in NE Brazil: Constraints of geochemical and isotopic data. Lithos. 258-259, 228-252.
Ngonge, E.D., de Hollanda, M.H.B.M., Pimentel, M.M., de Oliveira, D.C., 2016b. Petrology of the alkaline rocks of the Macau Volcanic Field, NE Brazil. Lithos. 266-267, 453-470.
Nimis, P., Grutter, H., 2010. Internally consistent geothermometers for garnet peridotites and pyroxenites. Contrib Mineral Petr. 159, 411-427.
Niu, Y.L., 1997. Mantle melting and melt extraction processes beneath ocean ridges: Evidence from abyssal peridotites. J. Petrol. 38, 1047-1074.
Nogueira, F.C.C., Marques, F.O., Bezerra, F.H.R., Castro, D.L., Fuck, R.A., 2015. Cretaceous intracontinental rifting and post-rift inversion in NE Brazil: Insights from the Rio do Peixe Basin. Tectonophysics 644-645, 92-107.
O'Neill, H.S.C., 1981. The transition between spinel lherzolite and garnet lherzolite, and its use as a geobarometer. Contrib. Mineral. Petr. 77, 185-194.
Oliveira, R.G., Medeiros, W.E., 2012. Evidences of buried loads in the base of the crust of Borborema Plateau (NE Brazil) from Bouguer admittance estimates. J. S. Am. Earth Sci. 37, 60-76.
Perlingeiro, G., Vasconcelos, P.M., Knesel, K.M., Thiede, D.S., Cordani, U.G., 2013. Ar-40/Ar-39 geochronology of the Fernando de Noronha Archipelago and implications for the origin of alkaline volcanism in the NE Brazil. J. Volcanol. Geotherm. Res. 249, 140-154.
Princivalle, F., Salviulo, G., Fabro, C., Demarchi, G., 1994. Inter- and intra-crystalline temperature and pressure estimates on pyroxenes from NE Brazil mantle xenoliths. Contrib. Mineral. Petr. 116, 1-6.
Qi, C., Hansen, L. N., Wallis, D., Holtzman, B. K., Kohlstedt, D. L., 2018. Crystallographic Preferred Orientation of Olivine in Sheared Partially Molten Rocks: The Source of the "a-c Switch". Geochem. Geophys. Geosyst. 19, 316-336
Rivalenti, G., Mazzucchelli, M., Girardi, V.A.V., Vannucci, R., Barbieri, M.A., Zanetti, A., Goldstein, S.L., 2000. Composition and processes of the mantle lithosphere in northeastern Brazil and Fernando de Noronha: evidence from mantle xenoliths. Contrib. Mineral. Petr. 138, 308-325.
Rivalenti, G., Zanetti, A., Girardi, V.A.V., Mazzucchelli, M., Tassinari, C.C.G., Bertotto, G.W., 2007. The effect of the Fernando de Noronha plume on the mantle lithosphere in north-eastern Brazil. Lithos 94, 111-131.
Tribaldos, V. R., White, N.J., Roberts, G.G., Hoggard, M.J., 2017. Spatial and temporal uplift history of South America from calibrated drainage analysis. Geochem. Geophys. Geosyst. 18, 2321-2353.
Sa, J.M., McReath, I., Leterrier, J., 1995. Petrology, Geochemistry and

Geodynamic Setting of Proterozoic Igneous Suites of the Oros Fold Belt (Borborema Province, Northeast Brazil). J. S. Am. Earth Sci. 8, 299-314.
Sang, L.Q., Bass, J.D., 2014. Single-crystal elasticity of diopside to 14 GPa by Brillouin scattering. Phys. Earth Planet. Inter. 228, 75-79.
Santos, E.J., Schmus, W.R.V., Kozuch, M., Neves, B.B.d.B., 2010. The Cariris Velhos tectonic event in Northeast Brazil. J. S. Am. Earth Sci. 29, 61-76.
Schutt, D.L., Lowry, A.R., Buehler, J.S., 2018. Moho temperature and mobility of lower crust in the western United States. Geology 46, 219–222.
Silveira, F.V., 2006. Magmatismo cenozóico da porção central do Rio Grande do Norte, NE do Brasil. Ph.D. Thesis, Univ. Federal do Rio Grande do Norte, UFRN, Brazil.
Simões Neto, F.L., Julià, J. Schimmel, M., 2019. Upper-mantle structure of the Borborema Province, NE Brazil, from *P*-wave tomography: implications for rheology and volcanism, *Geophys. J. Intern.* 216, 231–250.
Skemer, P., Karato, S.I., 2008. Sheared lherzolite xenoliths revisited. J. Geophys. Res. 113, B07205.
Souza, Z.S., Vasconcelos, P., Nascimento, M., V. Silveira, F., S. Paiva, H., Dias, L.G., Thiede, D., Carmo, I., 2003. 40Ar/39Ar geochronology of Mesozoic and Cenozoic magmatism in NE Brazil. In Proceedings of IV South American Symposium on Isotope Geology, 691-694.
Souza, Z.S., Kalsbeek, F., Deng, X.-D., Frei, R., Kokfelt, T.F., Dantas, E.L., Li, J.-W., Pimentel, M.M., Galindo, A.C., 2016. Generation of continental crust in the northern part of the Borborema Province, northeastern Brazil, from Archaean to Neoproterozoic. J. S. Am. Earth Sci. 68, 68-96.
Taylor, W.R., 1998. An experimental test of some geothermometer and geobarometer formulations for upper mantle peridotites with application to the thermobarometry of fertile lherzolite and garnet websterite. Neues Jb. Miner. Abh. 172, 381-408.
Tikoff, B., Russo, R., Teyssier, C., Tommasi, A. 2004. Mantle-driven deformation of orogenic zones and clutch tectonics. In: J. Grocott, K. McCaffrey, G. Taylor & B. Tikoff (eds) Vertical and horizontal decoupling in the lithosphere. Geol. Soc. London Spec. Publ. 227, 41-64.
Tommasi, A., Ishikawa, A., 2014. Microstructures, composition, and seismic properties of the Ontong Java Plateau mantle root. *Geochem. Geophys. Geosyst.*, 15, doi: 10.1002/2014GC005452
Tommasi, A., Vauchez, A., 2015. Heterogeneity and anisotropy in the lithospheric mantle. Tectonophys. 661, 11-37.
Tommasi, A., Vauchez, A., Daudré, B., 1995. Initiation and propagation of shear zones in a heterogeneous continental lithosphere. J. Geophys. Res. 100, 22083-22101.
Tommasi, A, Mainprice, D., Canova, G., Chastel, Y. 2000. Viscoplastic self-consistent and equilibrium-based modeling of olivine lattice preferred

orientations. Implications for the upper mantle seismic anisotropy. J. Geophys. Res. 105, 7893-7908

Tommasi, A., Tikoff, B., Vauchez, A. 1999. Upper mantle tectonics: Three-dimensional deformation, olivine crystallographic fabrics and seismic properties. Earth Planet. Sci. Lett. 168, 173-186

Tommasi, A., Vauchez, A., Ionov, D. A., 2008. Deformation, static recrystallization, and reactive melt transport in shallow subcontinental mantle xenoliths (Tok Cenozoic volcanic field, SE Siberia). Earth Planet. Sci. Lett. 272, 65-77

Ussami, N., Molina, E.C., Medeiros, W.E., 1999. Novos vinculos sobre a Evolução Térmica da Margem Continental Leste do Brasil, *In VII National Symposium on Tectonic Studies, Extended Abstracts*: Sociedade Brasileira de Geologia, **7,** 20–23

Van der Wal, D., Chopra, P., Drury, M., Gerald, J.F., 1993. Relationships between dynamically recrystallized grain size and deformation conditions in experimentally deformed olivine rocks. Geophys. Res. Lett. 20, 1479-1482.

van Schmus, W.R., Oliveira, E.P., da Silva Filho, A.F., Toteu, S.F., Penaye, J., Guimarães, I.P., 2008. Proterozoic links between the Borborema Province, NE Brazil, and the Central African Fold Belt. Geol. Soc. London Spec. Publ. 294, 69-99.

Vauchez, A., Nicolas, A., 1991. Mountain building: strike-parallel motion and mantle anisotropy. Tectonophys. 185, 183-201

Vauchez, A., Dineur, F., Rudnick, R., 2005. Microstructure, texture and seismic anisotropy of the lithospheric mantle above a mantle plume: insights from the Labait volcano xenoliths (Tanzania). Earth and Planetary Science Letters 232, 295-314.

Vauchez, A., Neves, S., Caby, R., Corsini, M., Egydio-Silva, M., Arthaud, M., Amaro, V., 1995. The Borborema Shear Zone System, NE Brazil. J. S. Am. Earth Sci. 8, 247-266.

Vauchez, A., Tommasi, A., Mainprice, D., 2012. Faults (shear zones) in the Earth's mantle. Tectonophys. 558, 1-27.

Viegas, L.G.F., Archanjo, C.J., Hollanda, M.H.B.M. and Vauchez, A., 2014. Microfabrics and zircon U/Pb (SHRIMP) chronology of mylonites from the Patos shear zone (Borborema Province, NE Brazil). Precambrian Research 243, 1-17.

Walter, M.J., Sisson, T.W., Presnall, D.C., 1995. A Mass Proportion Method for Calculating Melting Reactions and Application to Melting of Model Upper-Mantle Lherzolite. Earth Planet. Sci. Lett. 135, 77-90.

Workman, R.K., Hart, S.R., 2005. Major and trace element composition of the depleted MORB mantle (DMM). Earth Planet. Sci. Lett. 231, 53-72.

Wu, J., Zhang, Z., Kong, F., Yang, B.B., Yu, Y., Liu, K.H., Gao, S.S., 2015. Complex seismic anisotropy beneath western Tibet and its geodynamic implications. Earth Planet. Sci. Lett. 413, 167-175.

Table 1

Click here to download Table: Table 1_revised_v2.pdf

Table 1 Microstructures, modal compositions, thermometry, and bulk rock Mg# of Macau volcanics peridotite xenoliths

Sample	Location	Rock type	Microstructure	Modal compostions (%)				Thermometry (°C)								Bulk rock Mg#*
								Two-pyroxene				Ca-in-opx				
				ol	opx	cpx	sp	Rim	sd	Core	sd	Rim	sd	Core	sd	
16CA07	Pico Cabugi	Lz	Coarse-granular	61	22	15	2	816	52	834	9	903	22	878	11	89.0
16CA08	Pico Cabugi	Lz		58	26	15	1	834	21	830	27	905	13	869	6	89.0
16CA09	Pico Cabugi	Lz		70	23	7	1	923	17	920	18	970	5	958	7	90.3
16CA12	Pico Cabugi	Lz		69	19	10	2									
16CA14	Pico Cabugi	Lz		58	28	12	2	627	38	592	51	836	148	790	16	89.4
BO9^^	Bodo	Lz		63	22	15	<1	946		914		899		893		90.6
16CA01	Pico Cabugi	Hz	Coarse-porphyroclastic	79	18	3	1	985	72	1026	180	955	3	970	41	90.9
16CA02	Pico Cabugi	Hz		82	13	5	1									
16CA03	Pico Cabugi	Hz		87	10	3	<1	1024	8	1111	87	1119	148	1028	149	90.7
16CA04	Pico Cabugi	Lz		59	23	15	4									
16CA05	Pico Cabugi	Lz		71	15	14	<1									
16CA06	Pico Cabugi	Lz		67	21	11	1	703	5	710	16	778	9	846	46	90.2
16CA11	Pico Cabugi	Lz		72	8	18	2	693	8	691	25	813	21	809	18	89.5
16CA15	Pico Cabugi	Lz		67	19	13	1	887	152	730	112	856	29	785	76	89.5
16CA18	Pico Cabugi	Hz		82	16	2	1	1036	121	952	110	1005	106	942	8	90.9
GR1^^	Fazenda Geroncio	Lz		76	16	7	1	1202	14	1183	36	1178	6	1180	7	90.0
SV8^^	Serra Verde	Lz		77	13	9	1	1026		1008		1038		1034		90.6
SV14^^	Serra Verde	We		53	0	45	1									91.0
AG6^^	Serra Aguda	Lz	Fine-porphyroclastic	61	24	13	1			1186	1			1192	10	89.4
AG7^^	Serra Aguda	Hz		76	20	3	<1			1215	6			1220	3	90.7
Pc105^	Pico Cabugi	Hz		72	25	4	<1			1210				1220		91.3
Pc109^	Pico Cabugi	Hz		74	21	4	<1			1225				1233		90.4

Hz: Harzburgite; Lz: Lherzolite; We: Wehrlite; ^ Samples from Rivalenti et al. (2000); ^^ Samples from Rivalenti et al, (2007)

* estimated by average chemical composition and the modal contents (area.%) of each mineral except Pc105, Pc109, AG6, BO9 and SV8 for which whole rock chemical data were available

Table 2

Click here to download Table: Table 2_revised.pdf

Table 2 Quantitative texture and microstructure parameters derived from EBSD mapping for olivine, orthopyroxene, and clinopyroxene

Sample	Microstructure	Rex area fraction	Olivine							Orthopyroxene			Clinopyroxene	
			J-index	BA-index	M2M (°)	GOS (°)	Shape factor^	Grain size^ (µm)	Aspect ratio^	Shape factor^	Grain size^ (µm)	Aspect ratio^	Grain size^ (µm)	Aspect ratio^
16CA07	Coarse-granular	Bulk-rock	5.8	0.34	1.56	1.27	1.67	1381	1.81	1.69	1126	1.61	827	1.61
16CA08		Bulk-rock	6.6	0.35	1.36	0.74	1.56	1493	1.69	1.51	1322	1.57	936	1.62
16CA09		Bulk-rock	6.4	0.46	1.14	1.61	1.59	2233	1.55	1.46	1401	1.53	872	1.60
16CA12		Bulk-rock	6.3	0.62	1.73	1.33	1.65	2134	1.59	1.49	1190	1.51	926	1.67
16CA14		Bulk-rock	4.7	0.33	1.46	1.06	1.64	1899	1.55	2.01	2688	1.57	1007	1.61
BO9^^		Bulk-rock	6.5	0.84	1.41	0.88	1.85	1577	2.04	2.00	1669	1.80	1008	1.80
16CA01	Coarse-porphyroclastic	Bulk-rock	6.6	0.77	2.60	1.27	1.90	2428	1.86	1.64	1088	1.83	799	1.61
16CA02		Bulk-rock	6.2	0.81	2.67	1.52	1.73	2001	1.66	1.61	1194	1.62	636	1.70
16CA03		Bulk-rock	6.8	0.73	2.90	1.34	1.74	2140	1.78	1.95	894	1.94	248	1.86
16CA04		Bulk-rock	4.8	0.45	2.08	1.90	1.61	1813	1.56	2.14	2678	1.54	1124	1.63
16CA05		Bulk-rock	3.8	0.47	2.22	1.39	1.64	1856	1.62	1.85	2503	1.96	1074	1.61
16CA06		Bulk-rock	7.3	0.27	2.23	1.17	1.80	2192	1.64	2.12	3376	1.82	925	1.59
16CA11		Bulk-rock	5.8	0.31	3.35	1.48	1.71	2281	1.63	1.75	3298	1.58	1131	1.70
16CA15		Bulk-rock	5.1	0.48	1.66	0.78	1.90	1837	1.66	2.38	3279	1.76	947	1.69
16CA18		Bulk-rock	8.0	0.82	2.44	1.36	1.80	2416	1.93	1.78	1197	2.02	459	1.89
GR1		Bulk-rock	8.5	0.45	2.28	1.37	1.83	2507	1.87	1.75	1378	1.62	1048	1.52
SV8		Bulk-rock	9.0*	0.27	2.33	2.26	1.91	1589	2.04	1.75	1337	1.85	775	1.56
SV14		Bulk-rock	6.8	0.37	2.22	1.38	2.22	1655	1.68				1713	1.56
AG6	Fine-porphyroclastic	Bulk-rock	4.6	0.44	5.64	1.96	3.02	1221	1.69	1.89	1646	1.45	920	1.73
		Porphyroclasts	9.5	0.55	8.07	5.66	4.04	2143	1.74	1.89	1672	1.45	965	1.73
		Neoblasts (30%)	2.2	0.27	2.51	1.50	1.77	117	1.61	1.69	157	1.59	175	1.72
AG7		Bulk-rock	16.6*	0.40	3.05	0.89	2.83	3062	1.67	2.01	1301	1.62	729	1.63
		Porphyroclasts	24.6*	0.41	3.67	4.05	3.17	3814	1.67	2.06	1511	1.56	906	1.61
		Neoblasts (22%)	2.8	0.38	0.57	0.49	1.60	365	1.65	1.82	540	1.82	418	1.66
Pc105		Bulk-rock	6.4	0.25	6.18	1.47	2.20	2133	1.68	2.06	2772	1.75	748	1.52
		Porphyroclasts	8.2	0.26	7.22	5.30	2.36	2538	1.70	2.10	2919	1.74	865	1.48
		Neoblasts (15%)	2.1	0.26	0.54	0.56	1.49	311	1.57	1.48	464	1.91	435	1.61
Pc109		Bulk-rock	7.5	0.18	5.25	1.48	2.34	2330	1.74	2.56	1881	2.04	1082	1.95
		Porphyroclasts	9.2	0.18	5.96	4.86	2.48	2682	1.78	2.63	2046	2.04	1231	2.01
		Neoblasts (14%)	2.6	0.20	0.61	0.59	1.55	358	1.52	1.90	476	2.09	358	1.65

All values are averages over the entire EBSD map, weighted by the grain area

M2M: Misorientation relative to mean orientation of the grain; GOS: Grain orientation spread; Rex: recrystallized

^ Grain sizes, aspect ratios, and shape factors are apparent 2D values. Aspect ratios may be underestimated since many sections were not cut on the XY structural plane.

* marks J-index values that are probably overestimated due to the small number of coarse grains in the thin section (small samples)

Table 3

Click here to download Table: Table 3_revised.pdf

Table 3. Calculated seismic properties for the individual and for the average low- and high-temperature Macau peridotites

	Sample	Rock type	Microstructures	Seismic properties (velocity in km/s and anisotropy in %)												
				Vp max	Vp min	Avp	AVs	Vs1 max	Vs1 min	AVs1	Vs2 max	Vs2 min	AVs2	Vp/Vs1 max	Vp/Vs1 min	AVp/Vs1
Low-temperature samples (<1000°C) P=1.46GPa T=916°C	16CA07	Lz	Coarse-granular	8.2	7.4	10.0	7.1	4.7	4.4	5.2	4.5	4.3	4.4	1.8	1.7	6.3
	16CA08	Lz	Coarse-granular	8.2	7.5	9.2	6.7	4.7	4.5	4.2	4.5	4.3	4.1	1.8	1.7	5.7
	16CA09	Lz	Coarse-granular	8.2	7.6	7.8	5.8	4.7	4.5	3.5	4.5	4.4	4.0	1.8	1.7	7.7
	16CA14	Lz	Coarse-granular	8.1	7.5	7.8	5.5	4.7	4.5	4.2	4.5	4.4	3.4	1.8	1.7	5.4
	BO9	Lz	Coarse-granular	8.3	7.6	9.3	6.0	4.7	4.5	3.0	4.6	4.3	5.2	1.8	1.7	9.2
	16CA06	Lz	Coarse-porph	8.2	7.5	9.1	7.3	4.7	4.4	5.9	4.6	4.3	4.6	1.8	1.7	5.5
	16CA11	Lz	Coarse-porph	8.2	7.6	7.7	6.5	4.7	4.5	3.8	4.5	4.4	3.2	1.8	1.7	5.5
	16CA15	Lz	Coarse-porph	8.2	7.6	7.4	5.6	4.6	4.5	3.4	4.5	4.4	4.3	1.8	1.7	5.3
	Average	**-**	**-**	***8.2***	***7.6***	***7.9***	***5.2***	***4.7***	***4.5***	***3.6***	***4.6***	***4.4***	***3.7***	***1.8***	***1.7***	***5.5***
High-temperature samples (>1000°C) P=2.12GPa T=1189°C	16CA01	Hz	Coarse-porph	8.4	7.4	12.3	8.1	4.6	4.4	4.1	4.5	4.2	7.1	1.9	1.7	10.9
	16CA03	Hz	Coarse-porph	8.5	7.4	14.0	10.0	4.7	4.4	6.3	4.5	4.2	7.3	1.9	1.6	13.5
	16CA18	Hz	Coarse-porph	8.6	7.4	14.2	9.7	4.7	4.4	5.7	4.5	4.2	7.2	1.9	1.6	14.7
	GR1	Lz	Coarse-porph	8.2	7.4	10.4	8.2	4.6	4.4	5.9	4.5	4.2	5.4	1.8	1.7	7.3
	SV8	Lz	Coarse-porph	8.2	7.4	11.3	9.0	4.7	4.3	7.2	4.5	4.2	5.8	1.8	1.7	6.6
	AG6	Lz	Fine-porph	8.0	7.4	8.2	6.3	4.6	4.4	5.0	4.4	4.3	3.6	1.8	1.7	5.9
	PC105	Hz	Fine-porph	8.0	7.4	7.7	5.9	4.6	4.3	5.7	4.4	4.3	1.9	1.8	1.7	3.5
	PC109	Hz	Fine-porph	8.1	7.4	9.1	7.4	4.6	4.3	6.4	4.4	4.3	3.0	1.8	1.7	4.3
	AG7	Hz	Fine-porph	8.2	7.4	10.4	8.7	4.7	4.4	6.3	4.5	4.2	5.8	1.8	1.7	9.3
	Average	**-**	**-**	***8.3***	***7.4***	***10.5***	***7.7***	***4.7***	***4.4***	***5.8***	***4.5***	***4.3***	***4.9***	***1.8***	***1.7***	***7.4***

Coarse-porph: Coarse-porphyroclastic; Fine-porph: Fine-porphyroclastic; Hz: Harzburgite; Lz: Lherzolite

AVp: Maximum P-wave propagation anisotropy; AVs: Maximum S-wave polarization anisotropy; AVs1: Maximum fast S-wave propagation anisotropy; AVs2: Maximum slow S-wave propagation anisotropy; AVs1/Vp: Maximum anisotropy of Vp/Vs1 ratio

Supplementary material description

Click here to download Supplementary material for online publication only: SupplementaryMaterial.docx

Supplementary Fig. S1

Click here to download Supplementary material for online publication only: FigS1_spinel_chemical.pdf

Supplementary Table S1

Click here to download Supplementary material for online publication only: Table_S1.xlsx

Supplementary Table S2

Click here to download Supplementary material for online publication only: Table_S2.xlsx

Supplementary Table S3

Click here to download Supplementary material for online publication only: Table_S3.xlsx

Supplementary Table S4

Click here to download Supplementary material for online publication only: Table_S4.xlsx